

**Studying the Physics of Excitons in Semiconductor
Quantum Heterostructures**

A thesis

submitted in partial fulfillment of the

requirements for the degree of

Doctor of Philosophy

by

Amit Bhunia

20143308



Department of Physics

**Indian Institute of Science Education and Research –
Pune, India**

Dedicated to my beloved
grandmother
Smt. Laxmi Bhunia

CERTIFICATE

Certified that the work incorporated in this thesis entitled **Studying the Physics of Excitons in Semiconductor Quantum Heterostructures** submitted by **Amit Bhunia** was carried out by the candidate, under my supervision. The work presented here or any part of it has not been included in any other thesis submitted previously for the award of any degree or diploma from any other University or institution.

Date:

Dr. Shouvik Datta

Supervisor

DECLARATION

I declare that this written submission represents my ideas in my own words and where others' ideas have been included, I have adequately cited and referenced the original sources. I also declare that I have adhered to all principles of academic honesty and integrity and have not misrepresented or fabricated or falsified any idea/ data/ fact/ source in my submission. I understand that violation of the above will be cause for disciplinary action by the Institute and can also evoke penal action from the sources which have thus not been properly cited or from whom proper permission has not been taken when needed.

Date:

Amit Bhunia

Roll No. 20143308

Acknowledgement

Fulfilment of a goal requires contributions of many individuals throughout a journey. Completion of doctoral degree is one such goal which every budding research student wishes to accomplish within time. During my journey to achieve this goal, I also have come across many people who have significantly contributed by sharing their knowledge and support. Here, I want to convey few words of acknowledgement which might be too short to express my true gratitude to them.

First and foremost, I would like to take this opportunity to thank my supervisor, Dr. Shouvik Datta for his continuous support, guidance, valuable and motivating suggestions. I especially thank him for providing an independent and most enjoyable working environment in the lab. His thoughtful ideas and intuitions have helped a lot to understand the critical and intriguing problems of experimental physics. He has always inspired me to explore new physics and not to take a short cut in science. This will certainly motivate and encourage me to pursue science as a career.

I wish to thank my research advisory committee (RAC) members Prof. Kantimoy Dasgupta from IIT-B, India and Dr. Surjeet Singh from IISER-Pune for their valuable and constructive suggestion on my work during the RAC meetings. This has helped me a lot to gain some basic knowledge in my research topics and focussing in a particular research problem. I would also like to thank Prof. Yara Galvão Gobato from departamento de Física, Universidade Federal de São Carlos, Brazil for her insightful inputs during our discussion. I am also grateful to my teachers, TA mentors, and all the faculty members of the department of physics, IISER-Pune for their continuous support and sharing valuable knowledge with me. I also like to thank Prof. Sunil Mukhi, former chair physics program, and Dr. Girish Ratnaparkhi, former dean of doctoral studies for their kind academic help wherever I needed during my Ph.D. I would also like to express my gratitude to the past and present directors of IISER-Pune, Prof. Ganesh and Prof. Udgaonkar, respectively for providing state of the art research and lab facility in IISER-Pune. Here, I also specially like to thank Dr. Angshuman Nag from department of chemistry, IISER-Pune for valuable discussion, suggestions during the collaborative work on perovskite materials. He is our good collaborator and I am grateful to him for believing in my research capability. I am thankful to Nilesh sir, Prashant, Anil, Sudhir for sorting out various lab issues. Assistance of Mr. Prabhakar and Mr. Tushar was instrumental in getting all the paperwork in order.

Now, I would like to convey my sincere gratitude to one of the most important person in my research career Prof. Mohamed Henini from the school of physics and astronomy, University of Nottingham, UK. A significant research work of the thesis is based on the samples which were provided by Prof. Henini. He is a very good, responsible and kind-hearted person. I have spent three months in his experimental lab during Ph.D. as a Newton-Bhabha fellow. He had assisted me a lot in any research related issues as well as helped me to look for potential collaborators for post-doctoral position all the possible ways, he could. So, I am really indebted to him for all these kind gestures he has shown to me.

I would also like to thank all my present and past lab members for assisting me in setting-up the experimental lab, sharing knowledge, valuable discussions, etc. Especially, I am grateful to my three seniors Dr. Kanika Bansal, Dr. Padmashri Patil, and Dr. Arthur Varghese for their initial supports and helping me to learn all the experimental facilities available in the lab. They always motivated me to pursue a good research career. I wish to thank Kaustav, Mayur, Saurav, Deepak, Sumit, Arindam, Vaibhab, Omkar with whom I have spent valuable time in the lab. I also like to thank my present lab members Mohit, Anweshi, Dipti, and Gautam for their support and maintaining the spirit of the lab.

It will be a complete injustice if I forget to acknowledge the following peoples who have made my IISER life more than heaven I have ever dreamt of. I was the only physics Ph.D. student who joined the department in 2014 January session. But, I never felt lonely as I met Sanku, Reja, Bag, Panja, Shishir, Nishta, Harshini, Rohit Babar, and many other seniors cum friends in the department. They really had made my hostel life as well as research life quite enjoyable. I am also quite fond of sports like football, cricket, badminton, table tennis, etc. and I have spent some memorable time with Sudeb, Arindam, Avishek, Barun D, Biplab J, Maidul, Projjal, Arunavo, Unmesh, Sarath, Swarnkar, and others in the field and off the field which will be cherished for long time. I also wish to thank my batch mates Supratik, Sumit, Chandra, Partha, Avirup, Sagar, Shammi, Avinas, Vijaykanth, Chetan and others for their good company during these days. I also specially like to thank Jyotirmoy, Milan, Tathagata, Rajesh, Pulak, Tamaghna, Rathijit, Rupak Da, Korak, Panda, Pahan, and others for spending good fun time during cooking at night as we usually made delicious dishes. Here, I also like to thank Pratik, Debarati, Barun da, Ayan Da and family for their kind hospitality during my stay in Nottingham, UK and they are really awesome friends.

I also like to thank all my teachers who always motivated and inspired me to pursue science as career. My friends Arif, Pratim, Amitava, Anjan, Kusha, Rome, Kundu and others who are there with me from my school and college days, always supported me wherever I needed.

I like to express my sincere gratitude to my family and relatives who helped me a lot during this long journey. Firstly, I would like to take this opportunity to show my earnest respect and love to my grandmother who is not with us anymore. She was such a caring and loving lady I ever met. I would also like to thank my uncle (kaku) and aunts (pisi) who always motivated, supported and inspired me to pursue higher studies. Without their help and guidance, it would not have been possible to achieve this goal. I want to thank my brothers and sisters Somit, Rinku, Rana, Raja, Rajib, Manto, Tithi with whom I have spent a valuable time. Last but definitely not the least, I would like to thank my parents for their constant guidance, encouragement and support which have helped me to become what I am today.

September, 2019

Amit Bhunia

Contents

Abstract	xi-xiii
List of figures	xiv-xv
List of tables	xvi
Fundamental constants	xvii
1 Introduction	1
1.1 Motivation.....	1
1.2 Basics of semiconductor physics.....	2
1.2.1 Compound semiconductors.....	3
1.2.2 Basics of energy bands and energy bandgap.....	4
1.2.3 Doped semiconductors and Fermi level.....	7
1.2.4 Semiconductor devices.....	9
1.2.5 Semiconductor quantum heterostructures.....	12
1.3 Excitons	16
1.3.1 Types of excitons.....	17
1.3.2 Theoretical models of excitons.....	19
1.3.3 Experimental signature of excitons.....	22
1.3.4 Why study excitons?.....	25
2 Experimental techniques and set-ups	28
2.1 Introduction.....	28
2.2 Electrical approach to study excitons.....	28
2.3 Opto-electrical approach to study excitons.....	30
2.4 Low-temperature system.....	33
3 Dielectric signature of excitons and excitonic Mott transition in quantum confined laser structures	36
3.1 Introduction.....	36
3.2 Negative activation energy.....	37
3.3 Excitonic Mott transition.....	39
3.4 Background physics of frequency-dependent impedance.....	41
3.5 Instrumentation and description of samples.....	43

3.6	Results and discussion.....	44
3.6.1	Differential capacitance response, negative activation energy, and excitons.....	44
3.6.2	Electrical signature of excitonic Mott transition.....	50
3.6.3	Comparison of excitonic physics at room temperature and low temperature.....	51
	I. Differential capacitance response on similar injection current.....	51
	II. Photon flux and excitons.....	52
	III. Spectral signatures of excitons and excitonic Mott transition.	53
3.6.4	Prominent electrical signature of excitons in InGaAs/GaAs QDs laser diode.....	56
3.7	Conclusions.....	58

4 Physics of Indirect excitons and excitonic complexes using photocapacitance spectroscopy in GaAs/AlAs/GaAs heterostructure

4.1	Introduction.....	60
4.2	Excitonic dipole moments and electric field.....	64
4.3	Excitonic complexes.....	66
4.4	Fermi-edge singularity.....	69
4.5	Sample details and experimental techniques.....	70
4.6	Part A: Dipolar signature of indirect excitons using photocapacitance technique at room temperature.....	71
4.6.1	Results and observation.....	71
4.6.2	Discussion.....	74
	I. Schematic energy band diagram and carrier dynamics.....	74
	II. Excitonic dipole moments and field-induced binding energy.....	77
	III. Supporting analysis and frequency-dependent photocapacitance.	81
4.6.3	Summary of part A.....	84
4.7	Part B: Physics of indirect trions and Fermi-edge singularity at 100 K.....	85
4.7.1	Introduction.....	85
4.7.2	Results and discussion.....	87
	I. Presence of indirect positive trions and Fermi edge singularity at 100 K.....	87

II.	Spectral redshift and binding energy of indirect trions at 100 K..	92
III.	Differences in spectra at a fixed bias and with respect to temperature.....	97
IV.	Why photocapacitance spectra are superior over photoluminescence spectra in detecting such indirect excitonic complexes.....	99
4.7.3	Summary of part B.....	101
4.8	Temperature and bias dependent behaviour of photocapacitance.....	102
5	Photo-induced oscillations in dielectric measurement: involvement of excitons and quantum capacitance	105
5.1	Introduction.....	105
5.2	Sample and measurement details.....	109
5.3	Results and discussion.....	111
5.3.1	Photocapacitance oscillations and their correspondence to excitons..	111
5.3.2	Origin of quantum capacitance and its correspondence to excitons..	118
5.3.3	Further analysis and results to understand the physics of oscillation..	121
5.4	Conclusions.....	124
6	Summary and future directions	125
6.1	Conclusions.....	125
6.2	Future plans.....	130

Abstract

Semiconductor science and technology has experienced a giant leap in the last few decades due to the invention of sophisticated instruments for efficient growth of semiconductor materials. These eventually facilitated the growth of few nanometers thin, uniform epitaxial layers and heterostructures with precise control of charge carriers even at such small length scales. All these had allowed physicists to explore and manipulate quantum properties of semiconductor structures for both basic physics studies and to realize novel technological applications. Excitons are one of the most commonplace and elementary excitations happen in semiconductor systems. Contributions of these excitons become even more interesting in quantum heterostructures due to experimental detection of excitonic electro-optical effects and large non-linear optical effects even at room temperatures. Nevertheless, past studies of excitons mostly focussed on studying its optical properties. However, excitons as a composite quasi particle of negatively charged electron and positively charged hole always possess electric dipole moments. Thus probing the dielectric polarization of excitons using various opto-electrical techniques will be helpful to explore the many-body physics of semiconductor heterostructure devices.

Here, in this thesis, we mainly aim to probe this inherent dipolar nature of these excitons using voltage and frequency-dependent capacitance and photocapacitance measurements in quantum heterostructure devices. We would like to mention here that these techniques of sensing dielectric polarization of excitons were not commonly used in the past. We also reiterate and explain why some population of excitons in quantum-confined heterostructure of III-V semiconductors can survive at high enough temperatures such that thermal energy $k_B T$ is more than the binding energy of excitons. This is in contrast to widespread misunderstandings of treating excitons as mostly low-temperature objects.

We also demonstrate that voltage-activated rate processes can actually mimic the standard temperature-dependent activation of defect related transitions in case of excitons. Experimental observation of voltage modulated ‘negative activation energy’ is connected with the presence of excitonic bound states in quantum confined laser diodes, which is a novel approach to probe such excitonic bound states. Estimated binding energy of excitons using such methods also corroborates previously reported values for these III-V materials. Thereafter, we extend this line of investigation to probe electrical signature of excitonic Mott transition in these light emitting quantum heterostructures.

Moreover, phot capacitance spectroscopy was hardly used to probe and understand the applied bias induced changes in dielectric polarization of spatially indirect excitons. We demonstrated for the first time that one can detect distinct indirect excitonic signature in the bias induced phot capacitance spectra in single barrier GaAs/AlAs/GaAs heterostructure system at room temperature. Variation of excitonic peak energy with applied bias allows us to estimate the dipole moments and polarizability of these small populations of spatially indirect excitons. Excitonic dipole moment and applied electric field were found to be oppositely oriented in these single barrier structures. Furthermore, excitonic many-body states like indirect trions, Fermi-edge singularities were also experimentally detected by us using phot capacitance spectroscopy at a relatively higher temperature of 100 K which was not possible using photoluminescence (PL) method. This certainly indicates better sensitivity of the phot capacitance based dielectric polarization measurements to sense these excitonic complexes in comparison to PL.

We further study interactions between zero-dimensional (0D) and two dimensional (2D) quantum structures wherein InAs quantum dots were embedded inside AlAs barrier within a GaAs/AlAs/GaAs heterostructure. Distinct, periodic quantum oscillations with peaks and valleys in the bias-driven phot capacitance and photocurrent measurement were observed at 10 K. Correspondingly, we noticed periodic presence and absence of sharp, prominent excitonic signatures in the phot capacitance spectra in the peak and valley voltages, respectively. This observation indicates critical involvement of excitons in generating such interesting coherent oscillations. We explain these oscillations due to the involvement of coherent resonant tunnelling of mostly electrons between quantized energy levels of InAs quantum dots and the GaAs triangular quantum wells in this coupled 0D-2D quantum structure. Moreover, quantum nature of phot capacitance and its correspondence to excitonic Bohr radius is also experimentally demonstrated in the same heterostructure system.

Finally, we want to emphasize that further detailed understanding of such microscopic dynamics of excitons and excitonic complexes will certainly be possible using these sensitive capacitive measurements. Therefore, we propose that capacitance and phot capacitance spectroscopy may turn out to be quite useful experimental techniques to explore the many-body physics of dipolar excitons in quantum heterostructures. We sincerely hope that research methods and observations included in this thesis will thereby be able to fulfil some of these long-cherished goals of excitonic condensed matter system by revealing how such dipolar

excitonic complexes can be sensed, probed and experimentally controlled using these tools, to begin with.

List of Figures

1.1	Energy band-structures of GaAs and Si.....	5
1.2	An energy band profile of p-n junction diode under zero bias condition.....	9
1.3	A schematic representation of the density of states for low dimensional structures including bulk.....	13
1.4	Variation of lattice constants for different materials, band-offsets, and electron affinities.....	14
1.5	Different types of band alignments in heterojunctions.....	15
1.6	Energy band diagram for semiconductor heterostructures device.....	16
1.7	Energy-momentum dispersion relation for excitons.....	21
1.8	Absorption spectra of excitons in bulk GaAs.....	24
2.1	Experimental set-up for impedance spectroscopy.....	30
2.2	A schematic representation of optical measurement set-up.....	31
2.3	A sketch of the experimental set-up for photo-induced electrical measurement.....	32
2.4	Images of copper sample holders and heaters for low-temperature measurement.....	34
3.1	Schematic diagrams to understand activation energies.....	38
3.2	A schematic picture of excitonic Mott transition.....	39
3.3	Capacitance vs. frequency for different forward bias regimes.....	44
3.4	Applied voltage-dependent differential capacitance response.....	45
3.5	Current and electroluminescence light intensity is measured for applied forward bias.....	47
3.6	Configurational co-ordinate diagram and exciton binding energy.....	49
3.7	Differential capacitance response for different temperature.....	52
3.8	Estimated photon flux as function of injection current.....	53
3.9	Electroluminescence spectral data for different injection current and temperature.....	54
3.10	Differential capacitance response for InGaAs/GaAs QDs.....	57
3.11	Estimated average excitonic binding energy for InGaAs/GaAs QDs.....	58
4.1	Energy-Momentum (E-k) diagram of bulk GaAs and AlAs.....	61
4.2	Schematic energy band diagrams of p-i-n single barrier GaAs/AlAs/GaAs.....	62
4.3	A simplified picture of the interaction of dipole and electric fields.....	65
4.4	Photoluminescence intensity versus energy for a fixed excitation intensity to understand trions.....	67
4.5	A schematic of the p-i-n single barrier heterostructure sample.....	70

4.6	DC photocurrent and phot capacitance measured with respect to the applied bias.....	72
4.7	Photocapacitance and photocurrent spectra for different biases at room temperature...	73
4.8	Schematic energy band diagrams for an 8 nm single barrier p-i-n device.....	75
4.9	Photocapacitance spectral redshift and excitons Bohr radius.....	78
4.10	Power-law variation with photon flux.....	80
4.11	Fowler-Nordheim plot and estimated spectral broadening.....	82
4.12	Photocapacitance as a function of frequency for different voltages.....	83
4.13	Photocapacitance spectral variation with the applied reverse bias at 100 K.....	87
4.14	Energy band diagrams under the presence of light and reverse bias.....	88
4.15	A 2D colour contour plot of photocapacitance spectra for different applied voltages..	94
4.16	Splitting energy (ΔE) between exciton and trion peaks with Fermi energy.....	96
4.17	DC-photocurrent spectra are compared with photocapacitance and photo- G/ω spectra.....	98
4.18	Bias dependent photoluminescence measurement is carried out at 100 K.....	99
4.19	Excitation intensity-dependent photocapacitance spectra.....	100
4.20	Temperature and voltage dependent photocapacitance and photocurrent spectra.....	103
5.1	A standard energy band diagram and current-voltage plot of a normal tunnel diode...	105
5.2	A schematic energy band diagram of double barriers resonant tunnelling diode.....	106
5.3	A sketch of multi-layered p-i-n heterostructure device.....	110
5.4	Photocapacitance oscillation with applied voltage.....	111
5.5	Photocapacitance spectra for different peak and valley voltages.....	113
5.6	Quantum capacitance and corresponding excitonic Bohr radius for three peak voltages.....	120
5.7	Photocapacitance oscillations with excitation wavelengths for low forward bias.....	122
5.8	Photocapacitance spectra measured at two different forward bias values.....	123
5.9	Comparisons of Photocapacitance, photocurrent, and photo- G/ω oscillations.....	124

List of Tables

1.1	List of materials with respective bandgaps and temperature constants.....	6
4.1	Basic parameters of GaAs and AlAs are tabulated for experimental analysis.....	61
5.1	Energy levels of electron in TQW for different peak voltages.....	115
5.2	Energy difference between two peaks in the spectra taken for peak voltages.....	116
5.3	Theoretical and experimental comparison of energy shift for successive peak voltages.....	117

Fundamental Constants used for calculations

Boltzmann constant (k_B)	$1.3807 \times 10^{-23} \text{ Jk}^{-1}$
Planck's constant (h)	$6.626 \times 10^{-34} \text{ Js}$
Reduced Planck's constant (\hbar)	$1.0546 \times 10^{-34} \text{ Js}$
Speed of light in free space (c)	$2.9979 \times 10^8 \text{ ms}^{-1}$
Permittivity of free space (ϵ_0)	$8.854 \times 10^{-12} \text{ Fm}^{-1}$
Charge of an electron, (e)	$1.6022 \times 10^{-19} \text{ C}$
Bohr radius of hydrogen (a_H)	$5.292 \times 10^{-11} \text{ m}$
Mass of free electron (m_0)	$9.109 \times 10^{-31} \text{ kg}$
Avogadro number (N_A)	$6.022 \times 10^{23} \text{ mol}^{-1}$

Chapter 1

Introduction

1.1 Motivation

With time, improvements in technology have become an essential part of humankind, where peoples are strongly dependent on technological breakthroughs. One of the most crucial building blocks behind this technological progress is the development of semiconductor physics. According to famous law by Gordon Moore, number of transistors that can be placed on a chip would double every two years. Therefore, in the last few decades, we have seen miniaturization of semiconductor device sizes: a transition from microelectronics to nanoelectronics^{1,2}. Due to the advent of sophisticated growth techniques like Molecular Beam Epitaxy (MBE), Metal-Organic Chemical Vapour Deposition (MOCVD), etc. it is possible to grow such high-quality semiconductor quantum heterostructures like quantum well, Quantum dot, single barrier tunnel diode, etc. Not only the size of device structures reduces but also the efficiency and performances of these heterostructures are enhanced a lot due to quantum confinement of charge carriers. Although these structures are studied extensively by researchers in the last few decades, many-body condensed matter physics of electron-hole bound pairs or excitons inside these heterostructures still lacks complete understanding.

Semiconductor optoelectronic devices like light-emitting diodes (LEDs), laser diodes, photodetectors, solar cells, etc. are an inevitable part of our day to day basis life. Better understanding of underlying physics and carrier dynamics inside these devices will always be helpful to improve the efficiency of the same. Most of these semiconductor heterostructures devices also possess an interesting quasi-particle called excitons, which are Coulombic bound state of electrons and holes. Presence of these excitons dominates both absorption and light emission in these heterostructure devices. Usually, these excitons are having very short lifetimes (\sim ps) and small binding energy (\sim few meV) in III-V complex semiconductor materials like GaAs, InAs, etc. So, studying the physics of excitons in bulk semiconductors at room temperature (\sim 26 meV) is hardly possible as they mostly dissociate under large thermal fluctuations. But due to the progress of growth facilities, quantum heterostructures of these materials can certainly provide strong enough quantum confinement that allows excitons to survive even at room temperature. Although, in III-Nitride materials, excitons binding energy is sufficiently large to detect its features at room temperature³. Recently, there are some more

exciting materials like organic-inorganic perovskites^{4,5}, 2-dimensional transition metal dichalcogenides (TMDC)⁶, etc. which have exciton binding energy quite high compared to the thermal energy of room temperature. Henceforth, these materials have even better potentials for optoelectronic applications⁷ of excitons at room temperature.

Mostly, excitons are explored by researchers using standard optical based methods like photoluminescence (PL), absorption spectroscopy, etc. whereas the understanding and studying of their electrical signatures are very recent and few. Moreover, due to their intrinsic dipolar character, they are expected to respond in any dielectric measurement by electrical means⁸. In this thesis, we are mainly focussed on exploring different dielectric polarization behaviours of excitons in III-V semiconductor heterostructures devices in different temperature and frequency regimes. We provide some interesting insights and new experimental signatures of excitons which were not addressed previously. Photocapacitance based optoelectronic approach has now been established by us as a sensitive technique to detect many-body physics of indirect excitons at the interface of heterostructure, which is not possible using standard PL technique.

In this chapter, we will discuss the basics of semiconductor physics, quantum heterostructure, excitons, etc. which will be helpful to readers to understand the novelties of the following chapters.

1.2 Basics of semiconductor physics

A very lucid definition of semiconductor is a material having electrical conductivity (10^2 to 10^{-8} S/cm at room temperature) which is somewhat in between metals and insulators⁹. Also in terms of energy bandgap, we generally define semiconductor as having bandgaps up to 4 electron volts (eV), whereas metals are having hardly any bandgap and insulators usually have bandgap more than 4 eV⁹. There are some common semiconductors like Silicon (Si), Germanium (Ge) which people are most familiar with. They belong to group IV in the periodic table. Their crystal structures mimic diamond lattice structure where four nearest neighbour atoms are covalently bonded with each other. Over the decades, Si has turned out to be the main building block of today's electronics industry. However, the lowest energy gaps in both Si and Ge are indirect bandgap and therefore, these materials are inefficient light emitters in their bulk forms. Beside these elementary semiconductors, there are compound semiconductor

materials which also possess enriching physics and interesting optoelectronics applications.

1.2.1 Compound semiconductors

When individual elements from group III and group V are allowed to bind together, they form a III-V semiconductor – also called as binary compound semiconductors. Among many such binary compounds, most frequently used important alloys are Gallium Arsenide (GaAs), Indium Arsenide (InAs), Aluminium Arsenide (AlAs), Gallium Phosphide (GaP), Gallium Nitride (GaN), etc. Similarly, there are other binary semiconductor compounds which form by combining group II and group VI elements like Cadmium selenide (CdSe), Cadmium sulfide (CdS), Cadmium Telluride (CdTe), Zinc selenide (ZnSe), Zinc sulfide (ZnS), Zinc Oxide, etc. Energy bandgaps of these materials are such that the excitation and emission spectra mostly cover the whole spectrum range starting from ultraviolet to far-infrared region. Ternary and quaternary versions of these alloys like $\text{Al}_x\text{Ga}_{1-x}\text{As}$, $\text{In}_x\text{Ga}_{1-x}\text{As}$, AlGaInP, etc. were also studied and used in various applications. Importance of these compound semiconductors lies in the fact that one can tune the bandgap of these semiconductors by varying alloy composition ratio of the individual elemental components. Heterostructures of these compound semiconductors play an essential role in our optoelectronics technology starting from solar cells, LEDs, photodetectors, to diode lasers, etc. Thus, having only a few compounds and their heterostructure, it is possible to cover up a wide range of wavelength of the electromagnetic spectrum⁹.

Most recently, two new types of compound semiconductor materials have shown very interesting optoelectronic properties. Presently, substantial numbers of research groups over the globe are focussed and concerned in investigating these two new classes of materials. Organic and inorganic perovskite materials^{4,5} like Cesium Lead Halides (CsPbX_3 ; X=Br, Cl, I), Methylammonium Lead Halides ($\text{CH}_3\text{NH}_3\text{X}_3$), etc. are one such group of semiconductor materials. Beside these, nowadays, two dimensional (2d) transition metal di-chalcogenide^{6,7} materials have become quite attracting because of their exciting physical properties. Moreover, research efforts in Oxide semiconductors like ZnO and Ga_2O_3 are also picking up over last few years.

1.2.2 Basics of energy bands and energy bandgap

The origin of energy bands and corresponding energy bandgaps need to be thoroughly understood in order to explain the physics of semiconductors. Every single atom consists of quantized energy levels. These energy eigenvalues can be found using quantum mechanics. Now, as per the Pauli exclusion principle, no two electrons can have the same quantum numbers, i.e., they cannot share the same energy levels. When large numbers of such atoms come closer and arrange themselves in a regular periodic fashion, then their energy levels start merging, and energy bands form^{10,11}. In a semiconductor, the outermost unoccupied energy levels which form a band is called conduction band (E_C). Whereas, the occupied energy levels inside a semiconductor form energy bands, called valence band (E_V). The forbidden energy gap between minima of the conduction band and maxima of the valence band is termed as energy bandgap (E_g).

There are different models and theories to understand the energy-momentum (E-k) relationship in a semiconductor. Like, nearly free electron approximation, tight-binding model, Kronig-Penney model, k.p perturbation theory, orthogonalized plane-wave method¹¹, the pseudopotential method, density functional theory (DFT), Hubbard model, etc. are significant methods which were used to approximate the energy band diagram of a semiconductor⁹. However, we will not go into details of any of these methods to explain band diagrams and their advantages and disadvantages, which by itself is a vast topic of research. One of the simplest and basic models of band structure uses Bloch theorem which asserts that if the potential energy $U(r)$ of a crystal is periodic then the corresponding solution of Schrodinger equation will also follow the same periodic nature, called Bloch functions. Accordingly, one can solve the Schrodinger equation using above theorem and get the energy-momentum distribution.¹⁰

$$\left[\frac{-\hbar^2}{2m^*} \nabla^2 + U(r) \right] \psi(r) = E\psi(r) \quad (1.1)$$

Here, \hbar is the reduced Planck constant, m^* is the effective mass of carriers, $\psi(r)$ is the wave function of the particle. Now, for a crystalline semiconductor structure having a periodicity of R , corresponding potential energy and wave function will follow the relation as per Bloch theorem¹¹,

$$U(r) = U(r + R) \text{ and } |\psi(r)|^2 = |\psi(r + R)|^2 \quad (1.2)$$

and the momentum and energy of the electrons can be written as,

$$\mathbf{p} = \hbar\mathbf{k} \quad \text{and} \quad E(k) = \frac{\hbar^2 k^2}{2m^*} \quad (1.3)$$

respectively. To get an overview, how the energy band diagram looks like we present here the band diagram of the two most popular semiconductor materials silicon (Si) and Gallium Arsenide (GaAs) in figure 1.1.

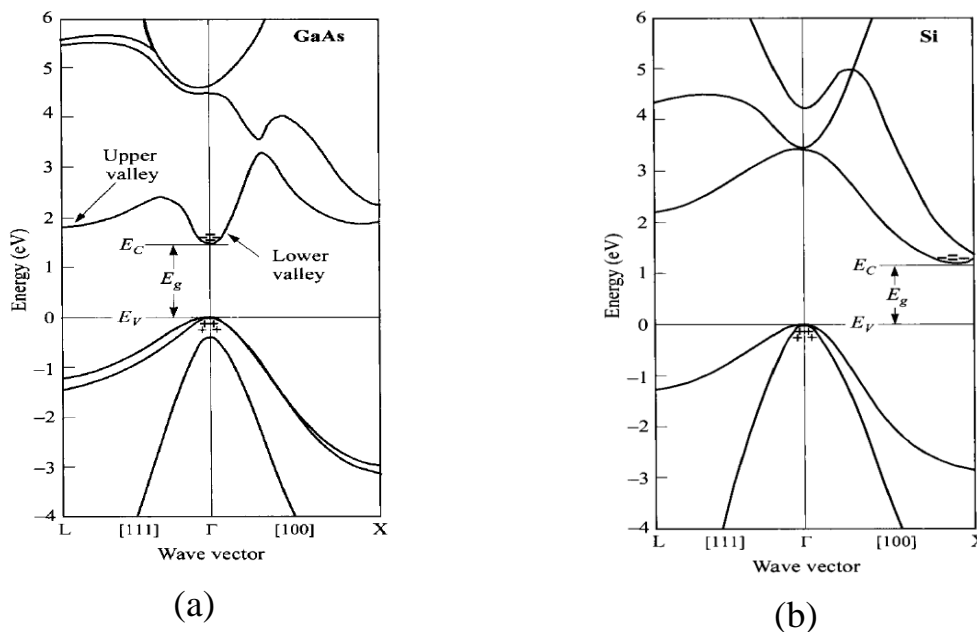


Figure 1.1: Energy band-structures of (a) a direct bandgap material GaAs, (b) an indirect bandgap material Si (both taken from reference 10). E_C and E_V are the conduction and valence band minima and maxima, respectively. E_g is the energy bandgap between two extremums. (+) and (-) signs correspond to the presence of holes and electrons in respective bands. Wave vector $k = 0$ denotes Γ point of the band diagram.

Corresponding energy band gaps of these two materials at room temperature are 1.12 eV for Si and 1.42 eV for GaAs. Now, these bandgaps are highly dependent on temperature and doping concentrations. As the effective temperature of the system is decreased, corresponding energy bandgaps usually increase following the famous Varshni model¹²

$$E_g(T) \approx E_g(0) - \frac{\alpha T^2}{T + \beta} \quad (1.4)$$

where $E_g(0)$, is the energy bandgap at zero temperature, α , and β are materials constants. Here, in table 1.1 we write down the values of these constants for different materials^{10,11} which are extensively used in this thesis.

Table: 1.1: List of materials with bandgaps and temperature constants.

Materials name (Bulk)	Type of bandgap	$E_g(300\text{ K})$ (eV)	$E_g(0\text{ K})$ (eV)	α eV/K	β (K)
Si	Indirect	1.12	1.169	4.9×10^{-4}	655
GaAs	Direct	1.42	1.519	5.4×10^{-4}	204
AlAs	Indirect	2.16	2.239	6.0×10^{-4}	408
InAs	Direct	0.36	0.420	2.5×10^{-4}	75

Now, depending upon the band structure, we can classify two different types of band gaps; one is called direct bandgap, and other is the indirect bandgap. Based on energy-momentum diagram, when minima of the conduction band and maxima of the valence band remain in the same wave vector ($k=0$; Γ point) position, then this is named as direct bandgap. Here, in figure 1.1(a), we have shown the energy band diagram of GaAs as an example of a direct bandgap. When maxima and minima of the conduction and valence bands are not in the same wave vector position respectively, then we term this as indirect bandgap material. Si is a good example of indirect bandgap material, and in figure 1.1(b), we see that the conduction band minimum is at X valley whereas the valence band maximum is at Γ valley, so they are indirect by nature. In case of direct bandgap materials, electrons and holes can make optical transitions from one band to other when the incident photons have energy $h\nu \geq E_g$, ν is the frequency of light. During absorption and emission processes, the overall momentum remains a conserved quantity for direct transitions as the photon momentum is considered negligible compared to the electron momentum. Thus, the transition probability of electrons and holes is stronger in a direct bandgap material. In comparison, extra phonon momentums are required to compensate for the mismatch of electron wave vectors during optical transitions in the indirect bandgap materials. Thus the transition efficiency becomes less. Direct bandgap materials are considered as better candidates for light emitting devices like LEDs, laser diodes as well as in case of solar cells, photodetectors as compared to indirect bandgap materials.

Effective-mass: The concept of free particles is widely addressed in physics, but, in reality, most of the carriers (especially electrons and holes in this context) are not free at all inside a crystal. Accordingly, these scatter from crystal potentials, impurity potentials, phonons inside these bulk materials. Hence, the motion of the carriers inside such crystals are redefined in terms of their ‘effective mass (m^*)’ in individual energy bands. Effective mass depends upon

the curvature of these bands and it can be written in the simplest form¹⁰ (although it is a tensor) as

$$\frac{1}{m^*} = \frac{1}{\hbar^2} \frac{d^2E(k)}{dk^2} \quad (1.5)$$

From this expression, it is quite evident that the effective mass of particles highly depends upon the curvature of bands; higher the curvature lower is the effective mass and vice versa. In the above band structure of GaAs shown in figure 1.1(a), the valence band maxima at Γ point show two parabolic energy dispersion having different band curvatures. As per the above expression, the outer parabola has less curvature, thus higher effective mass. So, this is called the heavy-hole band. The higher curvature and inner parabolic band is termed as the light-hole band. In addition, there is another energy band below the light-hole band in GaAs band structure which is called the split-off band which happens due to spin-orbit coupling in the band. Although, in the present contexts, we are not concerned with the details of the mechanisms of such band formations and assignment of their electronic angular momentums.

1.2.3 Doped semiconductors and Fermi level

A pure semiconductor has few free carriers (electrons and holes) of the order of $\sim 10^{11}$ cm^{-3} . This type of semiconductor is called intrinsic semiconductor. Due to this less density of carriers, intrinsic semiconductors hardly have any importance for technological applications until and unless the density of free carriers is increased up to a certain level. To increase the concentration of free carriers and change their electrical and optical properties, they should be doped externally to make it either electron-rich (n-type) or hole abundant (p-type) semiconductor. Now, number of electrons (n) which can occupy the states of the conduction band, can be estimated from the following equation¹⁰

$$n = \int_{E_C}^{\infty} g(E)F(E)dE \quad (1.6)$$

where $g(E)$ is the density of states near the bottom of the conduction band, E_C is the conduction band edge and $F(E)$ is the Fermi-Dirac (F-D) distribution function which defines the probability of occupation for different energy states, has the form of

$$F(E) = \frac{1}{1 + \exp[(E - E_F)/k_B T]} \quad (1.7)$$

where k_B is the Boltzmann constant and E_F is the Fermi energy level. In a pure semiconductor, where the intrinsic concentration of electrons (n_i) and holes (p_i) are same, the Fermi level lies at the middle of the bandgap at 0 K temperature. In case of a doped semiconductor, depending upon n-type or p-type, the Fermi level moves towards the band edges. For low doping concentration, i.e., when n or p is less than the density of states available and the Fermi level lies few $k_B T$ below the E_C or E_V then we call the semiconductor as *non-degenerate*. Now, in this regime, one can approximate the Fermi-Dirac distribution function as the Boltzmann distribution function at finite temperature by neglecting 1 in the denominator. In the present context, we will be dealing in the *non-degenerate* regime. For electron density (n) in the conduction band, we write the expression as¹⁰

$$n = N_C \exp[(E_F - E_C)/k_B T] \quad \text{or} \quad E_C - E_F = k_B T \ln\left(\frac{N_C}{n}\right) \quad (1.8)$$

where the effective density of state (N_C) for conduction band has the form of

$$N_C = 2 \left(\frac{m_e^* k_B T}{2\pi\hbar^2}\right)^{3/2} \quad (1.9)$$

Similarly, one can write the expression for holes in p-type semiconductor materials. Now, equating the expressions for electrons and holes, we can obtain the expression for Fermi level for intrinsic semiconductors ($n = p = n_i$)

$$E_F = \frac{E_C + E_V}{2} + \frac{k_B T}{2} \ln\left(\frac{N_V}{N_C}\right) \quad (1.10)$$

This expression implies that Fermi level will remain near the middle of the bandgap at finite temperature and it will be at the middle for absolute zero temperature for intrinsic semiconductor. Again, using the above equation 1.8 for both electrons and holes, we get the intrinsic carrier density n_i which directly depends on the bandgap of the semiconductor,

$$n_i = \sqrt{N_C N_V} \exp\left(-\frac{E_g}{k_B T}\right) \quad (1.11)$$

Knowledge of this semiconductor band structures is immensely important for electronic and optoelectronic device applications. In the next section, we will be discussing semiconductor devices.

1.2.4 Semiconductor devices

p-n junction diode: Semiconductor devices are the backbone of today's technological advancement. Growth of semiconductor devices, fabrication, and characterization for optimization of the device are the vast and important field of research nowadays. There are different types of semiconductor devices having diverse applications. Among these devices, p-n junction diode is a very simple, two-terminal device which forms the building block of semiconductor technology. Initial understanding of current-voltage relation in p-n junction diode was explained by Shockley long back around 1950¹³. Later it has been revised and modified for different systems.

A p-n junction device is formed when both p-type and n-type materials are brought closer to each other. When these two different types of materials meet at the junction, electrons from n-type recombine with holes in the p-type leaving immobile ions at the junction. This junction eventually becomes depleted of free electrons and holes and thus it is called depletion region. In addition, quasi-Fermi levels of n-type (E_{Fn}) and p-type (E_{Fp}) sides also align to a common Fermi level due to charge transfer from either side at thermal equilibrium.

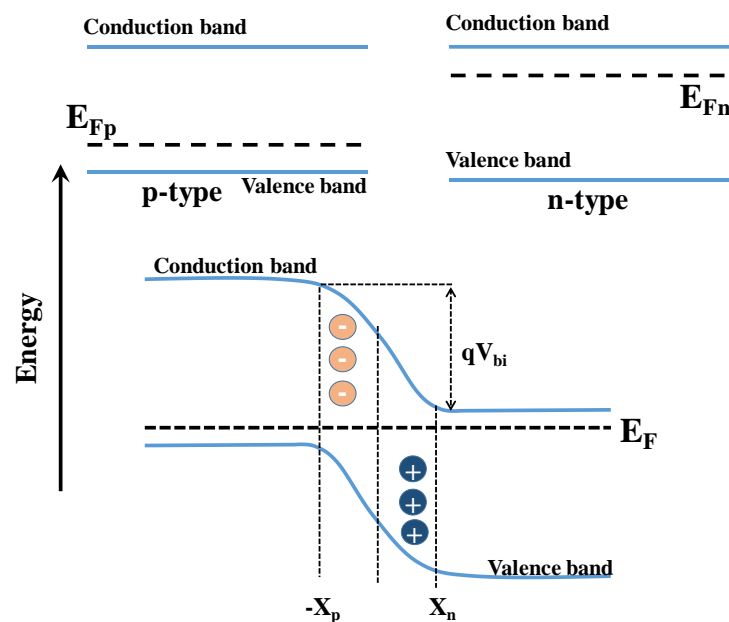


Figure 1.2: Position of quasi-Fermi levels in p-type and n-type semiconductor is shown in the upper part of the figure. An energy band profile is drawn for p-n junction diode under zero bias condition.

In this condition, it is assumed that free carrier density of electrons (n) and holes (p) are very less in comparison to the donor (N_D) or acceptor (N_A) density. Under the depletion

approximation, a built-in electric field is developed due to the present of immobile positive and negative ions. This can be calculated from solving the following electrostatic Poisson's equation:

$$\frac{d^2\phi}{dx^2} = e \frac{N_A}{\epsilon} \quad \text{for} \quad -x_p < x < 0 \quad (1.12a)$$

$$\frac{d^2\phi}{dx^2} = -e \frac{N_D}{\epsilon} \quad \text{for} \quad 0 < x < x_n \quad (1.12b)$$

Moreover, the band bending across the junction depends upon electrostatic potential developed across the depletion region. The above band alignment in figure 1.2 usually happens under zero external bias condition, and there is hardly any net measurable current flow in the circuit. Situation changes as we apply external bias to the system. Under reverse bias condition, due to the particular polarity of external bias, electrons and holes are pulled away from the junction. Thus the depletion region widens up, and there is hardly any direct current flow in the reverse bias. Although the presence of minority holes and electrons in respective n-type and p-type sides contribute tiny current flow in the circuit under reverse bias. However, the scenario changes in the forward bias. In the forward bias, carriers are injected towards the junction, and when the applied bias overcome the built-in voltage of the device and 'flat band' condition is reached then there is significant current flow in the circuit. Without going to rigorous derivation (which is not the aim of this thesis, and also discussed in any standard semiconductor book), we can write the expression of built-in voltage for a nondegenerate semiconductor,

$$V_{bi} = \frac{k_B T}{q} \ln \left(\frac{N_D N_A}{n_i^2} \right) \quad (1.13)$$

The corresponding current-voltage (I - V) characteristics for an ideal p-n junction diode is followed nicely by the following equation of Shockley¹⁰,

$$I = I_0 \left[\exp \left(\frac{eV}{k_B T} \right) - 1 \right] \quad (1.14)$$

where I_0 is the reverse saturation current. In reality, this equation is not always applicable and followed for all materials and systems. There are several reasons why this ideal relationship is not always obeyed¹⁰: (a) carrier generation and recombination at the depletion region, (b) tunnelling of carriers through energy barriers, (c) parasitic voltage drops due to series resistance, (d) the effects of surface states. Even in the case of Si and GaAs p-n junctions, the I - V characteristic does not fully follow the above Shockley equation. Moreover, the presence of surface ionic charges on semiconductor surface sometimes affects the I - V characteristic of

p-n junction. These ionic charges on the surface form image charges inside the semiconductor, thus create surface depletion region near the surface and eventually modifies the junction depletion effects. Hence, the I - V curve gets deviated from the ideal behaviour.

Besides, the I - V characteristic of a p-n junction device, there are other experimental parameters which play crucial roles to understand the underlying carrier dynamics of such a device. One of the essential measurable quantity is called capacitance. Capacitance, in general, is understood as the change in total charge (ΔQ) upon a change in the applied voltage (ΔV) i.e. $C = \Delta Q / \Delta V$. In case of parallel plate capacitor geometry, the standard expression for capacitance is $C = \epsilon A / d$ where ϵ is the dielectric constant of the material and 'A' and 'd' are area of the plate and the distance between the plates, respectively. Here, in a p-n junction device, we also have a similar geometry in the depletion region. Like, positive and negative plates in metal plate capacitor, in the depletion region, there are immobile positive and negative ions. This configuration of depletion region mimic parallel plate-like capacitor, and we term the capacitance due to depletion region as '*depletion capacitance*'. Previously, we have mentioned that depletion layer is more prominent in the reverse bias condition rather than forward bias condition. So, the concept of '*depletion capacitance*' is mostly valid in the reverse bias condition. One can also use this '*depletion capacitance*' to calculate the doping density using C - V profiling (not discussed here). In addition to this '*depletion capacitance*', there is diffusion capacitance which is significant when the device is operated under forward bias. The basic difference between these two is that former one can estimate the doping density in the depletion region, whereas the latter one can be used to calculate the injected charge density. To measure the capacitance, usually a small-signal ac voltage is applied with constant dc voltage V_0 and current density J_0 , where total voltage and current can be written as

$$V(t) = V_0 + V_1 \exp(j\omega t) \quad (1.15)$$

$$J(t) = J_0 + J_1 \exp(j\omega t) \quad (1.16)$$

where ω is the angular frequency of ac signal, V_1 and J_1 are the small-signal voltage and current density, respectively. The above two equations 1.15 and 1.16 can be used to calculate the diffusion conductance (G_d) and diffusion capacitance (C_d). The imaginary part of admittance (Y) can be written as¹⁰

$$Y \equiv \frac{J_1}{V_1} \equiv G_d + j\omega C_d \quad (1.17)$$

p-i-n junction diode: Similar to a *p-n* junction diode, a *p-i-n* diode consists of an extra intrinsic layer in between highly doped p-type and n-type layers. In comparison to the depletion region in a *p-n* diode, here this intentionally inserted intrinsic layer (*i*) play the crucial roles for the efficiency of the devices. The materials and quantum heterostructures of the intrinsic regions, hugely modify the optical absorption, emission, and electrical measurements, etc. Depending upon the type of materials and heterostructures, *p-i-n* diode has different applications and exciting physics. Due to large intrinsic region width, *p-i-n* diodes are not good rectifier¹⁰ but they are good candidates for high-frequency oscillators, fast switches, photodetector, solar cell, etc. Besides *p-i-n* diodes, there are other types of diodes like tunnel diode, Zener diode, charge storage diode, etc. which have different applications depending upon their construction. Among these, tunnel diode is more interesting and has rich physics related to quantum mechanical tunnelling process. A significant part of this thesis is based on the physics of *p-i-n* diodes and tunnel diodes. We will explore this physics of these diodes in details in the subsequent chapters.

1.2.5 Semiconductor quantum heterostructures

Physics of semiconductor and their applications have evolved enormously after the advent of semiconductor heterostructure. When the two or more materials having different properties and energy bandgaps combine to form multiple junctions, they are called heterostructures or heterojunctions. The concept of heterostructure was first developed by Herbert Kroemer, Gubanov and others around 1950-60s^{14,15}. With time technology has improved and inventions of advanced epitaxial growth facilities like Molecular Beam epitaxy (MBE), Metalorganic Chemical Vapour Deposition (MOCVD) have made it possible to grow epitaxial layers having an accuracy of few Angstroms. Later, in the year 2000, the Nobel prize in physics was given to Herbert Kroemer and Zhores I. Alferov for path-breaking experimental development of heterostructure devices.

The idea of heterostructures has opened up many avenues for experimental research. Moreover, the efficiency of the devices having heterostructures inside enhanced a lot in comparison to normal *p-n* homojunction devices. One of the important aspects is that carrier's motion can be confined and controlled using these heterostructures. When the thickness (d) of an epitaxial layer is less than the de-Broglie wavelength of electrons inside that material i.e. $d < \lambda_{de-Broglie}^{electron}$ then the motion of electrons is not allowed to access continuous energy rather

discrete energy levels. Here, we apply quantum mechanics to solve the energy levels of the electrons rather than the classical equation of motion. Since quantum mechanics governs the dynamics of carriers in these heterostructures, these can be termed as quantum heterostructures or nanostructures too. Depending upon the confinement directions and types, carriers motion and degrees of freedom can be controlled. Accordingly, we classify,

- (1) Quantum wells or 2D system: When the carriers are allowed to move freely in two directions but the motion is quantized in one direction, i.e., carriers have two degrees of freedom, then they are called quantum well.
- (2) Quantum wires or 1D system: When the carriers are allowed to move freely in one direction and motion is quantized in other two directions, i.e., carriers have one degree of freedom; then they are called quantum wire.
- (3) Quantum dots or 0D system: When the carriers are not allowed to move freely in any directions, and motion is quantized in three directions, i.e., carriers have zero degrees of freedom, then they are called quantum dot.

Whereas, in a 3D bulk system carriers are allowed to access all three directions of motions. Now, as the size of the system is reduced from bulk to nanostructures, the corresponding density of states $g(E)$, i.e. no. of energy states per unit energy interval (dN/dE) also changes significantly. In figure 1.3, the variation of density of states with energy is demonstrated from bulk to zero-dimensional structures. Moreover, the physics at lower dimension has been realised quite interesting and has humongous applications for optoelectronic devices.

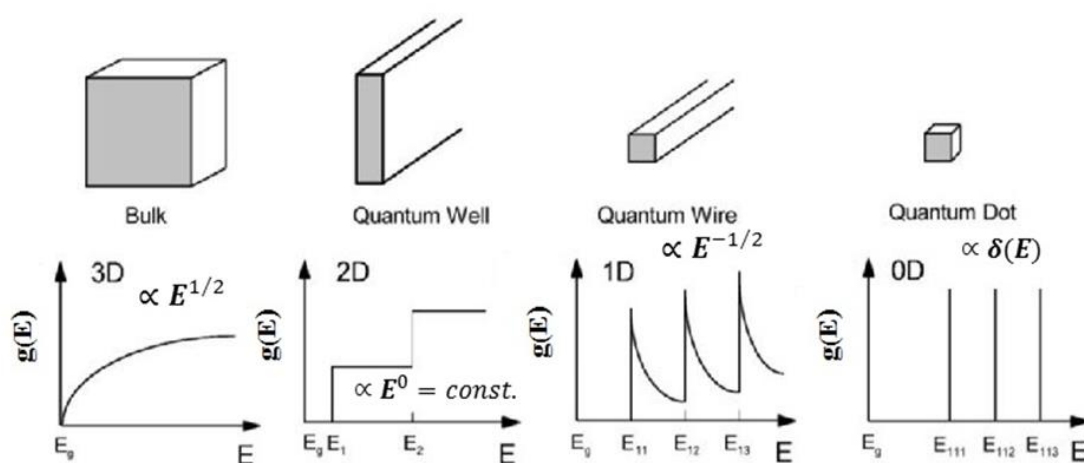


Figure 1.3: A schematic representation of the electronic density of states with energy for bulk (3D) to other low-dimensional structure (taken from reference 16).

Mainly difference in energy bandgaps of successive layers play significant roles to have quantum-confined regions; however, lattice matching between materials also have crucial impact for heterostructures. Here we will discuss how the energy bandgaps, lattice matching play important roles for these nanoscale heterostructures to form. One common example of semiconductor heterostructure uses GaAs and AlAs materials. Epitaxial growths of these two materials are easy because they have almost the same lattice constant $\sim 5.65 \text{ \AA}$. In figure 1.4(a), a group of other III-V and II-VI materials are plotted according to their bandgaps and the lattice constants. Lattice constant plays a huge role to grow good quality uniform hetero-interface as any mismatch in lattice constants introduce additional crystalline strains at the interface. As a result, electronic defects states and dislocations are also formed which may eventually affect the performance of these heterostructure devices.

We also understand that two different materials can have varying energy bandgaps E_g , work functions ϕ_m , permittivities ϵ_s , electron affinities χ , etc. We define work function and electron affinity as the energy required to remove one electron from the Fermi level E_F and from the bottom of the conduction band E_C , respectively, to the vacuum level i.e. outside of the material to make it free. Now, when two different bandgap semiconductors are merged together then at the junction due to mismatch of energy gaps there is a discontinuity of band edges at the interface.

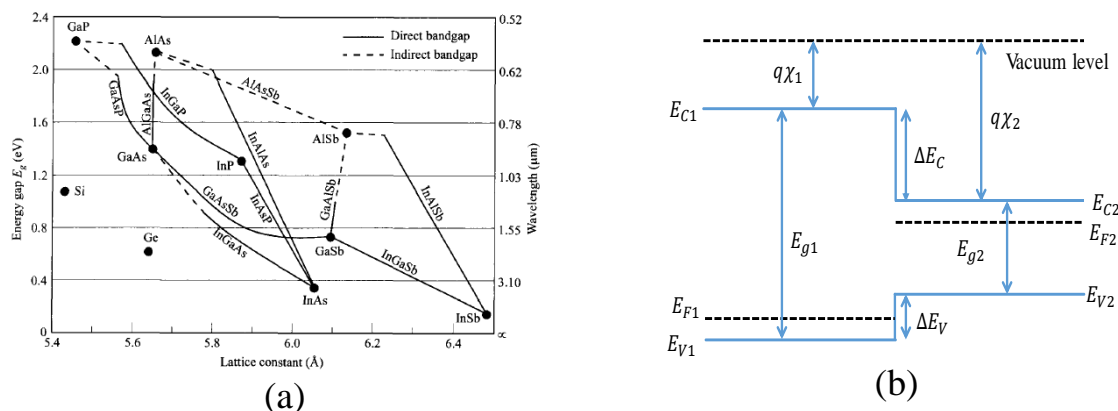


Figure 1.4: (a) Variation of lattice constants for different direct and indirect bandgap elementary and compound semiconductors (from reference 10). (b) Band-offsets and electron affinities are drawn for semiconductor heterostructure system.

These are called band offsets. There are two types of band offsets: conduction-band offset (ΔE_C) and valence-band offset (ΔE_V) across the conduction and valence-band of the

heterojunction, respectively. In figure 1.4(b), a schematic energy band diagram of heterojunction is drawn and all these above mentioned parameters are clearly shown.

We classify the different types of heterostructures based on the energy bandgaps of composite layers and position of the conduction and valence band with respect to vacuum level. Based on these, there are following categories of heterojunction interfaces^{10,17,18}:

- i) Type I interface or straddling gaps
- ii) Type II interface or staggered gaps
- iii) Type III interface or broken gaps

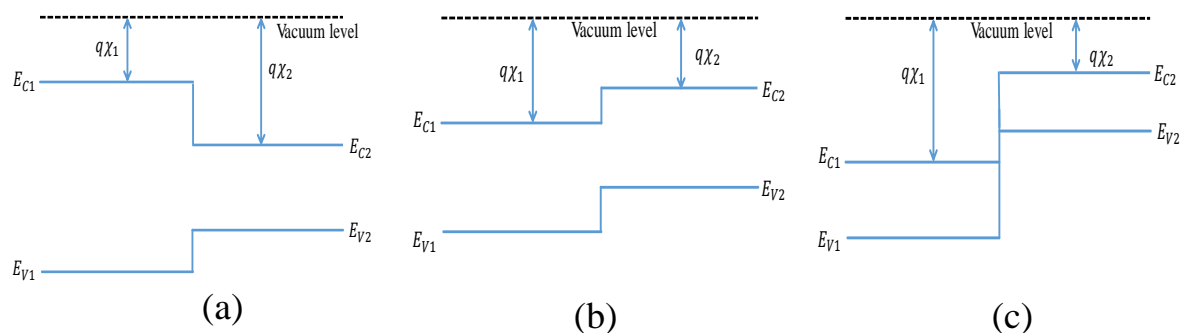


Figure 1.5: Energy bands position for different heterostructure system with respect to vacuum level are shown in (a) straddling gaps, (b) staggered gaps, and (c) broken gaps.

However, in the above schematic diagrams in figure 1.5, we have not shown the potential energy variation due to immobile ions across the interface of the doped p-n heterojunction devices. We have also ignored the depletion and accumulation of charge carriers near such interfaces. The built-in field across these heterojunction devices effectively induce the band bending similar to normal p-n device. But, in comparison to the normal p-n junction diode, here the band offsets of valence-band and conduction-band in heterojunction system play an important role for fundamental physics study as well as applications^{1,17}. Formations of triangular quantum well at the interface hugely modify the transport properties of devices. We will discuss the physics at the interface in the later chapters in more details. These band offsets are estimated based on some standard rules like Anderson's rule, common anion rule, 60:40 rule, etc¹⁰. Most of these rules are system dependent, and all of them have some limitations. However, it has been observed empirically that 60:40 rule work fine for GaAs/AlGaAs system to obtain the band offsets. This rule has the following mathematical expression,

$$\Delta E_C \cong 0.6\Delta E_g, \Delta E_V \cong 0.4\Delta E_g \quad (1.18)$$

where, ΔE_g is the difference in energy bandgaps of the two materials. In thermal equilibrium, the Fermi levels of both sides of the junction should align. Importantly, the vacuum level also bends similar to the band bending near the junction. For non-degenerate semiconductor, the band offsets hardly vary with the doping and other external parameters¹⁰. In figure 1.6, a schematic energy band diagram of heterojunction is drawn which include the effect of band bending due to the depletion field.

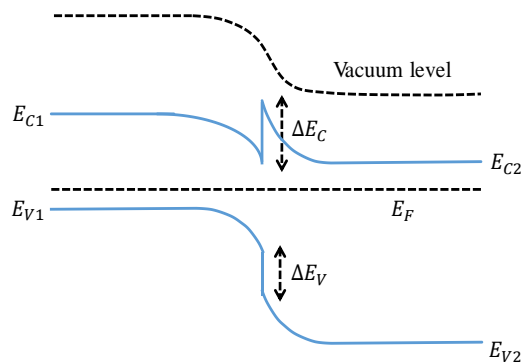


Figure 1.6: Energy band diagram for a semiconductor heterostructure device is plotted.

1.3 Excitons

Excitons as electron-hole pairs are the outcomes of most elementary excitations that can happen inside semiconductors. Two oppositely charged particles; electrons and holes bind together via electrostatic Coulomb attraction to form quasi particle states, called excitons. These bound states of excitons have finite binding energy and lifetime. Excitons also have their own individual characteristics. Excitons are Bosonic in nature due to their particular spin values. Also, finite spatial separation between electrons and holes, allows excitons to form a dipolar configuration. Thus, excitons possess inherent dipole moments. Structurally, excitons are similar to hydrogen atoms, the simplest atom in the periodic table, which can be exactly solvable using quantum mechanics. Hence, theoretical calculations of excitons can be similarly inferred from the quantum mechanical solution of hydrogen atom.¹⁹

Depending upon the strong presence of excitons, researchers classify two types of bandgaps: optical bandgaps and electrical bandgaps. In semiconductors, where exciton binding energy is reasonably high the optical bandgap is less compared to the electrical one. Electrical bandgap means we understand that the minimum energy required to excite electrons and holes

in their respective bands in semiconductor which will contribute to electrical current measurement. Whereas the excitons which are generated by optical means reside below the band edge and hardly contribute to the electrical direct current measurement. Thus, this difference is there and this effect is prominent mostly in systems where the exciton binding energy is quite high.

1.3.1 Types of excitons

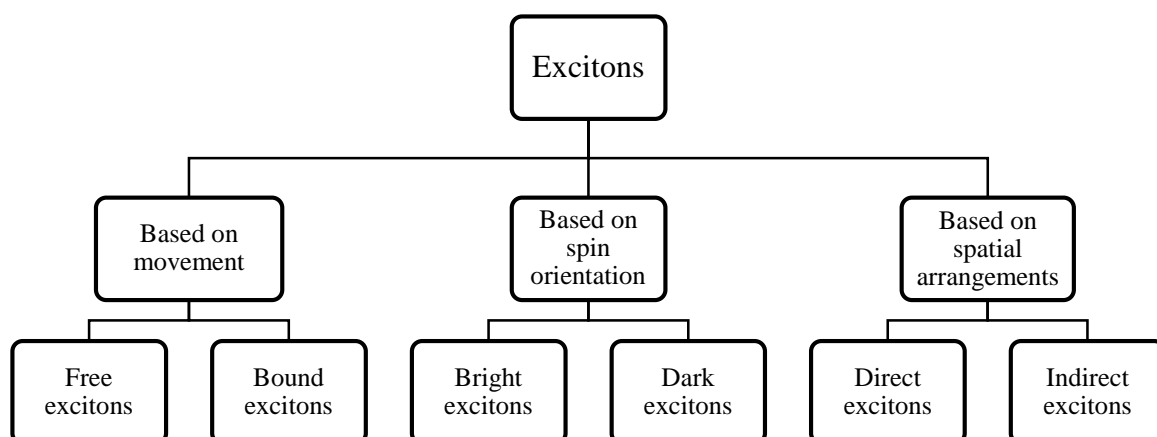
Now, there are different types of excitons based on various parameters like dielectric constant of materials, spin orientation, spatial arrangements, etc. Firstly, we will explain three basic types of excitons which are different based on their sizes, binding energy, and the materials in which these are created, etc. These are¹⁹:

- i) Frenkel exciton: Electrons and holes are strongly bound inside a molecule. Hence, their radius is very less; few Angstroms only. Due to this strong localization inside molecules, these excitons have quite high binding energy ~ few electron volts (eV). These are also called molecular excitons. Frenkel excitons mostly form in organic molecular crystals, alkali halide crystals, etc. Yakov Frenkel first introduced the concept of excitons in 1931.
- ii) Wannier-Mott exciton: In comparison to Frenkel exciton, these excitons are bigger in size, i.e. larger radius ~ few nanometers (nm). Due to higher dielectric constant, Wannier excitons are having small binding energy ~ few milli electron volts (meV) and electron and hole are separated by many unit cells inside the crystal. Most of the semiconductors are known to exist Wannier-Mott excitons.
- iii) Charge-transfer exciton: This kind of excitons are primarily found in ionic crystals. Their sizes and the binding energies are intermediate between Frenkel and Wannier-Mott excitons. Here the electrons and holes are situated within nearby molecules.

In this thesis work, we will mostly explore the physics of Wannier-Mott excitons in III-V semiconductor heterostructure devices. Before going into the details of Wannier excitons, we will first look into what are the other possible types of excitons happen and how they are important in terms of physics and applications. Based on spatial movement, there are bound

and free excitons. As the name defines, bound excitons are localized to some trap states, defects/impurity states whereas the free excitons occur mainly in a pure or defect-free semiconductor crystal. Inside the crystal, due to the presence of impurity trap states, free excitons get trapped into these states by losing their kinetic energy and form bound excitons.

There are other types of excitons which are called bright and dark excitons. Excitons are composed of two spin-half particles; electrons and holes. Now, excitons can have two spin orientations; either the spins of electrons and holes are parallel to each other in their respective bands or vice versa. Depending upon their spin arrangement and Pauli exclusion principle, optical dipole selection rule allows some transitions and forbids a few other transitions. When the spins of electrons and holes are anti-parallel to each other, this spin configuration is allowed for optical transition. Thus, this spin state is called bright exciton state. In contrast, when the spins are aligned parallel to each other, optical transitions are forbidden by dipole approximation and they are called dark excitonic state^{20,21}. Importantly, the lifetime of dark excitons is much larger $\sim \mu\text{s}$ in comparison to bright excitons.



Advent of semiconductor heterostructures allows researchers to manipulate the spatial locations of electrons and holes. By applying an external electric field, one can control the motion electrons and holes and thus makes them separated in different layers. Depending upon spatial separation of electron and hole, we classify direct and indirect excitons. When electrons and holes are formed in the same material, then we call them direct excitons. Inside heterostructures, electrons and holes can be separated into different layers of materials by external electric fields, and thus form indirect excitons. Since the electrons and holes are spatially separated, their wave functions also do not overlap. So, indirect excitons hardly

contribute to emission process and lifetime is also higher $\sim \mu\text{s}$ in comparison to direct excitons $\sim\text{ps}$.

Free and bound excitons are very common and obvious in any semiconductor system. Pure semiconductor crystals i.e. defect and impurity free systems are hardly possible. Thus, bound excitons are always there. To study the spin dynamics of any system one needs to probe the system with a magnetic field and polarized light which is out of context for the measurements presented in this thesis. Our main aim is to probe the physics of direct and indirect excitons using the so-called unconventional techniques. In later chapters, we will thoroughly discuss these experimental signatures, formation dynamics of direct and indirect excitons using some novel approaches.

1.3.2 Theoretical models of excitons

As mentioned earlier, excitons have the resemblance to hydrogen atoms. Here, electrons and holes are attracted by Coulomb force similar to proton and electron are bound in a hydrogen atom. Thus, it makes easier to solve the exciton problem theoretically. But there are two important factors which must be addressed to calculate the binding energy, dimensions of excitons or Bohr radius. Firstly, there is a substantial difference in ratio of the effective masses of electrons and holes in comparison to the ratio of electron and proton mass. Proton mass is much higher than that of hole and thus the binding energy of hydrogen atom very large compare to exciton. Another factor is the dielectric constant (ϵ) of the semiconductor which effectively reduces the attraction between electrons and holes. These two factors play crucial roles to differentiate hydrogen atom from excitons. Because of these two factors, binding energy of excitons is reduced substantially and the corresponding exciton radius increases enormously in comparison to hydrogen atom. Now, as the hydrogen problem is exactly solvable, so, one can use the expressions of energy and Bohr radius of hydrogen atom to estimate the excitons binding energy and exciton Bohr radius by replacing the appropriate values of the mass and dielectric constant of excitons. Although the above analogy of excitons with hydrogen atom gives an idea about the intra-excitonic energy levels but does not provide any estimation of excitons motion itself. Furthermore, an exciton is a two particles system where both the particles have significant kinetic motions. So, exciton dynamics cannot be explained with a one-particle picture approximation, rather need to consider as two-body problem as depicted in figure 1.7. The details explanation of two particles picture over one-particle is nicely

discussed in chapter 6 of reference 9. Usually, a two-body problem can be breaking up into two parts: a *center-of-mass* (CM) motion and *relative motion* of two particles about CM coordinate. Now, exciton CM motion under effective mass approximation will behave like free particle having $M = m_e + m_h$ where m_e and m_h are the effective masses of electron and hole, respectively. Considering the spatial coordinates of electron and hole R_e and R_h respectively, we write the Hamiltonian as

$$\left[-\left(\frac{\hbar^2}{2m_e}\right) \nabla_{R_e}^2 - \left(\frac{\hbar^2}{2m_h}\right) \nabla_{R_h}^2 - \left(\frac{e^2}{4\pi\epsilon|R_e - R_h|}\right) \right] \Phi(r) = E\Phi(R_e, R_h) \quad (1.19)$$

where $\Phi(R_e, R_h)$ is the exciton envelop function and ϵ is the relative dielectric constant of the semiconductor. Now, individual coordinates of electron and hole (R_e, R_h) can be written in terms of center-of-mass coordinate \mathbf{R} and relative coordinate \mathbf{r} accordingly,

$$\mathbf{R} = \frac{m_e R_e + m_h R_h}{m_e + m_h} \quad \text{and} \quad \mathbf{r} = R_e - R_h \quad (1.20)$$

Using the above relations and substituting these in equation 1.19, the distinct equations of motion for center-of-mass and relative coordinates take the form of

$$\left(-\frac{\hbar^2}{2M}\right) \nabla_R^2 \psi(R) = E_R \psi(R) \quad (1.21)$$

and

$$\left(-\frac{\hbar^2}{2\mu} \nabla_r^2 - \frac{e^2}{4\pi\epsilon r}\right) \phi(r) = E_r \phi(r) \quad (1.22)$$

here μ is the reduced mass of the exciton and has the expression of $\frac{1}{\mu} = \frac{1}{m_e} + \frac{1}{m_h}$. The form of center-of-mass equation 1.21 is a very well-known free particle equation. The corresponding wave function ($\psi_K(\mathbf{R})$) and energy (E_R) have the following expression,

$$\psi_K(\mathbf{R}) = \frac{1}{\sqrt{N}} \exp(i\mathbf{K} \cdot \mathbf{R}) \quad \text{and} \quad E_R = \frac{\hbar^2 K^2}{2M} \quad (1.23)$$

where $\mathbf{K} = \mathbf{k}_e + \mathbf{k}_h$ is the wave vector for exciton center-of-motion and $\mathbf{k}_e, \mathbf{k}_h$ are the wave vectors for electron and hole in the conduction band and valence band, respectively. Similarly, equation 1.22 is standard hydrogen atom problem and the solution can be written in terms of spherical polar coordinate (r, θ, ϕ) accordingly,

$$\Phi_{nlm}(r) = R_{nl}(r) Y_{lm}(\theta, \phi) \quad (1.24)$$

where $R_{nl}(r)$ is the associated Laguerre polynomials and the $Y_{lm}(\theta, \phi)$ are the *spherical harmonic* functions. Now, the total energy of excitons can be written in terms of center-of-mass motion and the intra-excitonic energy levels as^{9,19}

$$E_{nlm} = E_g - \frac{E_X}{n^2} + \frac{\hbar^2 K^2}{2M} \quad (1.25)$$

where E_g is the bandgap of the semiconductor, n is the principal quantum number, E_X is the binding energy or ionization energy of excitons which can have the following expression,

$$E_X = \frac{\mu}{m_0 \epsilon^2} \times R_y(H) \text{ eV}. \quad (1.26)$$

Here, $R_y(H)$ is the Rydberg constant for hydrogen atom which has the value of 13.6 eV. To get a simple estimation of binding energy of Wannier exciton for GaAs semiconductor i.e. $\mu = 0.058m_0$ and $\epsilon = 13\epsilon_0$, then $E_X \approx 4.5 \text{ meV}$ which is much less than the ionization energy of hydrogen atom. In figure 1.7, a schematic energy spectrum of excitons is drawn following the above energy expression of equation 1.25. An important point to mention here that as the binding energy is so small as compared to thermal energy $\sim k_B T \cong 26 \text{ meV}$ at 300 K, it is hardly possible to get the signature of excitons in bulk GaAs at room temperature.

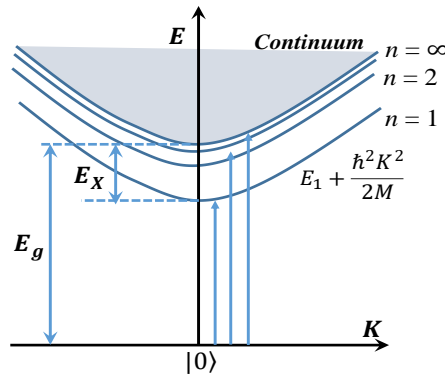


Figure 1.7: Energy-momentum dispersion relation for excitons is drawn (following reference 19). Here, K is the momentum of excitons inside the crystal.

However, if the binding energy of excitons is higher than the thermal dissociation energy, then there will always be excitonic presence. In most III-V materials except few III-Nitride semiconductors, binding energy of exciton is much less than the room temperature thermal energy. Thus, physics of excitons for these III-V materials remain always a low-temperature goal. But, heterostructures like quantum wells, quantum dots have made it possible to observe the excitonic signature even in room temperature due to the strong spatial confinement of

electrons and holes wave functions. Besides, there are other materials like TMDC, perovskites, etc. which are having a quite high binding energy of excitons more than thermal energy at room temperature. Materials having low dielectric constants have less screening effect, thus has stronger Coulomb attraction between electrons and holes and so the binding energy is higher.

1.3.3 Experimental signature of excitons

So far we have gone through the basic understanding of excitons and their theoretical backgrounds. In this section, we will discuss the possible experimental signatures of excitons and their physics. Experimental signatures of excitons are usually probed using optical methods like absorption and emission spectra, etc. These optical techniques are very well known and well established to investigate excitonic physics. However, existence of non-zero, intrinsic dipole moments, allows excitons to contribute in polarization-based dielectric measurements. In contrast to vast optical studies of excitons, much lesser amount of studies was carried out to explore these electrical signatures of excitons in the past.

Before going to the details study of optical signatures of excitons, we will briefly discuss the physics of optical transition in semiconductor. Light emission or absorption can happen in a semiconductor through transition of electron between two energy states (usually conduction and valence band energy levels) by emitting or absorbing the appropriate energy of photons. There are different types of transitions which can be detected using optical measurement. Excitonic transitions can be due to various types of excitons and they all have different signatures which we will not go into details here. There is a possibility of band to band transition between conduction and valence bands when the excitonic presence is negligible. Again there are two types of transition possible likely radiative and non-radiative transition. Radiative transition is the most dominating optical transition in direct bandgap semiconductor whereas non-radiative transition only happens for indirect bandgap semiconductor. As the position of wave vectors for conduction band minima and valence band maxima are at same point, the radiative recombination strength in direct bandgap semiconductor is higher than the non-radiative transition in indirect bandgap semiconductor. Besides, there are below band edge shallow or deep impurity states, trap states which also significantly dominate the optical spectra. All these transition processes are again strongly temperature-dependent. At the lower temperature regime, the probability of direct bandgap transition becomes higher in comparison to high temperature (room temperature). Whereas the probabilities of defects related and indirect bandgap transition decreases as the temperature of the system is lowered. Thus, the

intensity of absorption and emission spectra as well as their spectral behaviour substantially alters at low-temperature.

Now, all these transitions in semiconductors are mainly governed by famous Fermi's Golden rule. This formula is based on quantum mechanics and perturbation theory. It is frequently used to calculate the transition probability or transition per unit time from initial energy eigenstate to final energy eigenstate based on external perturbation. The probability of transition or transition rate ($\Gamma_{i \rightarrow f}$) from an initial state to final state has the following form, which is the Fermi's Golden rule,

$$\Gamma_{i \rightarrow f} = \frac{2\pi}{\hbar} |\langle f | H' | i \rangle|^2 \rho_{cv}(\hbar\omega) \quad (1.27)$$

where $\langle f | H' | i \rangle$ is the transition matrix element and H' is the perturbing Hamiltonian. The last term in the equation is called the joint density of states $\rho_{cv}(\hbar\omega)$. Density of state is commonly understood as the distribution of energy states inside a particular energy band. For optical transitions across the bandgap, one needs to consider the effect of joint density of states. It is composed of density of state of both conduction band and valence band, i.e. energy states of final and initial bands. For an optical transition with photon energy $\hbar\omega$ in a semiconductor system, joint density of state has the following form for 3D system,^{22,23}

$$\rho_{cv}(\hbar\omega) \equiv \frac{2}{8\pi^3} \int \delta[E_c - E_v - \hbar\omega] d^3k \quad (1.28)$$

where $\delta[E_c - E_v - \hbar\omega]$ function satisfy the condition of energy conservation i.e., when the energy gap between conduction and valence bands match with energy of the photon then there is a possibility of transition.

One of the important and strong proofs of excitonic signature is obtained by studying the optical absorption spectra. Usually, a photon of energy equal or more than the energy bandgap of the materials get absorbed and we see optical absorption spectra. In case of 3D bulk direct bandgap semiconductor, the absorption coefficient $\alpha(h\nu)$ depends upon the density of states following the expression¹⁹,

$$\alpha(h\nu) \approx (h\nu - E_g)^{1/2}, \quad h\nu \geq E_g. \quad (1.29)$$

This defines direct band to band optical absorption where the excitonic effect is not being considered. As discussed earlier and also shown in figure 1.7, the excitonic energy levels lie below the conduction band edge. Hence, we should expect strong excitonic absorption even

when the energy of an incident photon is less than the bandgap i.e., $h\nu \leq E_g$ and the corresponding equation for distinct excitonic absorption has the relation,

$$h\nu = E_g - \frac{E_X}{n^2}, \quad n = 1, 2, 3 \dots \infty; \quad (1.30)$$

In figure 1.8(b), we demonstrate how the band to band continuous absorption spectra turns into sharp, distinct peak like behaviour in case of GaAs material when the excitonic effect becomes prominent in the system. Due to very less binding energy of excitons in GaAs, we hardly see any excitonic effect at room temperature. As the temperature is decreased we start seeing nice and sharp excitonic peaks in the absorption spectra. Moreover, in figure 1.8(c), at very low temperature, we observe intra-excitonic transitions for $n=1, 2, 3$, etc. Also, the intensity of absorption signal diminishes as the higher-order transition ($n>1$) happens. More importantly, the presence of excitons in the system enhances the optical absorption strength a lot which effectively improves the efficiency and performance of the system.

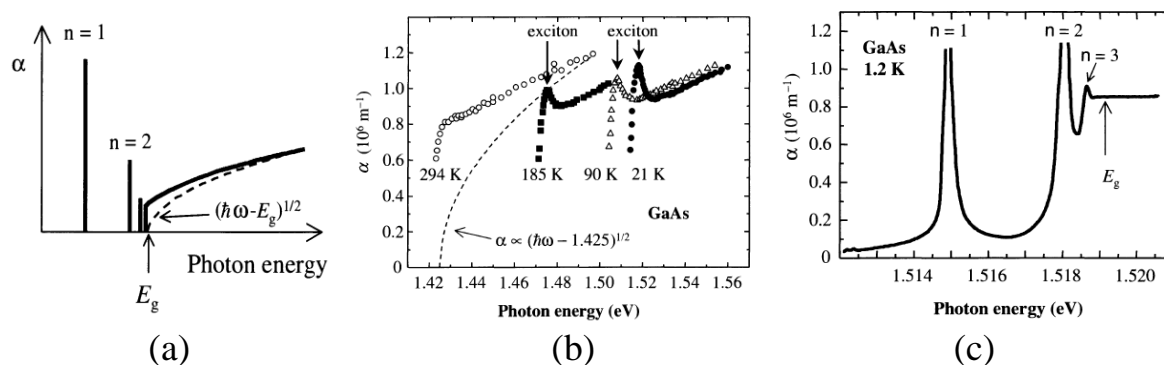


Figure 1.8: (a) A schematic of absorption spectral transition lines for direct bandgap semiconductor material. The dashed line corresponds to the absorption spectra without the excitonic presence. Presence of excitons enhance the absorption strength and show sharp resonant peaks. (b) Experimental results for bulk GaAs absorption spectra for different temperature. Sharp, resonant peaks at lower temperature bear the signature of excitons. (c) Intra excitonic peaks for pure GaAs sample at 1.2 K temperature. (from reference 23).

There are many other optical studies which also confirm the presence of excitons besides absorption study. Photoluminescence (PL) spectral approach is a very standard and well-established technique to figure out the dynamics of excitons. It has been observed experimentally that usually, the excitonic PL spectra becomes sharper in comparison to the band to band free electron-hole recombination. Although, the emission spectral features depend upon many factors like thermal broadening, Doppler broadening, collisional broadening,

lifetime broadening, etc.²⁴ Moreover, PL measurement also can be accomplished under different external perturbations which ensure to estimate various excitonic features. Like, excitation intensity-dependent integrated PL intensity follow power-law variation and the corresponding exponent value ~ 1 corresponds to excitonic presence and exponent value ~ 2 corresponds to free electrons and holes²⁵⁻²⁷. Similarly, temperature and time-dependent PL measurements can be carried out to extract important excitonic parameters.

In addition to the above mentioned optical studies, there are reports of some electrical measurements which also provide substantial experimental signatures of excitons^{23,28-30}. To probe the electrical signature of excitons, one usually uses simple p-n or p-i-n junction device configurations. In these devices, electrical bias and optical excitation or both can be employed to create the excitons. We are mostly interested to probe the physics of excitons which are generated near the depletion region or intrinsic region of the devices. Like PL, electroluminescence (EL) spectra from LEDs bears a similar excitonic signature. In the case of EL, injected electrons and holes from negative and positive terminals of a diode meet at the depletion or intrinsic region and finally recombine to produce light. Besides, these excitons also do contribute significantly in dielectric measurements depending upon the specific applied voltages and modulation frequencies⁸. There are reports of capacitance-voltage (C-V) study under the presence of light which shows peak like behaviour indicating the excitonic presence in low dimensional structure²⁸⁻³⁰. Also, researchers have seen the excitonic signature in photocurrent spectra at low temperature in GaAs p-i-n diode and dissociation of excitons under applied electric field is also demonstrated (see page no. 83 of reference 23). In our group, we first time report the signature of indirect excitons and excitonic complexes in p-i-n GaAs/AlAs heterostructure samples by measuring the photocapacitance spectra at elevated temperature^{31,32}. Moreover, this thesis is mainly based on the novel electrical signature^{8,31,32} of dipolar excitons and its complexes probed in different heterostructure devices under various optical and electrical excitations. In the respective Chapters, we will discuss these physics in more details.

1.3.4 Why study excitons?

So far, we have dealt with various aspect of excitons. But, the very obvious question which comes in our mind is that what is so important about excitons? Why researchers are so

concerned about excitons in different semiconductor system. In brief, we will review the interesting aspects of excitons and address the above concerns in this section.

As discussed earlier, an exciton is a very interesting quasi-particle because of its intrinsic dipole moment and its inherent bosonic spin state. Also, exciton has a simple structure analogous to hydrogen atom which predicts the solution of excitonic problem accurately. Firstly, in most of the semiconductors light emission is dominated by excitonic recombination, given the condition that the excitonic binding energy is higher than the thermal energy of the system. Moreover, inside quantum heterostructure, the binding energy of exciton is enhanced a lot which effectively make it easier for excitonic recombination. In addition, in case of direct excitons, emission spectra are sharper, and radiative recombination efficiency is higher due to strong resonant transition of overlapping wave functions of electrons and holes. Hence, this particle plays a huge role to increase the efficiency of LEDs, laser diodes, etc. Even, recently researchers have reported low threshold excitonic laser in monolayer MoS₂ at room temperature³³⁻³⁵.

Nowadays, excitons also have been demonstrated as a potential and efficient candidate in optical communications. A direct exciton can be generated by photon and also emits a photon when recombines. Thus it poses unique property which is essential for better optical communication. High et al. group³⁶ from the University of California, San Diego showed how one can control excitonic fluxes in an excitonic integrated circuit for efficient optical communication using III-V coupled quantum wells (CQWs) at low temperature. Whereas, in 2018, Unuchek et. al.³⁷ has studied similar physics at room temperature in TMDC heterostructure devices. Furthermore, a single exciton in a quantum dot is a ‘two-level’ system which can be utilized for quantum information processing.³⁸ Another interesting aspect is that exciton has very less exciton radius and excitonic de-Broglie wavelength is much less in comparison to the photon wavelength. Hence, excitonic circuits can be made of the scale of photon subwavelength.³⁹

Besides, excitons play important roles in the exploration of exotic condensed matter phases. Being a Boson, excitons are promising candidates for exquisite phases of condensed matter like Bose-Einstein condensation (BEC), superconductivity, superfluidity, etc. Although, these phases are experimentally realized in different atomic systems but, the critical temperatures of these phase transitions are much lower^{40,41} than our normal temperature range. However, excitons are potentially more favourable because of their low effective masses. Critical temperatures of these phase transition usually follow an inverse relation with temperatures, and thus low effective mass has higher transition temperatures. Another factor

which is also very important is the lifetime of excitons. Generally, phase transition is considered as a thermodynamic equilibrium process. Hence, thermalization time should be higher than the lifetime of excitons. As stated earlier, the lifetime excitons can be increased by spatially separating electrons and holes applying external electric field as a form of indirect excitons or by probing the dark state of excitons^{20,21}. There are numerous reports which claim the observation of excitonic BEC,⁴²⁻⁴⁶ superfluidity, superconductivity^{47,48} in a different system. Even there are theoretical works which also have showed that excitonic BEC is possible at low temperatures when experimental conditions are fulfilled. Despite these ample experimental and theoretical reports, there are contradictions regarding the signatures of excitonic BEC which is very thoroughly discussed in an article by D.W.Snoke.⁴⁹ Moreover, researchers speculate that dark excitons can also play a crucial role in BEC^{20,21,50-52} due to their high lifetime. Although, experimental evidence is still lacking towards definitive signatures of BEC of dark excitons.

Another interesting quasi-particle which can form due to strong coupling of exciton and cavity photon inside an optical microcavity, is called polariton or exciton-polariton^{53,54}. This is also a very good candidate for high-temperature BEC⁵⁵⁻⁵⁷, superconductivity^{58,59} due to small effective mass, as small as 10^{-5} times of the electron mass.⁴³ There is a recent report of polariton BEC in thermal equilibrium inside high-quality microcavity⁶⁰. Moreover, researchers have shown the experimental realization of exciton-polariton lasers^{61,62} in different materials system. Depending upon exciton binding energy in a variety of materials, exciton-polariton lasers can be operational even at room temperature.⁶¹

Chapter 2

Experimental techniques and set-ups

2.1 Introduction

The most important aspect of experimental research is to build experimental set-ups for measurements. Knowing the minute details, shortcomings, and limitations of the instruments are few crucial factors, which any experimentalist should always care about. Besides, tailor-made experimental set-ups, exploring new experimental approaches and techniques are the important goals for an experimental researcher. One should also gain in-depth knowledge of instrumentation and interfacing to set-up and design new experiments and data acquisition. In this section, we will discuss the details of experimental methods, techniques, instruments, etc. Further, we also raise questions regarding new experimental approach and methods which can detect excitons with better sensitivity in comparison to standard available techniques. Here, we would like to mention that we have employed new techniques and methods to measure and understand the interesting physics of excitons and its complexes at room temperature and low temperature in semiconductor heterostructure devices. Most of our measurements are executed on semiconductor devices like low-dimensional semiconductor heterostructure p-i-n junction diodes.

2.2 Electrical approach to study excitons

Semiconductor devices are mostly characterized based on some standard electrical techniques. Primarily, to measure the diode behaviour, one does the current (I) –voltage (V) measurement to see diode like feature in I-V data (equation 1.14 in chapter 1). Besides, there are other electrical techniques like impedance spectroscopy, deep-level transient spectroscopy (DLTS)⁶³, deep-level capacitance profiling (DLCP)⁶⁴, etc. Here, we mostly employ impedance spectroscopy technique to understand the dielectric behaviour of semiconductor junctions. In this technique, capacitance (C) and conductance (G) of the devices are measured by varying the temperature and applied modulation frequency (f) for different applied dc bias. For a semiconductor p-n junction diode, these capacitance and conductance are measured in a simplified diode circuit model where C and G are in parallel circuit connection. These C and G/ω (to make it in the same unit of capacitance, $\omega = 2\pi f$) are again the imaginary and real part of the complex impedance function (Z) respectively.

$$\frac{1}{Z} = \frac{1}{R} + i\omega C = G + i\omega C \quad (2.1)$$

Where R is the internal resistance of the device. Now, these real and imaginary parts are again connected by famous Kramers-Kronig relations^{65,66}, where one measured quantity can be used to obtain the other. As we discussed earlier, there are depletion capacitance, diffusion capacitance in semiconductor diodes, which effectively contribute to capacitance measurement depending upon applied bias, modulation frequency, temperature, etc. Moreover, we know that semiconductor heterojunctions are dominated by the presence of impurities, doping concentration, defects distribution, etc. These defects mostly form during the growth process of semiconductor heterostructure due to lattice constant mismatch, lattice irregularities, etc. Now, these defects, impurities and trap states near the band edges (conduction and valence band) inside bandgap contribute to the capacitance and conductance measurements following the standard rate equation of Arrhenius,

$$\frac{1}{\tau} = f = v \exp\left(-\frac{E_{Th}}{k_B T}\right) \quad (2.2)$$

where τ is the response time of these states, f is the frequency of the response, v is the thermal prefactor and E_{Th} is the activation energy. So, depending upon temperature and frequency modulation one can achieve the activation energy for different states which effectively affect the capacitance and conductance measurements. Although, we do not see any explicit voltage dependence in this formula, but we know, the applied voltage in a semiconductor device hugely affects the impedance measurement. Accordingly, we will see in the next chapter how applied voltage certainly relates to the activation of these impurities states and how that can be connected using the above expression. Besides, the presence of dipolar elements in the system also modifies the dielectric environment which affects the dielectric measurement. Similarly, we will see in the subsequent chapters how the presence of excitons which are intrinsically dipolar in nature, affect the capacitance measurements. Moreover, it is well-known that the response of these dipoles again has strong dependence on the applied modulation frequencies as nicely explained by Miller et. al.⁶⁶. In the low-frequency side, dipoles get sufficient time to follow the applied frequency cycle whereas in the high-frequency modulation dipoles certainly do not have enough time to track the fast oscillation, Thus, the rotation of the dipoles are not properly coupled at these two frequency limits. In the intermediate frequency regime, when the applied frequency resonantly matches with the response frequency of the dipoles then only the coupling become stronger and the maximum response happens⁶⁶.

Impedance of devices can be measured using two different approaches like Lock-in based technique and using LCR meter. In figure 2.1, we have shown a schematic of both the methods. A small sinusoidal ac signal with applied dc bias is used to measure the impedance of the device. Most of the frequency-dependent impedance measurements have been executed in our case using LCR meter. These are very standard approaches to measure the impedance of semiconductor devices. However, we will not go into detailed study to understand this mechanism.

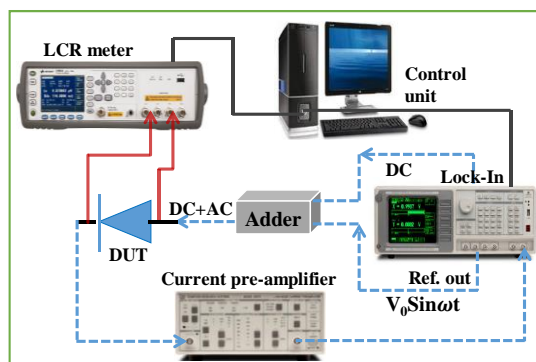


Figure 2.1: A sketch of an experimental set-up to measure the impedance spectroscopy using both lock-in based method and a simple LCR meter. The blue dashed lines indicate the connection for lock-in measurement, whereas the solid red lines show the electrical paths to measure the impedance of a device under test (DUT) using LCR meter. However, these two techniques can be employed separately to measure the impedance of a DUT.

2.3 Opto-electrical approach to study excitons

Due to having a finite energy gap, semiconductors emit light when these are optically or electrically excited. There are different optical and optoelectrical techniques which are commonly used to characterize the semiconductors. Photoluminescence (PL) and optical absorption spectroscopy are most common optical tools to understand the physics of semiconductors. In the case of PL, luminescence occurs when the semiconductors are excited by a light source having photon energy higher than the bandgap of the semiconductors. Usually, laser (light amplification by stimulated emission of radiation) is used to optically excite a sample. Emitted light is focussed at the entrance slit of the monochromator using a combination of lens and the dispersed light from the grating are detected by optical detectors. The signal from the detector is measured using a standard Lock-in based technique. For optical signal detection, we have used photodetector, photomultiplier tube (PMT). Depending upon the

wavelength of interest, there are Si, InGaAs, etc. photodetectors which work over the wavelength range 200-2700 nm. For Visible to near-infrared wavelength detection, we have used Si photodetectors FDS1010, FDS 010 from Thorlabs. We have used InGaAs photodetectors FGA 20, FGA 21 from Thorlabs for higher infrared wavelength detection. Whereas, PMT which has better sensitivity in the visible wavelength region, has been utilised to record the low signal strength in the measurement.

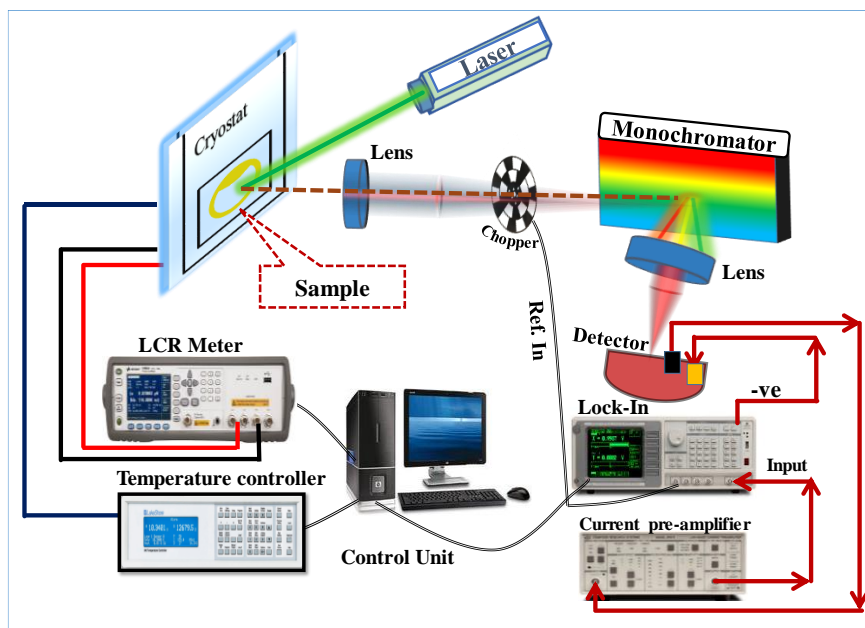


Figure 2.2: This is a schematic representation of optical measurement set-up. For PL or EL measurement one can optically excite the sample with laser or electrically apply forward bias to emit the light, respectively.

Optical absorption spectra for these type of solid-state semiconductor heterostructure system cannot be done in the transmission mode setup due to opacity of the material. So, to study absorption spectra in these samples, standard method is to probe the samples in the reflection geometry or one can employ photoluminescence excitation (PLE) approach for the same. Now, these experimental methods and its execution to extract the underlying physics are complicated and time-consuming too in comparison to the methods we use to probe the same physics. Moreover, these optical methods can be employed to study the physics of a few layers of semiconductor heterostructure or bare samples. But, as in our case, we will mostly deal with semiconductor devices with p-type and n-type junctions having many layers, above optical absorption techniques may not be applicable to probe the underlying excitonic physics. Instead,

we find opto-electrical methods more efficient and simpler to probe the same physics. Opto-electrical methods are understood as the involvement of both optical and electrical processes. This can be realized as the electrical excitation and optical detection or the vice versa. In a semiconductor light-emitting diodes, one can study the electroluminescence (EL) spectra, EL intensity with the applied biases to understand the dynamics of electrons and holes in semiconductor bands. We find the measurement of electrical parameters like capacitance, conductance, current, etc. in the presence of optical excitation more insightful and easier to execute. Moreover, these measurements of photocurrent, photocapacitance are found to be more informative and sensitive to explore the physics of excitons in heterostructures.

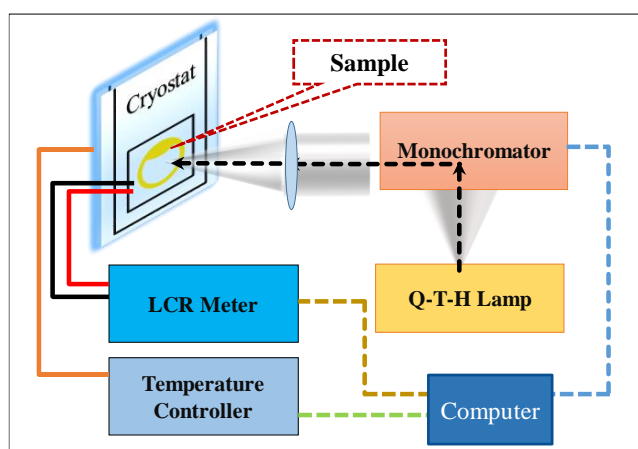


Figure 2.3: A schematic presentation of optical excitation wavelength-dependent electrical measurement. Here, the optical excitation is done using a quartz-tungsten-halogen (Q-T-H) lamp and monochromator. The electrical measurement is done using the LCR meter.

Besides, these photocurrent, photocapacitance methods are generically similar to the physics probed with the optical absorption spectroscopy. In this regard, we would like to mention that any spectroscopic measurement needs to be λ^2 corrected¹⁹ during the conversion of wavelength to energy for better accuracy. However, this effect becomes significant only when the spectra is measured over a wide range of wavelength. Most of our spectroscopic measurement are carried over smaller scanning wavelength range which does not require this correction. To measure these photo-induced electrical parameters, one can use different optical sources like laser, quartz-tungsten-halogen (Q-T-H) lamp attached with a monochromator, etc. All the electrical components can be measured using LCR meter or Lock-in based technique. Data acquisitions have been done using LabView program. The details of experimental setups are shown in figures 2.2 and 2.3.

2.4 Low-temperature system

Fascinating and interesting physics always happen in any system when temperature of the system is lowered. Depending upon materials and what physics to probe, low temperature corresponds to value of a few Kelvins to tens of Kelvins. For a semiconductor system, low temperature plays a crucial role as the bandgap of semiconductor has a strong dependence on temperature. Also, the transport properties of semiconductor devices have great impact on temperature. At low temperature, most of the defects related states get frozen and hardly contribute to electrical measurements.

There are different approaches to achieve low-temperature which depends upon the temperature of interest. In our case, we mostly work in the temperature regime of around 8 K to 300 K. To achieve the temperature range, we have used closed-cycle Helium cryocooler with model no- CS204F-DMX-20 from Advanced Research System (ARS). This is an ultra-low vibration-free ($<3-5$ nm) low-temperature system which can be used to accomplish any optical and electrical measurements. Here, ultra-pure Helium gas (99.999%) is cycled through a compressor and Gifford and McMahon (GM) cooling method is used to cool the temperature of the system. Temperature of the cold head is measured using a calibrated silicon diode sensor, model no-DT-670 from Lake Shore Cryotronics. The same is monitored and controlled by temperature controller, model no- 340 from Lake Shore Cryotronics. Moreover, the complete system needs high vacuum ($\sim 10^{-6}$ mbar) and that is accomplished by a combination of two pumps, a backing pump or scrawl pump followed by a turbo-molecular pump.

To have an accurate low-temperature measurement, one needs to be careful about proper thermal contact of samples with the cold head of the cryostat. Thus, first and important step is to make and design a suitable sample holder where the sample and temperature sensor can be placed as close as possible. Accordingly, we had designed our sample holder, and it was manufactured using pure copper material by local vendors. In figure 2.4(a), we have attached a few images of the holders. Then, it is important to make sure that the sample and sensors have good thermal contacts with the holder. There are various low-temperature thermally conducting glues (Apiezon N Grease) and soft metal (indium foil) which can be used to make better thermal contacts with the holder. Our samples were mostly mounted on a TO-5 header as also visible in figure 2.4(a). For electrical measurements, one needs to electrically isolate the sample from the copper holder such that any parasitic contributions do not affect the measurements. We have used few thermally conducting but electrically isolating tapes like

Kapton, Teflon tapes, etc. to do the same. Finally, the holder front side and samples need to be appropriately aligned with the optical window of the cryostat for optical measurement.

Another hurdle we used to face was the heater problem. To increase the temperature of the cold head, you need to put a heater in the cold head. Initially, a strip heater was provided by the company. But, when I had started working in the system, it had gone bad. Then, we had made a home build strip heater using thermally conducting Kapton tape and electrically insulated nichrome wire. Initially, it was also showing some problems and used to get burned

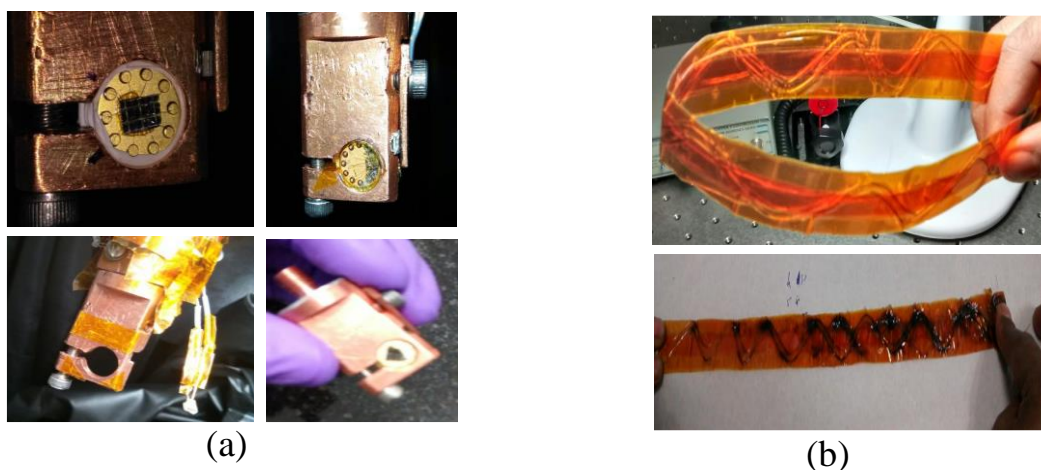


Figure 2.4: (a) Images of copper holders with and without samples. (b) A home-made cold head heater for the low-temperature system. This is made of Kapton tape and the nichrome wire.

due to local heating at the bending region. Later, we had optimized it following particular pattern (as shown in figure 2.4(b)) to avoid local heating and now, it is working fine. Even, in the last few years, we did not face any problem regarding the heater. These were the achievements and hurdles we developed and sorted out for low-temperature study. After all, for low-temperature measurements, one needs to be always cared for all the operational procedures and make sure the temperature what is displayed on the screen is same as the sample temperature. Besides these, there are other issues relating to proper vacuum, joint leak, water chiller, etc. which also had created problems and we had fixed those accordingly.

Most of the measurements were done inside the closed cycle cryostat. For electrical measurements, there are four electrical copper wires which go to the sample end and they are connected with the corresponding pins of the sample. For optical measurements, there are four optical windows which allow the light to excite the sample and emitted light is passed through

the windows for outside optics. We will discuss the low-temperature results of our samples in the respective chapters.

Chapter 3

Dielectric signature of excitons and excitonic Mott transition in quantum confined laser structures

3.1 Introduction

Excitons are most common, elementary excitations in any semiconductor as well as in quantum heterostructures. These critically influence electrical transport and optical properties of these materials and structures in various ways. Hence, studying experimental signature and application of excitons are quite essential in recent times. Moreover, being charge-neutral quasiparticles, excitons cannot contribute to direct current flow, but their inherent dipolar nature makes them capable of responding to dielectric polarization measurements like frequency-dependent capacitance, photocapacitance spectroscopy, etc. In this chapter, we inquire about the detection of experimental signature of these excitonic dipoles using similar measurements in III-V semiconductor quantum heterostructure devices. We probe the existence of excitons by measuring steady-state, small-signal, junction capacitance response in the frequency domain as carriers are injected gradually by increasing forward bias in the following III-V based electroluminescent diodes—a GaInP/AlGaInP based strained multi-quantum well (MQW) laser and an InGaAs/GaAs based quantum dot (QD) laser.

Bias dependent differential capacitance response with modulation frequency is used to trace presence of excitons in GaInP/AlGaInP based multi-quantum well laser diodes. In the lower bias side, we see standard voltage-activated defects states contribution which affects the impedance measurement. These sub-bandgap defects activation processes are usually recognized as the consequence of positive activation energy. Whereas, the occurrence of negative activation energy after light emission is understood as a thermodynamical signature of the steady-state excitonic population under an intermediate range of carrier injections. In the higher bias region, differential capacitance response falls off slowly, and after certain bias values, it vanishes. This behaviour of differential capacitance leads to gradual Mott transition of an excitonic phase into an electron-hole plasma in a GaInP/AlGaInP laser diode. This is further substantiated by exponentially looking shapes of high energy tails in electroluminescence spectra with increasing forward bias, which originates from a growing

non-degenerate population of free electrons and holes. Moreover, similar negative activation energy and its correspondence to the presence of excitons is also reproduced in another quantum-confined heterostructure system made of InGaAs/GaAs quantum dots. Such an experimental correlation between electrical and optical properties of excitons can be used to advance the next generation excitonic devices.

In the initial few sections, we will give a brief overview of negative activation energy and excitonic Mott transition which we have used thoroughly to explain our experimental results. After that, we will discuss the experimental details, samples, results, and rigorous analysis of our experimental observation on the physics of excitons.

3.2 Negative activation energy

Activation energy is a very well-known concept in the science community. Generally, whenever any thermodynamical transition (e.g. chemical reaction) occur between initial to final states, then initial states move to final states by overcoming some potential energy barriers. Activation energy usually measured as the energy difference between the final states and initial states. Mostly, people are familiar with positive activation energy where the effective energy difference between final and initial states usually become positive. However, positive activation energy can be both exothermic and endothermic for a process, as shown in the schematic diagram in figures 3.1(a) and 3.1(b), respectively. In the former case, system releases some energy in the form of heat, whereas in the latter case, system absorbs heat as a form of energy and finally complete the reaction. This extra heat or energy is understood in terms of change in enthalpy (ΔH) of the system, which can be positive and negative depending upon the process. Positive activation energy can be explained using a single-step barrier crossing analogy. Whereas, the concept of negative activation energy is very complicated and interesting too. Although the concept of negative activation energy seems not so popular to the physics community, it is a very well-known phenomenon to researchers in physical chemistry^{67,68} and biology⁶⁹, especially. Following articles by Mozurkewich et al.⁷⁰ and Muench et al.⁶⁹, we understand that negative activation energy can only be explained by considering the minimum two steps energy barriers crossing processes. In figure 1 of reference 70, authors have clearly demonstrated, how two reactants (A & B) undergo two steps activation processes having an intermediate transition state to produce the final products. It is understood that the intermediate transition state reacts in a much faster rate to have the final state whereas

reverse process of returning to the initial state is a slower process. Hence, the negative activation is realised as the consequence of the differential reaction rates of different reaction processes. Now, this rate dominated energy barrier activation process directly follows from the Arrhenius rate equation $\frac{1}{\tau} = f = \nu \exp\left(-\frac{E_a}{k_B T}\right)$. Considering the rate equation and Tolman interpretation⁷⁰, it is realised that there should be an involvement of an intermediate transition state (E_{TS}) which play a significant role for negative activation energy to occur.

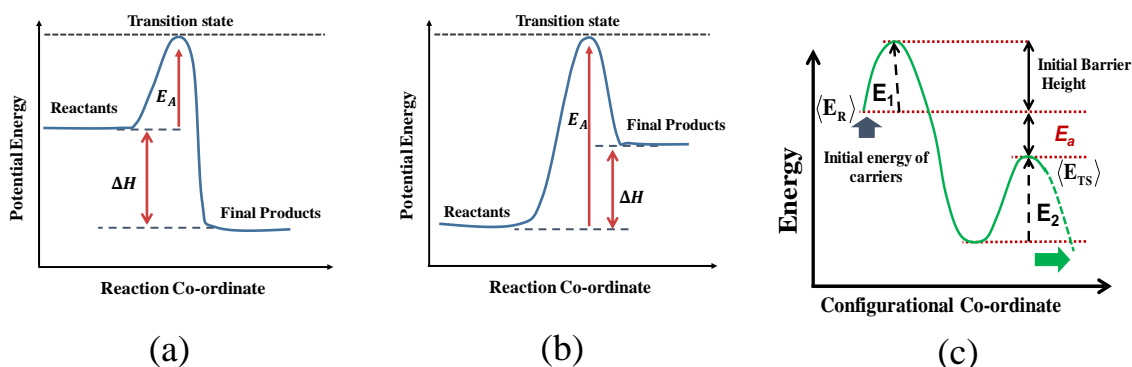


Figure 3.1: (a) and (b) Simple diagrams of exothermic and endothermic reaction processes are sketched to understand the positive activation energy mechanism, respectively. E_A and ΔH are the activation energy and change in enthalpy of the system, respectively. (c) A schematic configurational diagram is drawn to understand the negative activation energy. Here, $\langle E_{TS} \rangle$ and $\langle E_R \rangle$ are the average energy of the intermediate transitional state and initial state, respectively. E_1 and E_2 are the first and second energy barrier, respectively.

Now, activation energy can be written as $E_a = \langle E_{TS} \rangle - \langle E_R \rangle$, where $\langle E_{TS} \rangle$ is the average energy of the transitional state and $\langle E_R \rangle$ is average energy of the initial state. Here, if $\langle E_{TS} \rangle$ is less than $\langle E_R \rangle$, then the effective activation energy becomes negative. To get a better view, a scheme can be penned⁷⁰, $initial\ state \rightleftharpoons Intermediate\ state^* \rightarrow final\ state$. If the final state is a faster process compare to the initial state, then from the above Arrhenius equation it can be realized that the final transition process has lower activation energy barrier than the initial one. Thus, the effective activation energy becomes negative. In figure 3.1(c), we have drawn a schematic configurational diagram to understand the mechanism of negative activation energy. Initially, the carriers having sufficient thermal energy to cross the first activation barrier height and then before going to final lowest energy state, carriers find an intermediate stable energy state which is the second energy barrier. We will shortly understand this physics of negative activation energy in more details and try to correlate the same with the presence of

excitonic bound states in the system. Furthermore, we would also like to see whether negative activation energy can be correlated with excitonic Mott transition in laser diode.

3.3 Excitonic Mott transition

Mott transition is a phase transition from an insulating state to a metallic state or vice-versa. This is mainly a density-dependent phenomenon. However, it also depends upon other factors like temperature, pressure, doping concentrations, etc. We see examples of Mott transition in many different condensed matter systems. In semiconductors, excitonic Mott transition is one such well-known phase transition. Excitons are bound pairs of two oppositely charged carriers; electrons and holes. Due to this particular composition, excitons are inherently charge neutral in nature. Hence, they do not contribute to direct electrical current flow in the system. When these excitons are dissociated then electrons and holes become free to move and contribute to current flow. This transition from insulating excitonic phase to conducting electron-hole plasma (EHP) state mostly occur when the density of excitons crosses a critical value which is called Mott density (n_M). Usually, this Mott density (n_M) and excitonic Bohr radius (a_B) follows the relation $n_M a_B^3 \approx 1$.^{71,72} When density of excitons is less than this Mott density, then excitonic features prevail. As the density of excitons crosses n_M , then due to strong screening effect electrons and holes are not able to feel the Coulomb attraction. Thus, the bound excitonic state dissociate into free EHP state. This transition is known as excitonic Mott transition. In figure 3.2, we draw a schematic picture to get an overview of this phase transition. Although, the concept of Mott transition had been realized by N F Mott around 1949,^{73,74} still, it requires more theoretical and experimental study to realize the same for

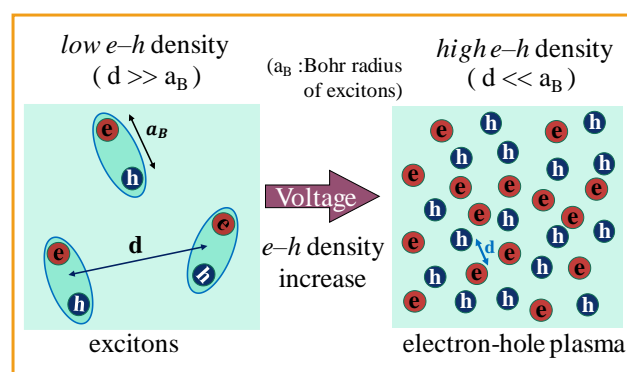


Figure 3.2: A schematic representation of the excitonic Mott transition is presented. Here, 'd' is the inter particles distance. Voltage is used to increase the carrier density.

semiconductor system, as also mentioned in the reference 75. However, there are numerous theoretical^{76,77} and experimental⁷⁸⁻⁸⁰ reports on excitonic Mott transition. Theoretical calculations are based on different interaction terms, screening, etc. which are very prominent in the higher density limit. Accordingly, there are different approximations and models to explain the excitonic Mott transition. Debye-Hückel (DH) and Thomas-Fermi (TF) screening formulas are very well-known in explaining Mott transition in a different regime of exciton density⁷². These two screening formulas have two regimes of application. Usually, Debye-Hückel formula is applicable when the thermal energy of the system is high and the carrier dynamics follow the classical Boltzmann statistics. We will utilize this Debye-Hückel formalism to estimate the exciton Mott density at room temperature⁷² to understand the excitonic Mott transition in our experimental results. Whereas, Thomas-Fermi model mainly works for a degenerate electron-hole gas system at low temperature. Due to the strong excitonic interaction in the higher density side, the effective bandgap of the semiconductor also gets affected which is known as bandgap renormalization. Usually, the bandgap decreases as the excitonic density increases. This is described based on a dimensionless quantity r_s which depends on the volume of an exciton and a volume occupied by carrier pair in the plasma state⁷²,

$$r_s = \left(\frac{4\pi a_B^3}{3} n_p \right)^{-1/3} \quad (3.1)$$

where, n_p is the plasma density. This r_s values lie in between 1 and 4 for the semiconductor system in EHP state.

Experimentally, one should see the spectral peak redshift during Mott transition due to bandgap renormalization effect⁷². Spectral width broadening also happens due to strong interaction in the higher density limit. Beside these experimental signatures of Mott transition, the high energy spectral tail follows Boltzmann statistics, which is also a crucial signature to identify the ongoing Mott transition. As a result, the semi-logarithmic plot of spectral behaviour shows the high energy spectral tail like a straight line, as shown in reference 78. Moreover, there are arguments on whether the excitonic Mott transition is a gradual⁸⁰ or a sudden phase transition. There are different views on this matter, and we will discuss the signature of gradual excitonic Mott transition shortly in our electrical and optical experimental data.

3.4 Background physics of frequency-dependent impedance

Usually, excitons have very small binding energy, in the order of few meV for III-V semiconductors. Excitons can be generated by optical frequencies ranging from visible to infrared whereas the intra-excitonic transitions can only be probed by Terahertz (THz) frequency. However, excitons probed in this present work are not optically generated. Here, we create excitons by electrically injecting electrons and holes in the narrow quantum wells region of the device. When electrons and holes come closer, then they feel the Coulomb attractions and form excitons within the active regions of these light emitting devices. Here, we will discuss how applied bias dependent exciton formation and subsequent dissociation of the same happen in forward bias regimes. We will further elaborate on how trapping and emission of charge carriers by defect states and formation of excitonic bound states with forward bias can be distinguished with frequency-dependent impedance measurement. Instead of standard temperature activation of such rate limited injection and recombination processes, here, we see transition rates which are governed by the applied voltage at constant temperatures. This bias activated electrical responses were modelled with a phenomenological rate equation which matches well with our experimental data.

Correlation between voltage modulated electroluminescence (VMEL) and electrical properties of GaInP/AlGaInP based MQW lasers have been demonstrated earlier by Bansal et al.⁸¹⁻⁸³. Under low-frequency modulation, the mutual non-exclusivity of radiative and non-radiative transitions was shown. This originates when slowly responding (\sim ms) sub-bandgap electronic states can directly influence faster (\sim ps-ns) radiative recombination in a non-trivial fashion which necessitates $\frac{1}{\tau_{Effective}} \neq \frac{1}{\tau_{Non-radiative}} + \frac{1}{\tau_{Radiative}}$, where $\tau_{Effective}$ is the effective time constant for such events. For any applied modulation frequency (f) at a temperature (T), charge carriers from certain sub-bandgap channels with activation energy can also contribute⁸¹ to the total available charge carrier reservoir at the junction. This affects both junction capacitance (C) and modulated electroluminescence (VMEL) simultaneously. To fully understand the role of sub-bandgap states, Fermi levels, and electronic transition rates $R = \frac{1}{\tau} = f = v \exp\left(-\frac{E_{Th}}{k_B T}\right)$, we suggest readers to see the band diagram given in figure 3 of Ref. 81. Here, E_{Th} is the thermal activation energy, v is the thermal prefactor representing the heat bath, T is the temperature in Kelvin, τ is the time period of the transition, and k_B is the Boltzmann constant. This band diagram was further used⁸³ to explain the observed anomalous

temperature dependence of VMEL and negative capacitance. In this work, we extend these results to electrically probe the presence of excitons during electroluminescence (EL).

When the quasi-Fermi level crosses activation energy (E_{Th}) of any charge transfer process, one observes a maximum in $G/2\pi f$ (G =conductance) and an inflection point in capacitance (C) in both frequency and temperature domains. Such a resonant conductance activation in frequency domain alters the dielectric environment, which can be probed by impedance spectroscopy. To fully appreciate the above statements, we recommend the readers to consult figure 1 in section 2 of Ref. 66 and discussions around equations 2.6 and 2.8. At low frequencies, the displacement vector within the active junction can follow the applied electric field modulation. However, at high frequency, dipoles cannot respond fast enough to applied modulation. As a result, energy loss through conductance activation is maximum at some intermediate frequencies where dipolar environments respond resonantly. This constitutes a general understanding of any dielectric response measurement. We, however, emphasize that such understanding is in no way dependent on depletion approximation which is mainly used for semiconductor junctions under reverse bias.

Here, we will explore similar physics using a derivative-based approach. We measure capacitance versus frequency data and plot $f dc/df$ with f . The peak signature in these kinds of plots points towards conductance activation and the frequency (f_{Max}) at which peak maximum occurs, corresponds the maximum response of the system. The corresponding carrier density $N(E_{Th})$ which contribute to the impedance measurement and radiative recombination is given by a generalized equation^{84,85},

$$N(E_{Th}) \approx - \left(\frac{f dc}{df} \right) \frac{U}{k_B T} \frac{1}{qw} \quad (3.2)$$

where U is the effective built-in-potential and is linearly related to the applied bias V_{dc} such that $U = [\Phi_B - V_{dc}]$ and Φ_B is the built-in potential at zero bias, q is the electronic charge, w is the width of the junction. In the case of impedance spectroscopy, usual thermal activation energy is obtained from the slope of an Arrhenius plot of $\ln(f_{Max})$ with $1000/T$. However, in this work, we are particularly interested in exploring the frequency response of electrical impedance as activated by increasing voltage bias V_{dc} in the active region of these light emitting diodes at constant temperatures. The estimated $f dc/df$ plays a role similar to electric modulus in such dielectric measurements. Such a description using electric modulus often removes unwanted artefacts from the analysis of dielectric response measurements. Moreover,

we will neither use the above equation 3.2 in its entirety nor the standard $1/C^2$ vs. V plots to estimate carrier densities, both of which require the strict implementation of depletion approximation. Currently, the above proportionality of dipolar density with estimated $f dc/df$ values are used only as a qualitative measure. Any dissipative process also causes decay. Hence, the width of such $f dc/df$ based conductance activation peaks in frequency domain is always related⁶⁶ to exponential decay rates of such dissipative processes in time domain.

3.5 Instrumentation and description of samples

For the steady-state, small-signal capacitance measurement, we used Agilent's precision LCR Meter E4980A at $f \leq 2\text{MHz}$ using 30mV rms voltage modulation. Measured capacitance depends on the small-signal current which is in quadrature with the applied voltage modulation. This capacitance is estimated⁸¹ using a simple, equivalent parallel RC circuit for the laser diode under forward bias. The applied dc bias voltage (current) to the device is represented as V_{dc} (I_{dc}) and monitored by the LCR meter. For temperature variation and control, we used a CS-204S-DMX-20 closed-cycle cryostat from Advance Research Systems along with the Lakeshore Model-340 temperature controller at an accuracy of $\pm 0.1\text{K}$. We measured standard EL spectra using FDS010 Si detector and SR850 Lock-in amplifier. The experimental set-ups for all these optical and electrical measurements are shown and discussed in chapter 2.

The samples used in these experiments are - (i) GaInP/AlGaInP based strained multi-quantum well (MQW) edge-emitting laser diodes from Sanyo (DL 3148-025), and (ii) InGaAs/GaAs based quantum dot (QD) laser diode grown by Molecular Beam Epitaxy (MBE) on (311B) GaAs substrates. A $0.7\mu\text{m}$ -thick GaAs buffer layer was grown before deposition of $\text{In}_{0.5}\text{Ga}_{0.5}\text{As}$ strained quantum dots at $450\text{ }^\circ\text{C}$ which are embedded in the center of a GaAs QW surrounded by $\text{Al}_{0.6}\text{Ga}_{0.4}\text{As}$ cladding layers on both sides (further details can be found in reference 86). These dots have an average diameter of around 26 nm and height 1 nm. Light is emitted through a small mesa etched on its top surface.

To derive the $f dC/df$, experimentally measured frequency-dependent capacitance data were numerically differentiated and multiplied by the frequency itself. Savitzky-Golay signal processing algorithm using Origin8.5 was employed to smoothen out numerically estimated $f dC/df$ vs. f plots.

3.6 Results and discussion

3.6.1 Differential capacitance response, negative activation energy, and excitons

In figures 3.3(a) and 3.3(b), we plot the capacitance versus frequency for two different, forward bias regimes at room temperature for GaInP/AlGaInP MQW laser diode. We observe a systematic evolution of frequency-dependent behaviour of capacitance over the bias regimes. The inflection region in the capacitance versus frequency data bears some interesting physics. Now, in figures 3.4(a) and 3.4(b), we plot the variation of $f dC/df$ with frequency for similar bias ranges. In these figures, we observe very nice peak-like features and these peak frequencies (f_{Max}) in the $f dC/df$ data vary with applied bias voltage. Estimated f_{Max} values initially decrease when forward bias (V_{dc}) slowly increases from zero, as shown in figure 3.4(c).

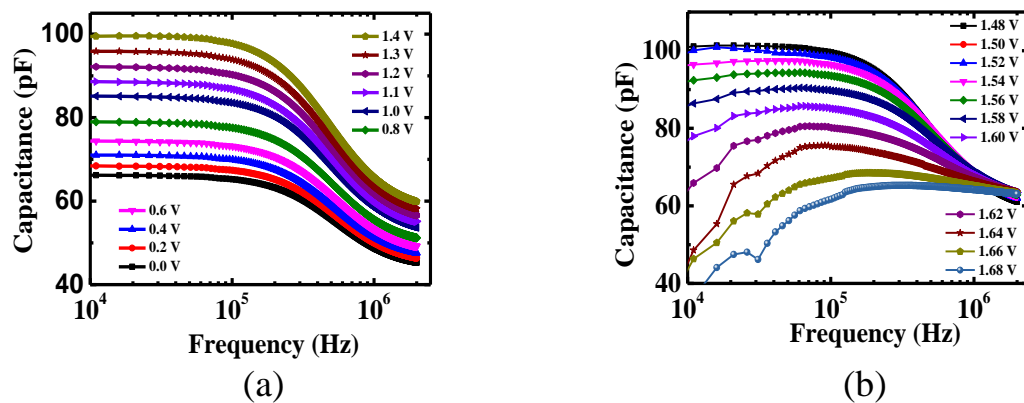


Figure 3.3: (a) Capacitance vs. frequency is measured for lower applied forward bias regime for MQW laser diode at room temperature. The overall magnitude of the capacitance increases with the bias. After certain modulation frequency, capacitance falls and shows an inflection region in the data. (b) Interestingly, the behaviour changes drastically as the applied bias is increased beyond certain value (say~1.45 V). In this intermediate bias regime, the magnitude of capacitance decreases as the voltage is increased and also the inflection region vanishes slowly with bias.

We must emphasize that observations of similar dynamical behaviour of small-signal impedance response are also noticed earlier in non-light emitting Silicon diodes⁸⁷. We have mentioned that defect response can be seen in capacitance measurements when modulation frequency (f) range matches with the transition rate (R). Here, one usually expects that a decrease in temperature decreases the peak position of frequency response (f_{Max}) and increases

the overall amplitude of fdC/df peaks. Therefore, the observed phenomenological activation rate process shown in figure 3.4(c), with increasing V_{dc} , is analogous to usual variations of fdC/df vs $1000/T$ encountered in ordinary impedance spectroscopy. In this regime of applied biases, electronic defect mediated transitions determine the dynamic response of the active junction. We observe the corresponding trend of $\ln(f_{Max})$ vs voltage plot in figure 3.4(c). This is seemingly a well-known voltage-activated defects response in this low applied bias regime⁸⁷. Empirically, this indicates that the role of V_{dc} is qualitatively equivalent to $1000/T$.

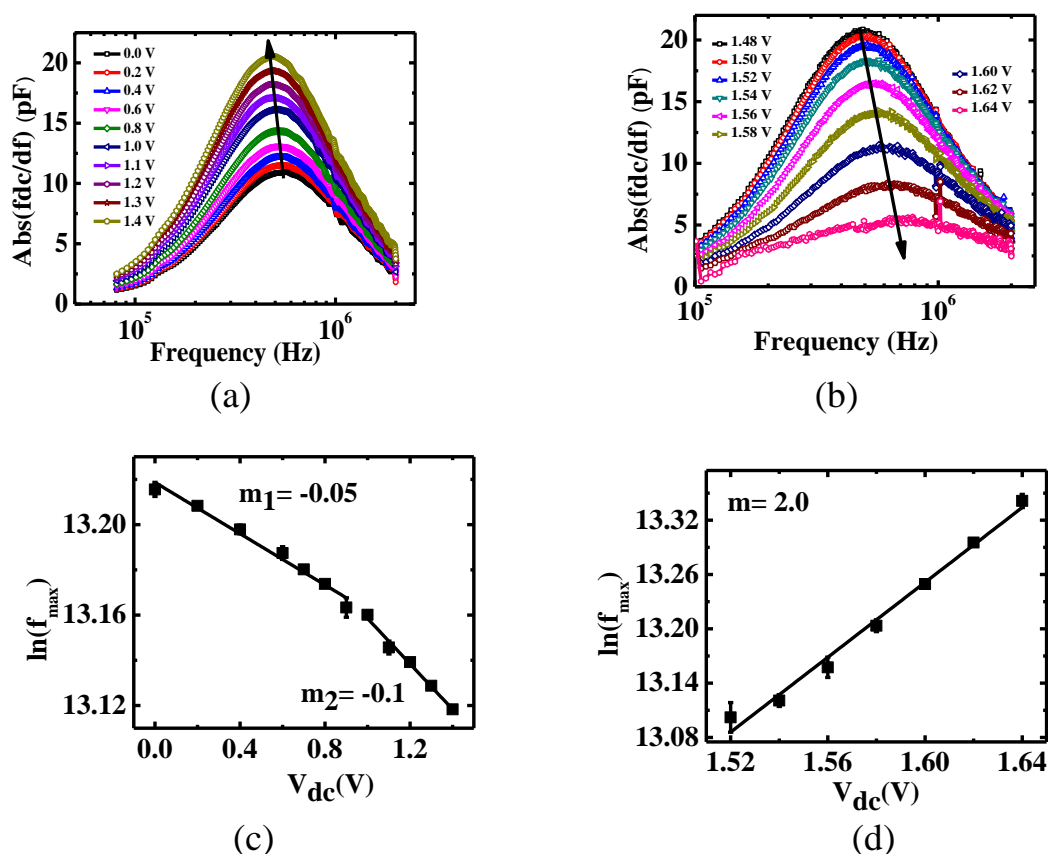


Figure 3.4: Applied voltage-dependent $abs(fdC/df)$ is plotted against frequency for (a) lower forward bias regime and (b) intermediate bias regime. Comparing these two plots, we observe a opposite behavioural signature where in the first plot, peak maxima of the $abs(fdC/df)$ moves towards lower frequency side and the magnitude goes up with the bias, in the second plot, we find that the peak maximum shift to higher frequency side and the amplitude decreases as bias increases. In figures (c) and (d), we plot the $\ln(f_{Max})$ vs. voltage for two different bias regime from figures (a) and (b), respectively. The linear features in the plots certainly follow the voltage-dependent revised phenomenological rate equation of Arrhenius. The slope of the linear fittings changes its magnitude and sign depending upon the bias regime from negative to positive in (c) and (d), respectively.

In general, quasi-Fermi levels in the active junction of a diode, which are nothing but chemical potentials, will be influenced heavily by a large number of injected carriers as a result of forward bias. Moreover, thermally activated carriers also add up in the total carriers available in the conduction and valence band and thus affect the quasi-Fermi levels. Therefore, a simplistic microscopic explanation of the above-mentioned equivalence can be understood in the following way. Within our experimental parameter ranges, as we increase the forward bias (V_{dc}), quasi Fermi levels move towards band edges while with increasing temperature (T) Fermi levels rather move towards the mid-gap in these laser diodes. At this stage, we are certainly ignoring any material-specific Fermi level pinning by defects, in order to build a simplified framework of such voltage-activated processes.

With this above understanding, we conceive a revised phenomenological rate equation for bias activated electronic transitions rate R^* at a constant temperature as,

$$R^* \approx \frac{1}{\tau} = v^* \exp\left(-\frac{E_a}{k_B} \eta V_{dc}\right) \quad (3.3)$$

where η is a proportionality factor in units of $V^{-1}K^{-1}$ to ensure correct dimensionality and E_a is activation energy for transitions activated by the bias voltage. Rewriting this equation gives,

$$\ln R^* = \left(-\frac{E_a}{k_B} \eta\right) V_{dc} + \ln v^* \quad (3.4)$$

The estimated (f_{Max}) coincides with the position of maximum transition rate R^* in the frequency domain. Hence, plotting $\ln(f_{Max})$ with V_{dc} should give a straight line with slope (m) as

$$m = \left(\frac{-E_a}{k_B} \eta\right) \quad (3.5)$$

In case of standard, thermally activated Arrhenius like rate process, v^* represents the attempt-to-escape frequency related to a thermal bath. Its interpretation broadly remains the same in the current analysis. Saturation of defect levels is also at its minimum at $V_{dc} = 0$ and this $V_{dc} \rightarrow 0$ limit points to largest f_{Max} possible for such voltage-activated transitions under forward biasing conditions. $\ln(f_{Max})$ vs V_{dc} plot shown in figure 3.4(c) indeed fits nicely to straight lines in support of the above phenomenological rate equation 3.4. Initial slope (m_1) is -0.05 for very low forward biases, and it abruptly increases to $m_2 = -0.1$ after ~1.1 V. This slope change around 1.1 V is related with considerable changes in carrier dynamics due to the onset of significant injection currents as shown in figure 3.5. The intercept of such plots are usually

related to the entropic changes (ΔS) associated with the injection process following the standard transition rate

$$R = \frac{1}{\tau} = \nu \exp\left(-\frac{\Delta F}{k_B T}\right) = \nu \exp\left(\frac{\Delta S}{k_B}\right) \exp\left(-\frac{\Delta H}{k_B T}\right) \quad (3.6)$$

where a change in free energy is $\Delta F = \Delta H - T\Delta S$; $\Delta H \approx E_a$, ΔH being changed in enthalpy. Therefore, the above parameter η here can also be related to free energy change under voltage activations. The observed change in slope around 1.1 V is connected with corresponding increases in the intercept and thereby an enhanced ΔS during an electronic transition. This enhancement in ΔS for $V_{dc} > 1.1$ V possibly happens due to the increased number of possible microstates of charge carriers after significant injection around 1.1 V as shown in figure 3.5.

In figure 3.4(b), we observe an interesting differential capacitive response, in the intermediate bias regime ($\sim V_{dc} = 1.5$ V to < 2 V), below lasing threshold (~ 2.2 V, ~ 20 mA). Here, the peak frequencies of fdC/df shift toward higher f and the magnitude of fdC/df fall with increasing V_{dc} . Now, in figure 3.4(d), the resultant Arrhenius like plot of $\ln(f_{Max})$ with V_{dc} now shows a seemingly counterintuitive positive slope ($m \sim 2.0$) for a reasonably linear fit in comparison to figure 3.4(c). According to equation 3.5, a positive slope indicates the presence of ‘negative activation energy’ for bias activated rate processes at $V_{dc} \sim 1.5$ V and above. Therefore, around these intermediate injection levels, we observe an exact opposite dynamical behaviour of bias activation than what was seen in case of lower injection levels [figure 3.4(a)]. To understand this opposite impedance response in the intermediate range of bias, we measured EL signal over similar bias range. In figure 3.5, we plot measurable EL signal with the voltage and try to correlate with impedance data. We find that the onset of light emission also starts around 1.5 V.

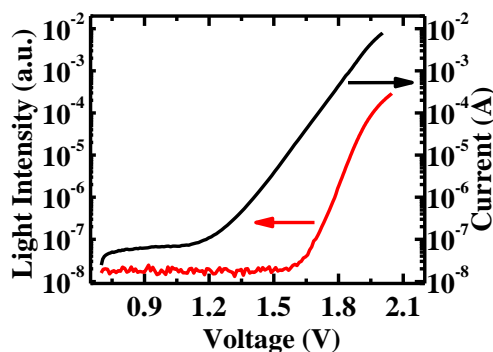


Figure 3.5: Current and EL light intensity is measured for applied forward bias at room temperature.

At this point, we speculate that light emission from this device may have some impact on the observed inverse trend of the slope in $\ln(f_{Max})$ vs. V_{dc} plot in figure 3.4(d).

In general, activation energy is known as a free energy barrier. It is mostly understood as a one-step thermodynamical transition process. However, there are well-known situations in physical chemistry where certain reaction rates decrease with increasing temperatures which cannot be explained by a single step crossing of the activation energy barrier. This quintessential effective ‘negative activation energy’ can, therefore, be explained⁶⁷⁻⁷⁰ only by a two-step configurational process through a stable ‘transitional bound state’ such that low energy initial states can make transitions to final states at a much faster rate than high energy initial states. The net effective activation energy for the whole transition is given by Tolman’s interpretation,

$$E_a = \langle E_{TS} \rangle - \langle E_R \rangle \quad (3.7)$$

where $\langle E_{TS} \rangle$ is the average thermodynamical energy of a ‘stable’ population of transitional bound states measured using steady-state electrical responses. $\langle E_R \rangle$ is the average energy of the initial states which is typically proportional to the energy of the thermal bath ($\sim k_B T$) of injected carriers. Now, if the first term in equation 3.7 is smaller than the second term, then one can get resultant activation energy which is negative. It is certainly tempting to associate this transitional bound state with the formation of excitons having an average binding energy $\langle E_{TS} \rangle$. Subsequently, it undergoes radiative recombination and disappears as shown in figure 3.6(a). This situation is characteristically different from the thermal dissociation of excitons into electron and holes which are usually probed using thermal quenching of luminescence.

For better understanding, we now discuss the microscopic context of the configurational free energy diagram of this composite transition processes shown in figure 3.6(a). Initially, trapped charge carriers have an average thermal energy $\langle E_R \rangle \sim k_B T$ available to them at one particular temperature (T). In general, these carriers have to cross the initial activation energy barrier E_1 and then directly take part in light emission. This E_1 can be a Coulomb barrier which takes care of mutual repulsion of similarly charged carriers before these can populate the narrow active region of quantum well. However, with increasing injections, quasi-Fermi levels move closer to the band edges. Some of these electrons-holes can now first populate this thermodynamical transition state (indicted as an excitonic state) as they experience the strong Coulomb attractions within the narrow confinement of a quantum well. This configurational bound state also has a free energy barrier $\langle E_{TS} \rangle$ beyond which it finally takes part in the

radiative recombination. We understand that the thermodynamic microstates contributing to impedance spectroscopy are characteristically different before and after the formation of excitons. This situation changes again after the recombination of excitons. Corresponding free energy changes are reflected in the configurational free energy diagram in figure 3.6(a). This type of free energy diagram can ensure that the necessary condition⁷⁰ $E_{-1} > E_1 + E_2$ is satisfied to have an effective ‘negative activation energy’ for the overall transition process (see discussions around equation 11 in Ref. 70 for a lucid schematic description of ‘negative activation energy’ process and its connection to our configurational free energy diagram in line with other pioneering papers^{67,68,70}).

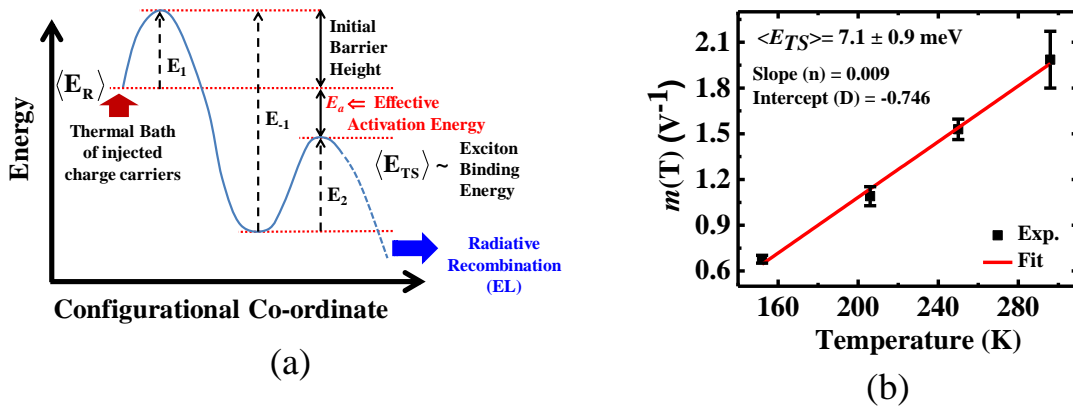


Figure 3.6: (a) A schematic configurational coordinate diagram to understand the negative activation energy and its involvement with excitonic presence in the system. (b) Temperature-dependent change in positive slopes (figure 3.4(d)) is plotted to estimate the excitonic binding energy.

Now, to get a quantitative estimate of the energy value $\langle E_{TS} \rangle$, related to such excitonic presence around these intermediate injection levels, we combine equations 3.5 and 3.7 to get

$$E_a = -m \frac{k_B}{\eta} = \langle E_{TS} \rangle - \langle E_R \rangle \quad (3.8)$$

Here, we replace $\langle E_R \rangle$ by energy $\sim k_B T$ of the thermal bath and by rearranging terms we get

$$m(T) = -\frac{E_{TS}\eta}{k_B} + \eta T = D + nT \quad (3.9)$$

From this equation 3.9, we find that the slope $m(T)$ has explicit temperature dependence. This also suggests that $m(T)$ vs T plot will produce a straight line having ‘D’ is the new intercept and ‘n’ is the new slope. Now, fitting a straight line to the data shown in figure 3.6(b), we

obtain the value of η from the new slope ‘n’ and then estimate $\langle E_{TS} \rangle$ from the intercept ‘D’. Here, we also assume that both η and $\langle E_{TS} \rangle$ do not vary much⁸⁸ within this range of temperature such that $\frac{\Delta\langle E_{TS} \rangle}{\langle E_{TS} \rangle} \ll 1$ even when bandgap of the material may actually change considerably. Finally, our estimated value of $\langle E_{TS} \rangle$ is $\sim 7.1 \pm 0.9$ meV. This value closely matches with the binding energy of the weakly confined excitons in these MQW laser diodes^{89,90}. Therefore, we connect this occurrence of an effective ‘negative activation energy’ to the presence of a stable, steady-state population of ‘excitonic bound states’. We further highlight that contribution of defects and excitons in fdC/df measurements can simply be differentiated by looking at figures. 3.4(a) and 3.4(b) for GaInP/AlGaInP MQW laser diodes. An ordinary defect related transition gives rise to usual negative slopes in Arrhenius like plots as evident from figure 3.4(c). However, situation changes completely [figure 3.4(d)] around 1.5 V in case of GaInP/AlGaInP laser diode. We emphasize that this can only be interpreted in terms of influences of steady-state presence of ‘intermediate bound states’ identified as excitons from these capacitive measurements.

Additionally, we also want to mention that excitonic binding energies are typically less than ten meV in this quantum-confined III-V semiconductor structures with high potential energy barriers. Still, it is possible to see resonant excitonic⁹¹⁻⁹³ effects at room temperature ($k_B T \sim 26$ meV). Unlike bulk material, these barriers oppose the spatial separation of electrons and holes along the confinement direction. Additionally, inherent random fluctuations of the potential barrier due to the uneven well thickness and alloy disorder present across the well interface may also localize these injected electrons-holes in each other’s vicinity. As a result, electrons-holes experience each other’s Coulomb attractions and subsequently form excitons at room temperature⁹². Thus, under high rate of excitation (larger than the rate of radiative recombination), these structures can exhibit a steady-state population of resonant excitons at room temperature, even though the excitonic lifetime is very short (\sim ps). Strong quantum confinement also squeezes the excitonic wave function along the confinement direction to alter the excitonic binding energy to some extent.

3.6.2 Electrical signature of excitonic Mott transition

Moreover, in figure 3.4(b), we observe that the magnitude of fdC/df peak gradually diminish beyond ~ 1.5 V and virtually disappear above ~ 1.7 V. Now, this magnitude of fdC/df

is related to excitons number density (equation 3.2) in this intermediate bias regime. So, the diminishing of fdC/df magnitude corresponds to decreasing of excitons density which is likely connected with excitonic Mott transition. To understand the excitonic Mott transition, we use the Debye-Huckel model of electrostatic screening. Here, we assume that a non-degenerate population of electron-hole gas, formed after Mott transition, obeys classical Boltzmann statistics. To estimate the Mott transition density, the Debye-Huckel model of electrostatic screening⁷² has the form of

$$n_{Mott} = (1.19)^2 \frac{\epsilon\epsilon_0 k_B T}{e^2 a_B^2} \quad (3.10)$$

where $\epsilon (= 11.8)$ and ϵ_0 are static dielectric constants of GaInP and free space, respectively, k_B is the Boltzmann constant and T is the temperature in Kelvin. We calculate the Bohr exciton radius (a_B) ~ 8.3 nm from the previously estimated excitonic binding energy value ~ 7.1 meV. Our calculations yield a value of excitonic Mott density $n_{Mott} = 3.5 \times 10^{17}/cm^3$ at room temperature which somewhat matches with previously reported Mott density for this kind of 2d heterostructures.⁷⁸

3.6.3 Comparison of excitonic physics at room temperature and low temperature

I. Differential capacitance response on similar injection current

Excitonic presence is more prominent at low temperature. To further establish our differential capacitance approach and its correspondence to excitons, we did low temperature measurement as shown in figures 3.7(a) and 3.7(b). We compared fdC/df vs. f plots at both 294 K and 7.7 K, respectively, under partly similar range of applied injection currents. However, unlike figure 3.4(c), we do not observe the usual negative slopes of $\ln(f_{Max})$ vs V_{dc} plots for any bias levels at 7.7 K. This indicates that the origin of negative slopes in $\ln(f_{Max})$ vs V_{dc} plots are related to usual trapping and emission processes from electronic defects which are probably frozen out at such low temperatures. Whereas, the positive slope certainly related to the presence of excitons in the system. Moreover, we qualitatively assume that peak magnitude of fdC/df , in the ‘negative activation energy’ regime, scales with the number of excitons present within the active junction. We further notice that peak fdC/df values at 7.7 K do not decrease with increasing bias currents unlike those at 294 K. This possibly signifies

a lack of ionization of excitons at such low temperature as will also be explained in the next section using results of figure 3.8. We also notice that the fdC/df peak magnitudes are somewhat smaller (~ 12 pF) at lower temperature of 7.7 K as compared to ~ 16 pF at 294 K for a similar injection current (e.g. ~ 1.15 μA).

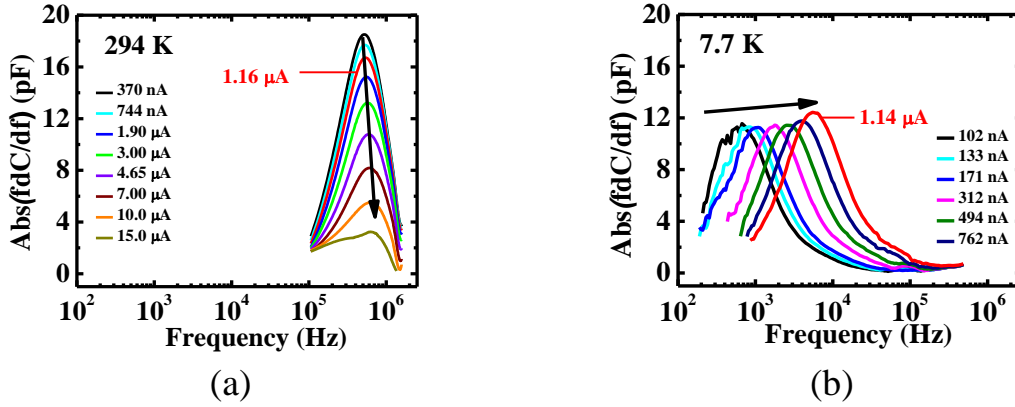


Figure 3.7: (a) and (b) differential capacitance response is plotted for similar injection current regime for both 294 K and 7.7 K, respectively. At the similar current injection (~ 1.15 μA , marked in red), the magnitude of $\text{abs}(fdC/df)$ is less for lower temperature in comparison to 294 K, implying the higher recombination probability drain out more excitonic dipoles at 7.7 K. The black arrows point out the frequency maxima move towards higher frequency side which signifies the presence of the positive slope or negative activation energy.

At one particular injection current, we infuse an approximately similar number of electrons and holes in the active region. However, the radiative recombination of the excitons is significantly stronger at a lower temperature. This stronger EL readily depletes the number of available dipolar excitons which contribute to steady-state dielectric measurements. Therefore, it explains the observed reduction in fdC/df peak magnitude at 7.7 K. Under similar current injections, these bias activated conductance peaks represented by fdC/df also shift toward lower frequencies at lower temperatures as expected from our rate equation model.

II. Photon flux and excitons

In addition to these electrical studies on excitons and excitonic Mott transition, we did some standard opto-electrical studies both at room temperature as well as lower temperatures to reaffirm our claims on excitons. We measured standard EL spectra under similar levels of

looking shape of EL spectra become more prominent. Besides, the EL spectral peak energy also redshift with the bias. On the other hand, at 7.9 K, we observe exciton like sharp resonant, symmetric spectra [figure 3.9(b)]. Although EL emission starts around 1.5 V [figure 3.5] but peak energies and line widths (FWHM) of EL given in figure 3.9(c) are estimated only from experimentally measurable well-shaped spectra of figure 3.9(a) for bias values ≥ 1.75 V. However, more and more exponentially looking high energy spectral tails indicate the ongoing Mott transition process at room temperature following the report by Deveaud et al.⁷⁸ We also find this transition process as gradual^{94,80} due to slowly increasing fraction of free electrons and holes. In fact, these higher energies EL tails become prominently exponential only after 0.8 mA, 1.86 V. Most interestingly, measured electrical signatures of the excitonic bound state tend to slowly disappear by ~ 1.7 V as shown in figure 3.4(b).

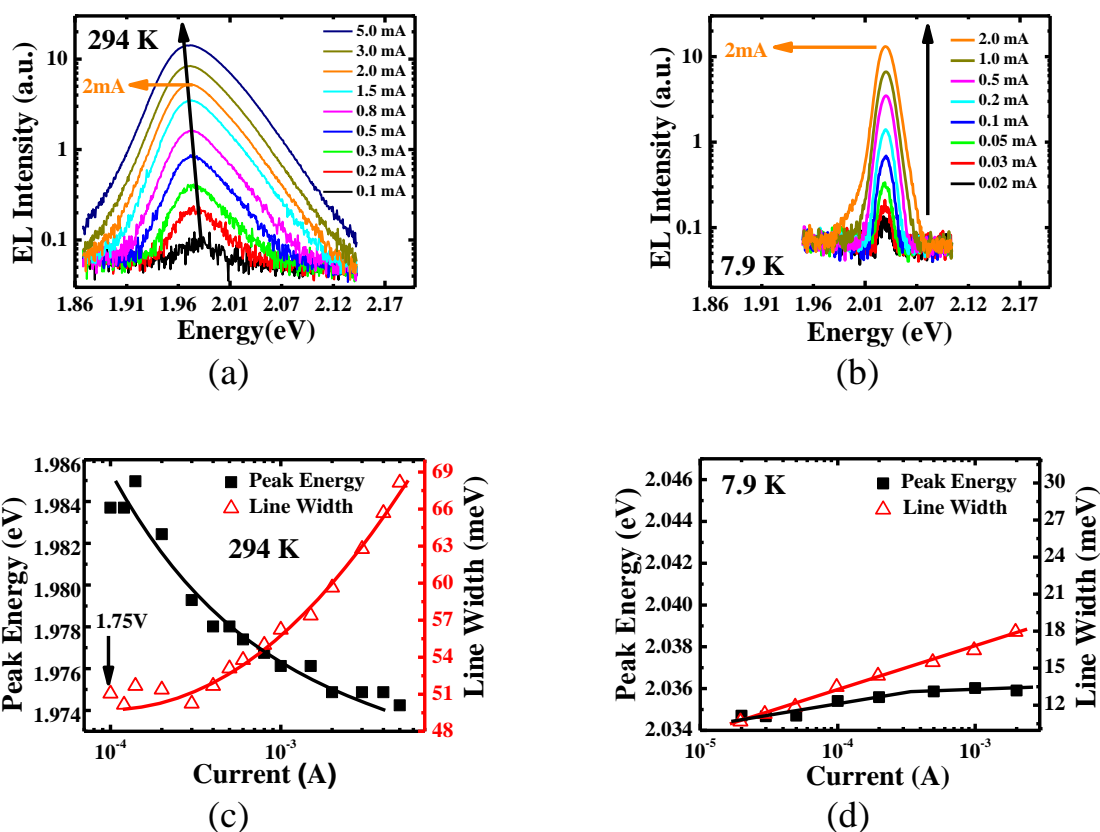


Figure 3.9: Semi-logarithmic plot of EL spectra for different injection current (a) at 294 K and (b) at 7.9 K. In figures (c) and (d), we plot the spectral linewidth and peak energy for different injection current at temperature 294 K and 7.9 K, respectively.

Therefore, this continuing suppression of electrical signature of excitonic response starting after ~ 1.7 V, is likely connected to optical evidence of gradual excitonic Mott transition at

room temperature. In figures 3.9(c) and 3.9(d), we have compared EL peak energies and line widths at 294 K to those at 7.9 K. Significant redshift in peak energies with current injection points towards ongoing bandgap renormalization effects at 294 K. Additionally, due to enhanced scatterings, spectral line widths also increase significantly at higher temperatures. However, we do not see any considerable changes in peak energy and line width at 7.9 K. Therefore; it implies an apparent lack of evidence of excitonic ionizations even under the similar range of high injection levels at such a low temperature, which is also evident in figures 3.7(b) and 3.8. Observed minor blue shifts at 7.9 K are significantly smaller than even the excitonic binding energy. Besides, we also do not see any saturation of EL spectra in such bias ranges at these temperatures to claim any notable phase-space filling effects. All these spectral evidence again support the presence of Mott transition at room temperature.

Estimated line widths (FWHM $\sim\Delta$) from the EL spectra at 294 K are used to calculate the approximate number of electron-hole pair density (n_0) in this quasi-2D sample. The following expressions¹⁹ under zero Kelvin limit for free-electron system is used to calculate the same.

$$n_0 = n_{e,h} = \frac{\nu_{C,V}(2m_{e,h}^*F_{e,h})^{1.5}}{3\pi^2\hbar^3} \quad (3.11)$$

$$F_{e,h} = (2\Delta) \left[1 + \left(\frac{\nu_{C,V}}{\nu_{V,C}} \right) \frac{m_{e,h}^*}{m_{h,e}^*} \right]^{-1} \quad (3.12)$$

where $n_{e,h}$ is the electron or hole density, $\nu_{C,V}$ is the number of equivalent minima or maxima of the conduction or valence band, respectively, with $\nu_{C,V} \sim 1$ for the Γ point in strained GaInP band structure, $m_{e,h}^*$ is the effective mass of electron and hole such that $m_e^* = 0.088m_0$ and $m_{hh}^* = 0.7m_0$ respectively, m_0 is the free electron mass and $F_{e,h}$ is the quasi-Fermi energy level position of electron or hole measured with respect to mid-gap such that $2\Delta = F_e + F_h$ is full width at the base of each EL spectrum. When we increase bias current from 120 μ A to 5mA, corresponding values of Δ vary from ~ 50.2 meV to ~ 68.1 meV as seen in figure 3.9(c). As a result, calculated electron-hole pair density changes from $\sim 3.2 \times 10^{18}/cm^3$ to $\sim 5 \times 10^{18}/cm^3$. Therefore, even these zero Kelvin estimates of number density calculated from EL spectroscopy are certainly more than the anticipated Mott transition density of $n_{Mott} = 3.5 \times 10^{17}/cm^3$ derived from electrical fdC/df measurements. This indicates gradual excitonic Mott transition in these quasi-2D GaInP/AlGaInP MQWs at 294 K over such bias ranges.

We must reiterate that vanishing of fdC/df signature mentioned above [figures 3.4(b) and 3.7(a)] also happens in the similar range of forward biases where we also see standard optical spectroscopic signature [figure 3.9(a)] of the excitonic Mott transition. This concurrence of both optical and electrical effects helped us to identify these corresponding changes in fdC/df as those originating from the effect of formation of a steady-state population of excitons and their subsequent disappearance through Mott transition. Capacitance or fdC/df is a measure of the dielectric response of the active junction and it is not surprising that this response can change when neutral excitons dissociate into conducting electron-hole plasma through a Mott transition. Moreover, electronic defects are expected to freeze at such low temperatures of $\sim 7-8$ K. These eventually stop taking part in carrier trapping and emission processes. Defect levels also saturate under such high forward biasing. We, however, we still see ‘negative activation energy’ like signatures of fdC/df even at such low temperatures [figure 3.7(b)].

3.6.4 Prominent electrical signature of excitons in InGaAs/GaAs QDs laser diode

So far, we have dealt with 2-dimensional MQW heterostructures made of AlGaInP/GaInP. Now, we want to reproduce the similar physics in another semiconductor heterostructure to extend the applicability of this frequency-dependent differential capacitance approach towards the exploration of excitonic physics. Here, we probe a zero-dimensional QDs laser structure made of InGaAs/GaAs. Due to having a stronger overlap of electron-hole wave functions, excitonic presence is expected to dominate in these QDs heterostructure. We also find convincing support of all our previous analyses on the electrical signature of excitons in these QD laser diodes. In figure 3.10(a), we observe a similar trend of large fdC/df peaks where f_{Max} moves towards the higher frequency side as the injection current increases. Now, plotting the $\ln(f_{Max})$ vs. V_{dc} , we find the slope of the straight line is positive around 294 K. Positive slopes in $\ln(f_{Max})$ vs. V_{dc} like Arrhenius plots corresponds to ‘negative activation energy’ which again should be related to the presence of excitons.

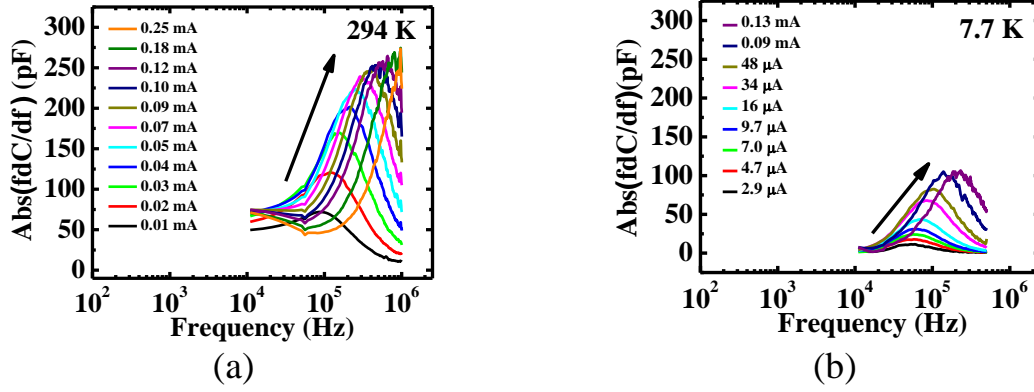


Figure 3.10: (a) and (b) Differential capacitance response is plotted for different injection current for InGaAs/GaAs QDs laser diode at 294 K and 7.7 K, respectively. Scaling of both X and Y axis are kept the same for better comparison. Here, black arrows show the shift of peak frequency maxima towards higher frequency regime with applied current. This trend again confirms the presence of negative activation energy or excitonic states.

Moreover, we observe similar trend in $f dC/df$ vs. current at 7.7 K and in figures 3.10(a) and 3.10(b), we compare both the low temperature and room temperature results. These $f dC/df$ peaks shift towards larger frequencies at both the temperatures. Interestingly, we only see a positive slope in $\ln(f_{Max})$ vs. V_{dc} plots for this QD laser diode under any applied forward bias at both the temperatures. This is understandable as QDs are supposed to be strongly excitonic in nature and even a very small bias can create stable excitonic population displaying ‘negative activation energy’ like behaviour. Importantly, the excitonic binding energy estimated from similar plots of $\ln(f_{Max})$ vs. V_{dc} for different temperatures with positive slopes, is found to be 6.4 ± 0.7 meV, shown in figure 3.11. This agrees well with the reported values^{95,96} for these kinds of QDs structure made of III-V materials. Besides, we find that the relative peak heights of $f dC/df$ reduce much more substantially with lowering of temperature as compared to similar plots of weakly confined quasi-2D GaInP/AlGaInP MQW laser sample given in figures 3.7(a) and 3.7(b). As a result, this much larger variation of $f dC/df$ peak heights can be explained in terms of expectedly higher radiative recombination in QD laser at 7.7 K. Such strong radiative recombination can significantly reduce an available number of excitonic populations that can contribute to steady-state dielectric measurements. In addition, the height of the $f dC/df$ peaks continuously increases with increasing bias currents (unlike MQW sample) indicating that the dipolar excitonic population measured by our differential capacitive method is also increasing with increasing injections.

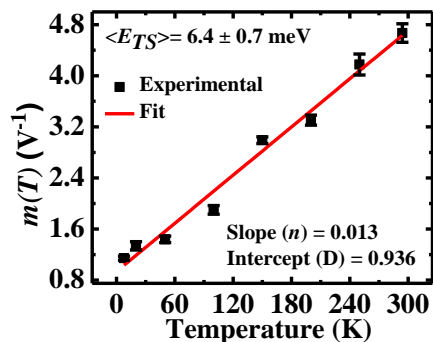


Figure 3.11: Temperature-dependent positive slopes of $\ln(f_{Max})$ vs V_{dc} graphs are plotted and fitted with a linear equation. From the linear fitting parameters, the average excitonic binding energy has been estimated which is ~ 6.4 meV.

This signifies absence of any Mott transition in these QD lasers as seen in the MQW lasers. It is anticipated because the influence of Coulomb screening is substantially reduced in lower dimensional systems. Besides, we also note that the frequency span of bias activated fdC/df peaks in InGaAs/GaAs QD laser is comparatively temperature independent as compared to that of GaInP/AlGaInP MQW laser.

Lastly, we perceive that all these results once again affirm our claim on electrical evidence of steady-state excitonic populations at higher injections in quantum confined laser structures using dielectric impedance measurements. As mentioned above, the formation of more excitons with increasing bias, not only shifts the fdC/df peak towards higher frequencies but also enhances its magnitude in this QD sample. This is not expected from any ordinary defect mediated carrier trapping and emission processes as observed in figure 3.4(c). The fdC/df amplitudes also decrease significantly at low temperatures where enhanced radiative recombination irreversibly remove a large number of excitons from the active junction.

3.7 Conclusions

To summarize, we have developed a novel electrical technique to probe the physics of excitons in GaInP/AlGaInP MQW and MBE grown InGaAs/GaAs QD laser diodes. The applied voltage-dependent differential capacitance (fdC/df) measurements with frequency bear the signature of excitons in these quantum confined structures. Presence of excitonic

dipoles at the junctions of these light-emitting diodes, certainly modify the junction capacitance depending upon applied modulation frequency. We conceived a phenomenological rate equation considering the effects of applied bias on the dynamics of various rate-limited processes. Formation of stable excitonic population inverts the usual negative Arrhenius slope to positive one which eventually appears as ‘negative activation energy’. This ‘negative activation energy’ relates to the presence of transitional bound states, excitons. Calculated average energy of this bound transitional state matches well with the binding energy of the weakly confined excitons in both the laser diodes. We emphasize that such occurrence of ‘negative activation energy’ was not observed in ordinary Silicon diodes which do not show electroluminescence and perhaps are non-excitonic in nature.

Further increase in charge injection suppresses the differential capacitive response, which shows a gradual Mott transition of exciton states into electron-hole plasma in GaInP/AlGaInP MQW. This all-electrical, steady-state description of excitonic presence and its subsequent suppression is fully supported by standard optical spectroscopic signatures of excitonic Mott transition. It may lead to innovative applications based on efficient electrical control of excitonic devices. Work is going on to use such a generic approach to fully understand specific analytical details of dipolar contributions of excitons through dielectric measurements.

Moreover, one may apply a similar analysis to investigate the presence of condensed excitonic phases at low temperatures and to other rate-limited transitions involving any bound states/quasiparticles in various materials/device structures intended for advanced functionality including ‘excitonics’. Specifically, there is increasing consensus about the role of dark excitons, in connection with still elusive excitonic BEC. It has been repeatedly advised that standard optical tools, which indirectly study such condensations by looking only at photons coming out once excitonic quasi-particles decay, might actually overlook the BEC altogether. At this point, we speculate that our dielectric experiments dealing with frequency-dependent dynamic signatures of dipolar excitons will be able to throw more light in that direction as these tools will also be sensitive to the presence of the dark excitons.

Chapter 4

Physics of Indirect excitons and excitonic complexes using photocapacitance spectroscopy in GaAs/AlAs/GaAs heterostructure

4.1 Introduction

Semiconductor heterostructures are attractive due to their in-built potentiality to control and manipulate both electrical and optical properties of carriers, including excitons. Moreover, these heterostructures also have shown better efficiency for optoelectronic applications in comparison to their bulk counterparts. Now, we know that presence of excitons in these semiconductor quantum heterostructures are observable even at higher temperatures due to strong quantum confinement of electrons and holes within such structures. Moreover, it is possible to detect excitons at room temperature using any steady-state method when the generation rate is higher than the recombination rate inside a quantum structure^{91,92}. In this chapter, we will mostly address a particular type of indirect excitons, excitonic complexes like trions and Fermi-edge singularities within a single barrier GaAs/AlAs/GaAs heterostructure. Applied bias dependent photocapacitance and photocurrent spectroscopy have been established by us as efficient and sensitive experimental tools to detect these indirect excitonic complexes in single barrier p-i-n devices. We also qualitatively argue at the end, why these electro-optical methods bear more clear-cut experimental proofs of indirect excitons in comparison to PL.

Initially, we will look into the details of energy band diagram of GaAs and AlAs, their energy bandgaps, basic parameters, etc. Later on, we will discuss, how the energy band alignment, band bending and formation of triangular confined regions will happen at the interface of these two interesting materials when they are brought closer to make semiconductor heterostructure devices. First of all, both GaAs and AlAs have an almost similar value of lattice parameters which effectively help to grow good quality, smooth heterointerface between these two materials. Besides, GaAs and AlAs have direct and indirect bandgaps, respectively. In addition, the effective bandgaps of these two materials are such that they form a type I band alignment (see figure 1.5(a) in Chapter 1).

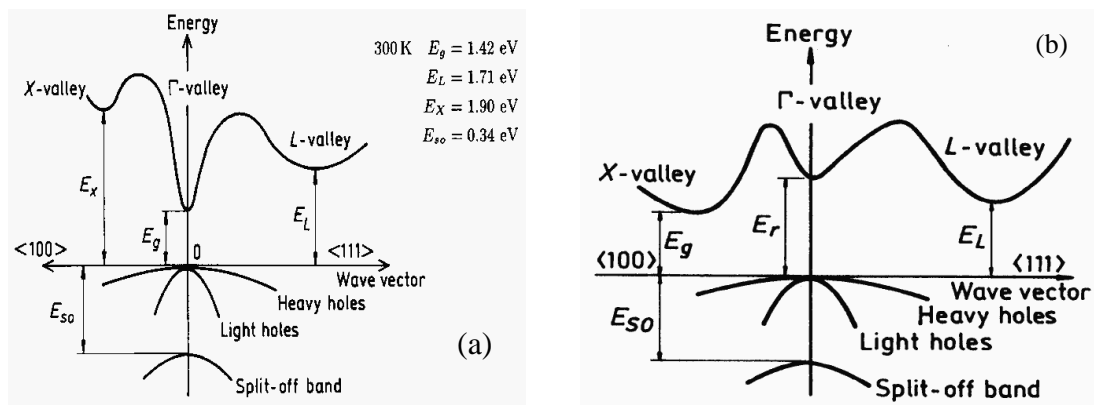


Figure 4.1: (a) and (b) Energy-momentum (E - k) diagram of bulk GaAs and AlAs, respectively. In the schematic representations, effective energy bandgap, different valleys and the valence band splitting are shown for both the materials. These images are taken from the Ioffe online site⁹⁷.

Table 4.1: Basic parameters of GaAs and AlAs are tabulated for experimental analysis.

Parameters	GaAs	AlAs
Structure	Zinc Blende	Zinc Blende
Lattice Constant (\AA)	5.653	5.660
Energy Bandgap (300 K) (Γ valley and X valley)	1.424 (E_g^Γ) 1.90 (E_g^X) ⁹⁷	2.16 (E_g^X) 2.95 (E_g^Γ) ⁹⁸
Energy Bandgap (0 K)	1.519 (E_g^Γ) 1.981 (E_g^X)	2.24 (E_g^X) 3.099 (E_g^Γ) ⁹⁹
Bandgap type	Direct	Indirect
High-frequency or optical Dielectric Constant (ϵ_∞)	10.89	8.16
Static Dielectric Constant (ϵ_s)	13.18	10.06 ⁹⁸
Refractive Index (n)	3.5227	2.99
Effective mass of electron (m_e^*)	0.067 m_0 (m_e^Γ) 1.3 m_0 (m_e^X)	0.15 m_0 (m_e^Γ) (0.4-0.8) m_0 (m_e^X) ⁹⁹
Effective mass of hole (m_h^*)	0.51 m_0	0.5 m_0
Electron mobility ($\text{cm}^2\text{V}^{-1}\text{s}^{-1}$)	8500	200
Optical Phonon energy (meV)	45	35

Also, the effective band offsets of conduction and valence band play a significant role to have quantum confinement region. Now, when a semiconductor p-i-n junction diode is made of with GaAs and AlAs, then an interesting band bending occurs in the intrinsic region. Here, we are mostly interested to a particular single barrier heterostructure made of GaAs/AlAs/GaAs. In figure 4.2(a), we have shown a schematic of the energy band diagram of GaAs/AlAs/GaAs p-i-n under zero or reverse bias condition. Highly doped thick p-type and n-type GaAs materials are used as the top and bottom metallic contacts of the device. A few nanometers (nm) thick GaAs/AlAs/GaAs heteroepitaxial layers are grown in the intrinsic region of the device. Complete details of the layers will be discussed later in the experimental section. Important to note here that the p-type and n-type GaAs are made by doping the intrinsic GaAs materials with Be and Si, respectively.

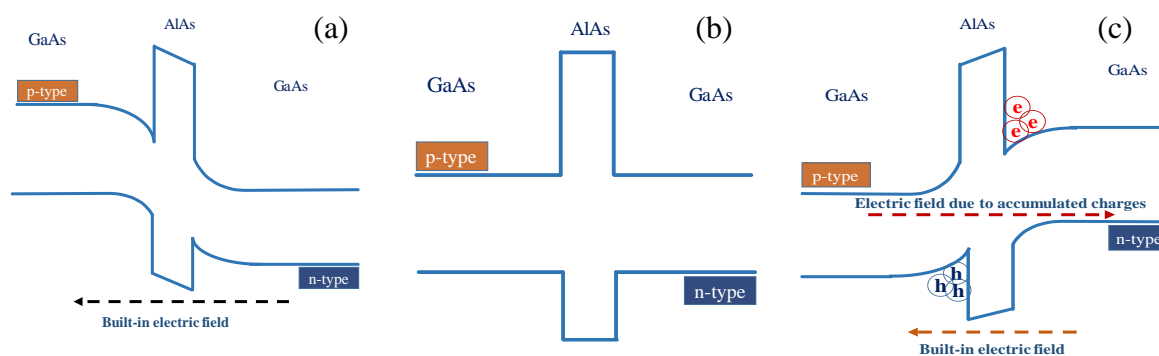


Figure 4.2: (a) A schematic energy band diagram of p-i-n single barrier GaAs/AlAs/GaAs heterostructure under zero bias or reverse bias. We observe that due to the presence of built-in electric field across the intrinsic region there is band bending which forms triangular quantum wells both side of the AlAs barrier. (b) This is a band diagram for the flat-band condition when the external forward applied voltage matches with the built-in internal voltage. Thus, there is effectively no electric field across the junction. (c) Complete opposite and unconventional band bending happens when the applied forward bias become quite high. Due to the presence of a high potential barrier of AlAs, the accumulated carriers (electrons and holes) cannot tunnel very efficiently. Thus, these accumulated charge carriers generate an electric field which is opposite to the built-in electric field (due to immobile ions) as indicated by the arrows. When the electric field due to the accumulated carriers become higher than the built-in field then the band bending follows the trend as shown in (c).

In addition, we observe that due to band bending across the AlAs layer, there is formation of triangular quantum wells (TQWs) both for electrons and holes in their respective regions.

Also, the overall band bending trend of this p-i-n heterojunction is similar to a normal p-n homojunction diode. Now, as the applied forward bias is increased and when the applied voltage reaches to flat-band condition, then accordingly the bands are aligned and become almost flat as shown in a schematic representation in figure 4.2(b). However, it is well known that an unconventional¹⁰⁰⁻¹⁰² band bending follows as the applied forward bias is increased more than the flat-band voltage as shown in figure 4.2(c). Here, it is noticeable that this band bending is entirely different from the standard one in figure 4.2(a). To understand the underlying physics behind this kind of behaviour, we comprehend that there should be an associated electric field across the heterojunction which is exactly opposite in direction and higher in magnitude than the depletion field due to immobile charges. Accordingly, in this kind of heterostructure, the presence of strong potential energy barrier of AIAs does not allow charge carriers to pass through it except small tunnelling possibility. Thus, in this process, there will be an accumulation of electrons and holes in the n and p side, respectively. Now, this accumulated positive and negative charge carriers separated by a small distance produce an electric field which is opposite to the direction of depletion field as shown by the arrows in figure 4.2(c). When the strength of this field due to accumulated charge carriers becomes higher than the depletion field then the former one dominates the energy band structure. As a result, the band bending looks similar to figure 4.2(c)¹⁰⁰⁻¹⁰². In our experimental studies, we will discuss these physics in more details and show how the charge transport properties get affected due to this kind of band bending profiles. We would also like to mention here that although the transport properties of these single barrier structure use the concept of tunnelling, however, we rather discuss the details of tunnel diode in the next chapter 5 due to better relevance of the context.

Here, we find this kind of single barrier heterostructure as very exciting system to probe the physics of indirect excitons. Formation of TQWs on both side of the AIAs barrier allows electrons and holes to accumulate and confine within wells. Now, proximity of electrons and holes in these wells let them to bind via Coulomb attractions to form indirect excitons. Presence of an extra layer of AIAs in between electrons and holes (in GaAs), make them spatially indirect in nature. Thus, these indirect excitons hardly respond to optical emission process (except through tunnelling). Also, being charge-neutral dipoles, excitons cannot conduct direct current unless they are dissociated into electrons and holes by an electric field. Nevertheless, excitons with non-zero dipole moments are expected to respond in capacitance measurements. Previous studies^{103,30} have shown that both photocurrent and capacitance-voltage (C-V) spectroscopy

techniques can be used to detect excitonic features. Labud et. al²⁸ and Pal et. al²⁹ investigated many-body interactions of different excitonic species as well as signatures of indirect excitons in quantum dot samples using standard C-V measurements in the presence of light. In the previous Chapter 3, we also have described a thermodynamic model of dielectric signatures of excitonic presence in quantum well laser diodes at room temperature using capacitance-based measurements. Here, we report on observations of resonant peak signatures of photo-generated, 2D quantum-confined indirect excitons in single barrier GaAs/AlAs/GaAs quantum heterostructure using photocapacitance spectroscopy under different DC-biases and AC modulation frequencies. We discuss why 2D quantum-confined indirect excitons can have thermodynamically finite probabilities to survive even at room temperature. We also describe how these excitonic dipoles are detected using photocapacitance spectroscopy, which has never been used for the detection of indirect excitons. Earlier people had usually created and probed indirect excitons by using external electric fields¹⁰⁴ to pull apart direct excitons which are formed inside coupled quantum wells. Such procedures often broaden the excitonic spectra and thereby compromise the nature of these excitons. In contrast, in this study, applied electric fields are mainly utilized to push electrons and holes towards each other to form spatially separated, indirect excitons across the Γ -AlAs potential barrier. This procedure results in an uncharacteristic sharpening of photocapacitance spectral features of indirect excitons with increasing bias. Before proceeding further to explain experimental results, in the next few sections, we will discuss some basic concept of physics terminology which we will use thoroughly later in this chapter.

4.2 Excitonic dipole moments and electric field

We first note that any pair of positively charged hole and negatively charged electron separated by a distance ‘d’ forms a dipolar entity. Therefore, excitons also possess dipolar properties and, thus have dipole moments. Now, in this section, we will comprehend how these dipolar excitons are affected when the applied electric field is varied. Let us initially consider, there is a permanent dipole, having a dipole moment ‘ \vec{p} ’, is placed in an electric field \vec{F} with an initial angle in between them as θ , shown in figure 4.3. In this configuration, the torque $\vec{\tau} = \vec{p} \times \vec{F}$ will be generated which will act on the dipoles and tend to align the dipoles along the direction of the field. The potential energy of the dipole $U = -\vec{p} \cdot \vec{F}$ will be minimum when the

dipoles are oriented in the field direction and this is the stable, minimum energy configuration for the system.

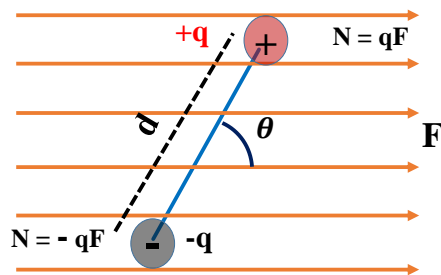


Figure 4.3: A simplified picture describing the interaction of a dipolar system with the electric field (F).

Also, in presence of an external electric field, charge distributions inside the material also contribute to dipole moment which is called induced dipole moment (p^{ind}). This depends on the polarizability (α) of the material. Polarizability of a material is defined as the induced dipole moment per unit electric field or $\alpha = \frac{p^{ind}}{F}$. So, the total dipole moment for a system is the combination of both permanent and induced dipole moments i.e. $p^{total} = p + p^{ind}$. One can derive the effective contribution of these dipole moments to the potential energy of the system following the basic calculation. The total potential energy (U) can be estimated as

$$U = \int dU = - \int \overline{p^{total}} \cdot d\vec{F} \quad (4.1a)$$

$$= - \int (\vec{p} + \vec{p}^{ind}) \cdot d\vec{F} \Rightarrow - \int (\vec{p} + \alpha \vec{F}) \cdot d\vec{F} \quad (4.1b)$$

$$U = U_0 - \vec{p} \cdot \vec{F} - \frac{1}{2} \alpha F^2 \quad (4.1c)$$

where, dU and dF are the elemental change in potential energy and electric field, respectively. U_0 is the potential energy at zero electric field. Now, we would like to introduce the concept of Stark effect in semiconductor system and how it correlates with the above energy expression. In presence of external electric field, energy levels of a system get shifted, which is known as Stark effect. Usually, in a semiconductor system, application of an external electric field changes the absorption and emission spectrum significantly. There are essentially two types of electric field-induced changes in spectral features, one is called the Franz-Keldysh (F-K) effect and the other one is quantum-confined Stark effect (QCSE)^{11,23,105}. The F-K effect

mainly happens in bulk semiconductor system and the presence of electric field modifies the band-edge transition such a way that the resulted spectral peak energy usually shifts towards lower energy with increasing electric fields. Whereas, QCSE mostly appears in quantum confined low-dimensional structures. Here, applied electric field pushes electrons and holes of excitonic bound states in opposite direction inside quantum wells but due to the presence of high potential barriers and deep confinement, they are not fully torn apart²³. So, the electrostatic Coulomb attraction still exists and the exciton still survives. However, the excitonic spectral signatures usually become broaden due to the applied field²³. Also, the ground state energy levels of electrons and holes of the quantum structures are modified with the field. This effectively changes the spectral peak energy of the absorption or emission spectra. Now, these excitonic peak energy shifts in the spectral data with applied electric field can be explained on the basis of how the dipoles of excitons interact with electric field. There are numerous published articles¹⁰⁶⁻¹⁰⁸ where researchers have corroborated the field-dependent spectral energy shift with dipolar energy equation 4.1c as evidence of QCSE. One can also estimate the value of dipole moment and polarizability of a system by fitting experimental data with this quadratic field-dependent equation 4.1c. In our experimental results, we will discuss the details of these estimations and the corresponding values of dipole moments and polarizability for indirect excitons and excitonic complexes.

4.3 Excitonic complexes

As one of the simplest of quasi-particles, exciton requires minimum two oppositely charged particles; electron and hole to form. This number of electron and hole can be more than one, and in that case, more than two particles can form exciton like bound states which are called excitonic complexes. There are two distinct, well-explored states of excitonic complexes: one is known as charged excitons or trion states and another one is called biexcitons¹⁹. Trions are made of three particles: either two electrons and one hole or two holes and one electron. Depending upon the abundance of hole or electron, one is called positively charged trion when there is an extra hole and another one is termed as negatively charged trion when there is an extra electron with the exciton. This is simply can be understood as a neutral exciton with an extra charge; electron or hole, and hence, it is termed as charged exciton state. They are usually denoted as X^+ and X^- for positive trions and negative trions, respectively. Similarly, when two excitons bind together to form a bound state then it is called exciton molecule or biexciton (XX). These trion or biexciton states have very common similarity with

a hydrogen ion (H_2^+ and H^-) or hydrogen molecule (H_2), respectively¹⁰⁹ when hydrogen atom (H) is compared with neutral exciton. Now, the binding energy of these excitonic complexes is quite small as compared to the excitons. As a result, these delicate excitonic complexes are mostly a low-temperature phenomenon for the majority of III-V semiconductor materials. However, binding energy can be enhanced a lot when these complexes are generated inside low-dimensional quantum heterostructure devices. Moreover, recently accessible semiconductor materials like layered transition metal di-chalcogenides (TMDC), black phosphorene¹¹⁰, etc. are shown to be good semiconductor system to probe the physics of these excitonic complexes. Due to less dielectric screening in these materials, the binding energy of excitons and its complexes is much higher, which certainly help to probe the experimental signatures of these states even at room temperature¹¹¹⁻¹¹³. For monolayer MoS₂ and WSe₂, the trion binding energy is reported ~ 20 meV and ~ 30 meV, respectively^{111,114}.

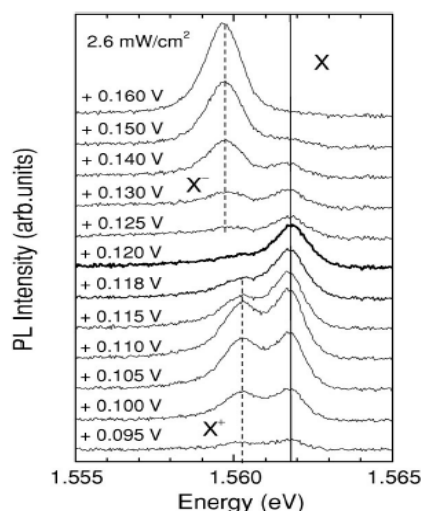


Figure 4.4: This is a plot of PL intensity versus energy at a fixed photoexcitation intensity. Spectral evolution from positive trion to negative trion is demonstrated for different applied biases in *n-i-n* GaAs/AlAs double-barrier diode. (Taken from reference 109).

Depending upon materials, sample structures, and external perturbations, one can identify such positive and negative trions. Like, in monolayer MoS₂, the possibility of negative trion formation is more as MoS₂ is inherently *n*-type in nature¹¹¹. Whereas, tunnel diodes like GaAs/AlAs single, double-barrier structures may contain both positive and negative trions depending upon the polarity of bias, device types, and other factors. We would like to mention here that the estimated binding energy of both X^+ and X^- have similar values¹⁰⁹. Although,

there are substantial divergences in arguments among experimentalists and theorists on this issue. However, there is a claim that due to higher hole effective mass, binding energy of X^+ should be higher in comparison to X^- .¹⁰⁹ Generally, excitons and trions coexist within semiconductors which resulted in observation of two distinct spectral peaks. Now, the binding energy of trions can be simply the energy difference between two spectral peak energies as shown in figure 4.4. However, dissociation of a trion produces a neutral exciton and an extra charge. This extra charge contributes to the adjustment of the Fermi level. Accordingly, we write the expression for trion binding energy ($E_{X^\pm}^b$)^{111,115},

$$E_{X^0} - E_{X^\pm} = E_{X^\pm}^b + E_F \quad (4.2)$$

where, E_{X^0} is the peak energy of neutral exciton, E_{X^\pm} is the peak energy for negative/positive trion and E_F is the Fermi energy due to excess electron/hole. Above equation 4.2 can be used to estimate the binding energy of trion. One can plot the energy difference between trion and exciton peak with the Fermi energy and the intercept of the fitted straight line results in trion binding energy. We will discuss one example of this estimation of trion binding energy in our experimental results.

Similarly, there are numerous reports on biexcitons in different materials systems^{116,117}. Identifying the signature of biexcitons and distinguishing them from excitonic ensemble have been done on the basis of power-law behaviour. As biexcitons are made of two excitons, it is expected that the emission strength due to the biexcitons recombination will be always much higher in comparison to excitonic recombination. In a log-log plot, biexciton emission intensity (I_{XX}) versus exciton intensity (I_X) shows a power-law behaviour $I_{XX} \propto I_X^\alpha$, where, α is the power-law exponent. Theoretically anticipated value of α should be 2, which says each biexciton is a product of two excitons. Whereas, experimentally estimated values of α vary from 1.2 to 1.9 depending on systems¹¹⁶. We also want to mention here that these excitonic complexes involve many-body physics which necessitate considering different interaction terms like correlation term, exchange term etc. using Hartree-Fock (HF) theory^{118,119}. We will not go into the detailed theoretical analysis of these many-body physics in this context. Moreover, all these excitonic complexes occur in a moderate level of carrier density regimes where the interaction strength is sufficient enough to bind these states together. On the other hand, when the density of carriers become much higher then we observe another aspect of excitonic physics which will be discussed in the next section as Fermi-edge singularity.

4.4 Fermi-edge singularity

Spectral characteristics of absorption and emission process of any semiconductor materials highly depend upon the excitation power, carrier density, sample temperature, etc. Depending upon observed variation of spectral peak, line shape, peak energy shifts with changing parameters, the underlying many-body carrier dynamics can be predicted in a semiconductor. Fermi-edge singularity (FES) is a manifestation of a unique excitonic spectral signature in semiconductor structures. This usually happens when a Fermi sea of electrons or holes (2DEG or 2DHG) is strongly Coulomb attracted to a trapped hole in the valence band or an electron in the conduction band or to each other respectively. Thus, this has a similarity to excitons in displaying resonant peak like spectral signatures. This phenomenon is known as the Fermi-edge singularity. The concept of FES was first introduced by Mahan^{120,121} in 1967 while studying the X-ray absorption spectra of metal and interband absorption spectra of semiconductors. Absorption and emission spectra show an abrupt change in a spectral line shape, intensity and peak energy after some threshold carrier density. In a semiconductor quantum heterostructure, in the lower density regime, formation of excitonic bound state happens which show sharp, symmetric spectral peaks. In the moderate density regime, co-existence of both the excitons and low energy trion states were observed in absorption or emission spectra¹²². However, when the density of electrons or holes exceeds some threshold value then the Fermi levels move towards higher energies. Consequently, the optical transition takes place directly at the Fermi levels. Hence, spectral peak signature of FES mostly happens in the higher energy side of the spectrum. Moreover, the spectral shape of FES becomes asymmetric due to strong scattering effect at high carrier density. Now, the obvious question arises regarding the relevance of the term ‘singularity’ in this scenario. At the threshold carrier density, the absorption strength ($A(\omega)$) follows a power-law behaviour which is governed by the following expression¹²².

$$A(\omega) \propto \frac{1}{(\omega - \omega_0)^\alpha} \quad (4.3)$$

where ω is the angular frequency of the light, ω_0 is the resonant transition frequency of the semiconductor and the α is the power-law exponent. α has been understood as a measure of phase shift and screening during strong scattering in this high-density regime. It is now very evident from the equation 4.3 that absorption strength becomes quite high as the incident frequency of light resonantly matches with the transition frequency of the semiconductor. As a result, effective absorption efficiency increases sharply after the onset of FES.

This sudden enhancement of transition probability in the emission or absorption spectra provoked researchers to relate the phenomenon with singularity. One can also correlate this FES nature with well-known concept of Van Hove singularity in condensed matter physics where the density of states (DOS) shows kinks (sharp increase) for different energy values¹²³. Hence, the DOS is not differentiable at those kink points, i.e., derivative of DOS with respect to energy diverges at kink, which implies the singular region. The physics of FES also found to be analogous with the well-established, many-body Kondo effect problem in condensed matter system as reported by researchers^{124,125}.

4.5 Sample details and experimental techniques

All experimental measurements were done on an 8 nm thick single barrier GaAs/AlAs/GaAs p-i-n diode structure. The sample was grown by molecular beam epitaxy on a semi-insulating GaAs (311)A substrate. A 1.5 μm thick, highly doped p-GaAs ($4 \times 10^{18} \text{ cm}^{-3}$) buffer layer was grown first. This layer also served as the p-type bottom electrical contact for the device. Subsequently, a 100 nm thick p-GaAs ($1 \times 10^{17} \text{ cm}^{-3}$), an 8 nm undoped AlAs quantum barrier, two 100 nm undoped GaAs spacer layers on both sides of the AlAs barrier, and a 100 nm n-GaAs ($2 \times 10^{16} \text{ cm}^{-3}$) were grown epitaxially. Finally, a 0.5 μm highly doped n-GaAs ($4 \times 10^{18} \text{ cm}^{-3}$) capping layer was grown to complete the structure. This layer act as the n-type ohmic contact for the device. Circular gold mesas with a ring diameter of 400 μm and area $\sim 5 \times 10^{-4} \text{ cm}^2$ as top metal contacts were made to facilitate optical access from above.

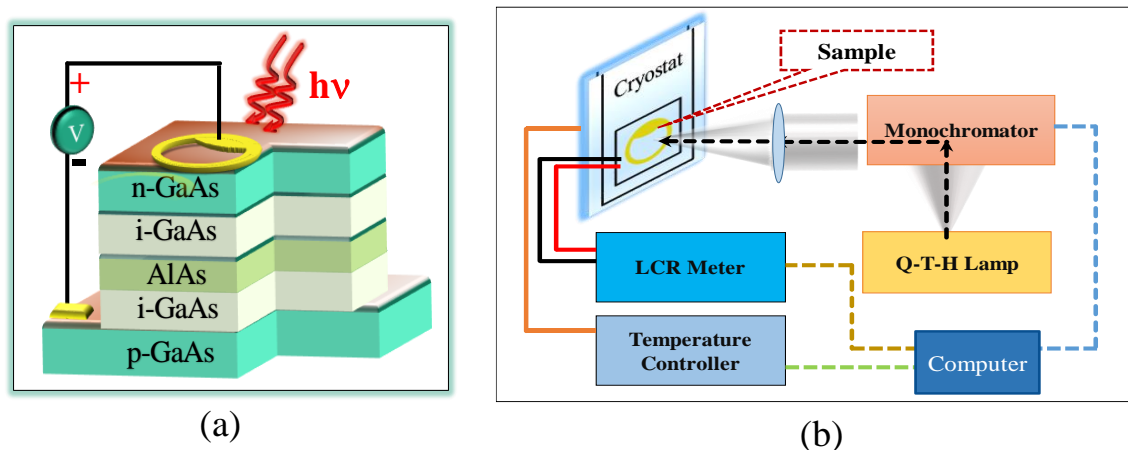


Figure 4.5: (a) A schematic of the p-i-n single barrier heterostructure. The device is operated under optical excitation and applied external biases. (b) A sketch of the experimental set-up used to measure the opto-electrical parameters.

A schematic structure of the sample in figure 4.5(a) having the layer's arrangements will help the readers to get an idea of the device configuration.

Agilent's E4980A LCR meter with 30 mV of rms voltage at a frequency (f) was used to measure capacitance (C) and conductance (G) of the device. A simple equivalent circuit consisting of capacitance and conductance in parallel was used to extract photocapacitance using the LCR meter such that $|C|$ is always greater than $|0.1 \times G/\omega|$ where $\omega = 2\pi f$. DC-current were measured using both LCR meter in the DC mode and a Keithley 2611 source meter. To measure the photo-induced changes in electrical components, we excite the sample with light of an appropriate wavelength. Photocapacitance ($C_{photo} = dQ/dV$) is measured under applied bias while our sample is illuminated from the top n-GaAs side. A 1000 Watts quartz-tungsten-halogen lamp and Acton Research's SP2555 monochromator having 0.5 m focal lengths were used as a light source. Spectral response of lamp plus monochromator changes slowly and monotonically within the wavelength ranges used in our measurements.

PL spectra are measured using a 35-mW He-Ne gas laser and CCS200 compact spectrometer from Thorlabs with a spectral accuracy < 2 nm at 633 nm. For temperature variation, we use a closed-cycle helium gas CS-204S-DMX-20 cryostat from Advance Research Systems along with a Lakeshore (Model-340) temperature controller. In figure 4.5(b), a schematic of the measurement set-up is drawn.

4.6 Part A: Dipolar signature of indirect excitons using photocapacitance technique at room temperature

4.6.1 Results and observation

The primary characterization of a semiconductor device is accomplished by measuring the current (I) versus voltage (V) and capacitance (C) versus voltage plots. Accordingly, in figures 4.6(a) and 4.6(b), we plot DC current and capacitance (at a frequency of 5 kHz) against applied bias under dark and in the presence of light. The selective photoexcitation of 870 ± 3 nm wavelength is performed on the top n-type side of the heterostructure. This specific wavelength of 870 nm matches with the energy bandgap of bulk GaAs at room temperature. So, we used this excitation wavelength to photo excite the electrons and holes just above the band edge of GaAs. We clearly visualize significant photo induced enhancement in both DC-current and capacitance values under finite applied biases.

However, we refrain from any quantitative estimates of carrier density of a particular charge from capacitance versus bias characteristics, which are strictly valid only under depletion approximation for a one-sided junction.

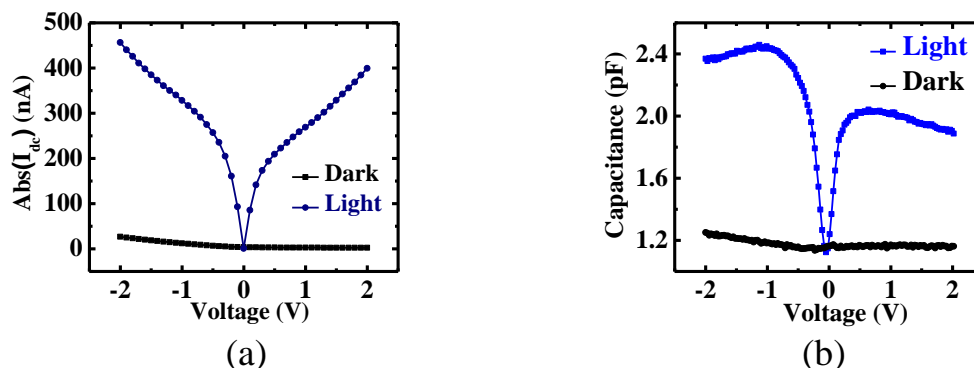


Figure 4.6: (a) and (b) DC current and capacitance (at 5 kHz) are measured with respect to applied bias under the presence of both light and dark condition at room temperature, respectively.

Such estimates are even more complicated as there is no uniform equipotential surface under photoexcitation with a ring-shaped top contact and also due to the presence of both types of carriers across the AlAs barrier. It is likely that a surface Schottky barrier is created between the top metal contact and the top GaAs layer. This, however, goes away when sizable photo absorption biases that surface barrier in the forward direction. Henceforth, in this work, we will only focus on the variation of capacitance and current under non-zero biases and the presence of light. It is well known that large DC-currents can destroy quantum effects due to dielectric screening and averaging effects. We carefully selected top mesa contacts for which DC-photocurrents are restricted within nano-Ampere ranges under reasonably small applied biases of a few volts. Therefore, such sub-micro Ampere DC-photocurrents are also crucial for observing experimental signatures of quantum confined indirect excitons which are only a small fraction of the total number of photogenerated electrons and holes.

Now, we will comprehend how the formation of indirect excitons can be identified if at all they are present in the system. In figures 4.7(a) and 4.7(b), we show photocapacitance spectra for a fixed frequency (1.0 kHz) under both reverse and forward biases, respectively. Initially, photocapacitance peak amplitude gradually increases with increasing bias levels. After certain applied bias values, the magnitude of photocapacitance starts decreasing. Moreover, in the reverse bias, we observe more distinctly sharp resonant peak features in the photocapacitance spectra in comparison to the forward bias. This kind of sharp peak signature

in the phot capacitance spectra portray steady-state photo-generated excitonic presence, identical to standard absorption spectra in a semiconductor.

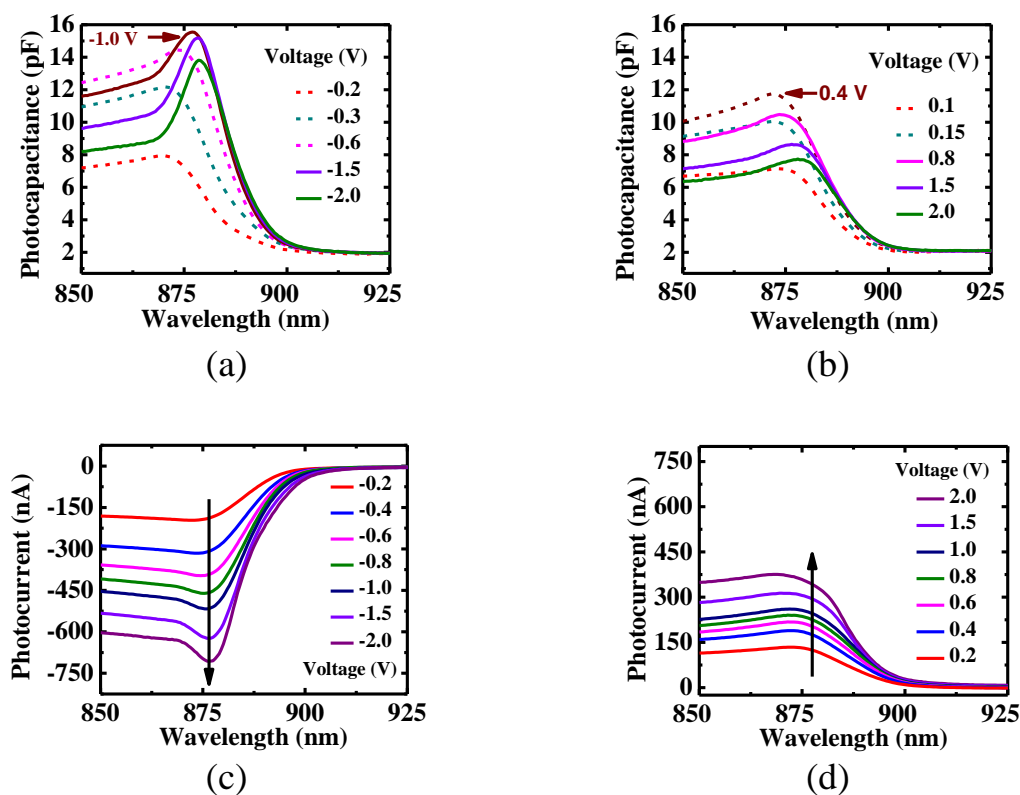


Figure 4.7: (a) and (b) We plot the variation of photocapacitance spectra for different reverse and forward biases, respectively. Photocapacitance peak magnitude initially increases with the bias and then start falling after certain bias values. (c) and (d) Photocurrent spectra for different reverse and forward biases are measured, respectively. In comparison to the photocapacitance spectra, photocurrent spectral amplitude always increases with the biases and also does sign change with the polarity of the applied bias.

Likewise, figures 4.7(c) and 4.7(d) show the DC-photocurrent spectra at different reverse and forward biases, respectively. A peak like excitonic transitions is also visible in these photocurrent spectra under reverse bias. Usually, any peak feature in optical absorption spectra of a semiconductor indicates resonant excitonic transitions. As such, both photocapacitance and photocurrent spectra are dependent on optical absorption spectra. Nevertheless, space charge modifications, charge carrier transport, and electronic defects can significantly influence the respective magnitudes and shapes of these spectra. Similar pronounced peaks may also appear in linear optical absorption spectra due to strong¹²⁶ light-matter interaction inside a resonant optical cavity. However, this single barrier heterostructure and the moderate

levels of photon flux ($\sim 10^{15}/\text{cm}^2$) used in our measurements for photogeneration certainly do not fall into the above category. It is quite evident from figure 4.7(a) that finite, reverse bias larger than -0.2 V is required to observe the prominent spectral signature of excitonic transitions.

We roughly estimate the applied electric fields at each bias by dividing the bias magnitude with the thickness (~ 208 nm) of the intrinsic region of the heterostructure. In addition, we understand that applied electric field across single barrier heterostructure is not only influenced by immobile ionized charges of the GaAs/AlAs/GaAs heterojunction but also by accumulated charge carriers across the AlAs barrier. The high density of charge carrier accumulations across the AlAs barrier was earlier argued^{127,128} to be the main cause for the inverted band structure under high forward bias as also clearly demonstrated in figure 4.2(c).

In section 4.2, we have discussed how a strong electric field can dissociate direct excitons^{129,130} and broadens excitonic transitions in semiconductor quantum wells. However, we notice an opposite scenario in our photocapacitance spectra in reverse bias. In figure 4.7(a), we observe that photocapacitance signature of excitonic resonances become sharper as the reverse bias is increased from -0.2 to -2.0 V. Excitonic peak heights in photocapacitance initially increase with increasing reverse (figure 4.7(a)) and forward (figure 4.7(b)) biases up to -1.0 V and $+0.4$ V, respectively. Beyond these values, the photocapacitance magnitude of excitonic peaks reduce and also show a spectral shift towards low energy. As evident from figures 4.7(a) and 4.7(b), excitonic peaks are more prominent and sharper under reverse bias than forward bias. On the contrary, excitonic peaks of photocurrent spectra (figures 4.7(c) and 4.7(d)) are much less prominent, change sign under opposite biases and do not redshift with increasing biases. All these differences indicate that excitonic populations contributing to photocapacitance and photocurrent spectra have somewhat different physical origins. We will try to explain the possible causes of these differences in the next section.

4.6.2 Discussion

I. Schematic energy band diagram and carrier dynamics

Now, to understand the internal carrier dynamics across the interface of the GaAs/AlAs/GaAs heterostructure, we draw the schematic energy band diagrams in figures 4.8(a) and 4.8(b) for both the reverse and forward biases, respectively. The intrinsic region of

this heterostructure is made of direct and indirect bandgap materials GaAs and AlAs, respectively. So, there is a possibility of band mixing in these kinds of devices. Accordingly, there are reports^{127,128} of Γ -X valley mixing in GaAs/AlAs/GaAs heterostructure, studied at low temperature under high forward bias. However, for AlAs barrier thinner than 3 nm, it is reported¹²⁷ that Γ -band of the AlAs material actively participate in the carrier transport. Due to higher Γ -AlAs potential barriers for both conduction and valence bands, direct tunnelling of carriers are suppressed in this kind of heterostructure. As the barrier thickness of our device is ~ 8 nm, we find that considering the Γ -band instead of X-band will be helpful to explain our result better. Accordingly, we provide following explanations to establish our proposition regarding the Γ -AlAs potential barrier.

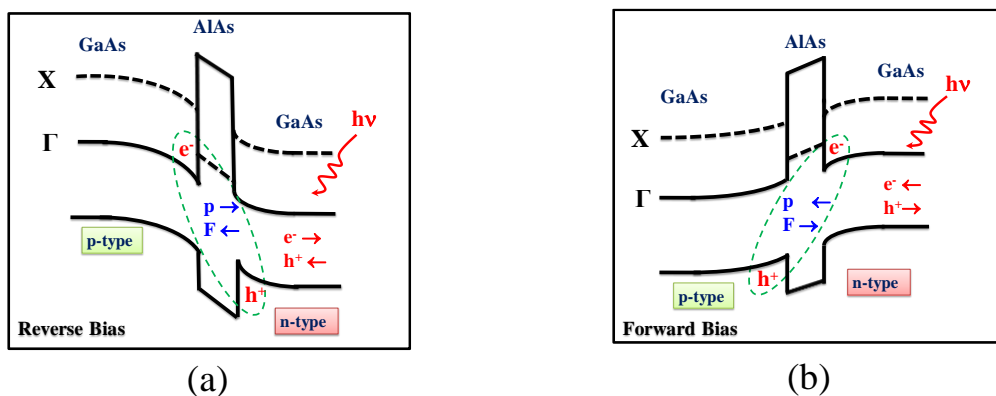


Figure 4.8: (a) and (b) Schematic energy band diagrams for an 8 nm single barrier p-i-n GaAs/AlAs/GaAs heterostructure are drawn for both reverse and forward bias, respectively.

The electrostatic field across the intrinsic region of p-i-n GaAs/AlAs/GaAs barrier simply bend the effective bands and thus, there is a formation of TQWs in both side of the AlAs barrier as shown in figures 4.8(a) and 4.8(b). In our case, it is likely that photogenerated electrons and holes in GaAs are driven by applied bias to accumulate on both sides of Γ -AlAs potential barrier. Due to such charge accumulations, 2D electron-gas (2DEG) and 2D hole-gas (2DHG) are formed across the Γ -AlAs barrier in respective triangular quantum wells (TQWs) in two spatially separated GaAs layers¹³¹. Proximity of these 2DEG and 2DHG allow the formation of indirect excitons by Coulomb attractions as shown in figure 4.8.

However, if we still want to consider indirect excitons within the X band of AlAs¹²⁷, which have a much smaller conduction band offset at Γ -GaAs/X-AlAs/ Γ -GaAs heterostructure,

then significant inter valley electron injection can also occur under applied bias. Such electrons can then recombine with holes of 2DHG. At temperature $\sim 2\text{K}$, this was shown to have a dominant contribution to conductivity and electroluminescence¹²⁷. Therefore, in this context, we want to mention the following points in connection with our room temperature measurements. Firstly, any significant Γ -X- Γ inter valley electron tunnelling, if present at room temperature, can deplete indirect excitons through radiative recombination and subsequently enhance tunnelling conductivity even at smaller biases. Moreover, this Γ -X- Γ electron transport through inter-valley tunnelling is highly dependent on applied bias and must show excitonic stark effects due to effective quantum confinement of electrons within X-GaAs/X-AlAs/X-GaAs band configuration. However, we do not observe any redshift of excitonic photocurrent spectra with applied bias (figures 4.7(c) and 4.7(d)). We will also see that the estimated diameter of indirect excitons is sufficiently large and approaches the thickness of this Γ -AlAs barrier under higher biases. However, thermal activation of charge carriers over the AlAs barrier may also contribute substantially to photocurrents measured at room temperature. Finally, it is also improbable that this Γ -X- Γ inter-valley tunnelling current can be a significant fraction of the overall photocurrent as the majority of photo generations take place in bulk GaAs layers. Therefore, we will restrict our subsequent discussions on indirect excitons formed only across this Γ -AlAs barrier instead of X-AlAs.

It is also important to consider that most of these photocurrents originate from excitonic photo absorptions in the top n-type GaAs layer (figure 4.7(c)). A sizable fraction of these excitons possibly form away from the GaAs/AlAs heterojunction. Furthermore, direct excitons in bulk GaAs are known to have a binding energy of ~ 5 meV. Therefore, most bulk excitons generated within a depth of a few microns from the top n-type layer can either thermally dissociate or drift apart under the applied electric field into electrons and holes at room temperature. These electrons can quickly flow out of the heterojunction under reverse bias. However, holes from these remote excitons cannot overcome the high Γ -AlAs barrier and hardly contribute to DC-photocurrent under lower biases. Hence, unlike phot capacitance, bias driven flow of carriers out of the GaAs/AlAs/GaAs heterojunction contributes to DC-photocurrent. Nevertheless, in the presence of weaker quantum confinement due to reduced band bending, the number of indirect excitons formed under forward bias is smaller than that of reverse bias. Thus, sharp excitonic absorptions in both phot capacitance and photocurrent spectra under forward bias are barely visible. Moreover, we expect photogenerated holes to move away from the heterojunction under forward bias in n-GaAs layer. In addition, these

holes with larger effective masses are also minority carriers in the top n-GaAs layer. So, they cannot flow out of the heterojunction efficiently like electrons in case of reverse bias. As a result, we see comparatively smaller photocurrent signal under forward bias. We, therefore, emphasize that measured photocapacitance is likely connected with indirect excitons formed within the 2DEG and 2DHG which are on opposite sides of the Γ -AlAs barrier. Whereas, all other excitons photo-generated elsewhere inside the heterostructure can contribute to DC-photocurrent without any visible redshift. We will now present additional experimental results and analyses to justify all these above explanations.

II. Exciton dipole moments and field-induced binding energy

Under applied bias voltages, excitons inside a quantum structure can show quantum-confined Stark Effect (QCSE)¹⁰⁵ as discussed earlier in section 4.2. We also observe a sizable redshift of excitonic photocapacitance peaks under reverse bias as shown in figure 4.9(a). Peak energy shifts by ~ 14 meV within the applied bias range. Recently,¹³² it was reported that a redshift of the peak excitonic energy per applied voltage (i.e. $\delta E_{IX}/V$) remains ~ 10 meV/V. Similarly, we find $\delta E_{IX}/V \sim 8$ meV/V. Inset of figure 4.9(a) displays spectral redshifts of excitonic photocapacitance peaks in the presence of electric field under forward bias. Now, in section 4.2, we have elaborated on the interaction between excitonic dipoles and applied electric field. We have also discussed how the QCSE and observed spectral peak energy shift are governed by the energy expression, derived in equation 4.1. In this case, we find the peak energy shift with the applied field follow a specific trend (figure 4.9(a)) and we want to apply a similar analogy here to interpret experimental observation. Variation of peak energy (E) of excitonic photocapacitance signal with applied electric field (\vec{F}) is fitted with the following relation¹⁰⁶⁻¹⁰⁸.

$$E = E_0 + \vec{p} \cdot \vec{F} + \beta \vec{F}^2 \quad (4.4)$$

where E_0 is zero field energy, \vec{p} is permanent dipole moment of indirect excitons, and β is polarizability. Using equation 4.4, we obtain reasonably high values of dipole moments as $\vec{p} = (+7.5 \pm 0.7) \times 10^{-28}$ C.m and $\vec{p} = (-2.0 \pm 0.2) \times 10^{-28}$ C.m for reverse and forward biases, respectively. The signs in front of \vec{p} take care of respective directions of excitonic dipoles. Interestingly, dipole moments (\vec{p}) and applied electric fields (\vec{F}) are always

in the opposite direction. Such anti-parallel alignments of \vec{p} and \vec{F} are shown in figures 4.8(a) and 4.8(b). These are certainly not the lowest energy configurations for these excitonic dipoles. Therefore, this change in sign of effective built-in dipole moment with changes in the direction of bias fits well with our band diagrams (figures 4.8(a) and 4.8(b)) which display ‘inverted’ dipoles of indirect excitons. We estimate polarizability as $+4.5 \times 10^{-35} \text{ C m}^2 \text{ V}^{-1}$ and $+1.2 \times 10^{-35} \text{ C m}^2 \text{ V}^{-1}$ under reverse and forward biases, respectively. Therefore, this analyses corroborate our discussions in the previous section and provide an understanding of how photocapacitance is able to detect the indirect excitons by sensing their dipolar contributions. Such a sizable redshift also raises the binding energy of these indirect excitons, which will be illustrated in the next paragraph.

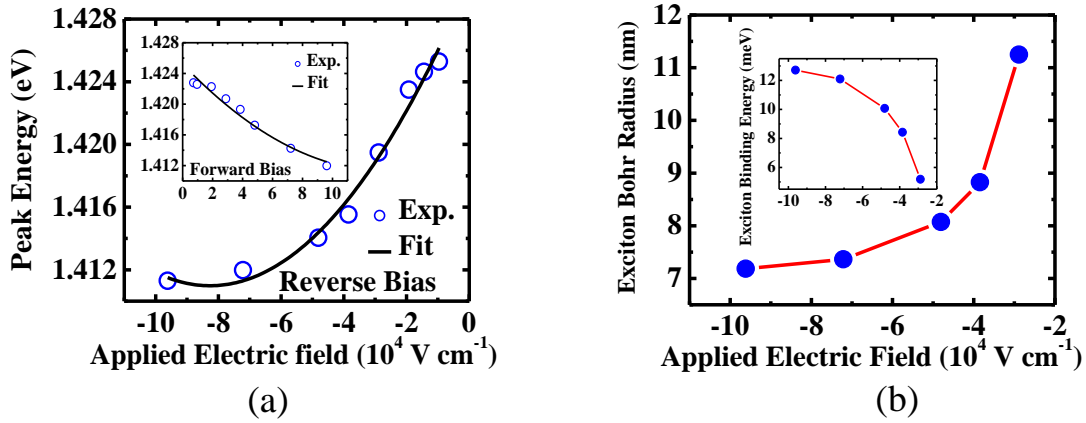


Figure 4.9: (a) Peak energy of the photocapacitance spectra redshift with the applied electric field for both reverse and forward bias (inset). The experimental variations are fitted with equation 4.4 to extract the corresponding values. (b) Excitonic Bohr radius decreases with the applied electric field. Accordingly, excitonic binding energy enhances with the electric field (inset).

When the electrons and holes come closer, then their binding energy also becomes stronger due to enhanced Coulomb attraction. In order to check this, we tried to analyze the redshifts of excitonic resonance in photocapacitance spectra from a different perspective. Here, we assume that the observed redshifts mostly come from bias induced changes of this 2D quantum-confined indirect excitons. Subsequently, we estimate the difference in average separation between these constituent electrons and holes of the 2DEG and 2DHG, respectively, using the following simplified formula

$$E = E_g - \left(\frac{\hbar^2}{2\mu a_B^2(V)} \right) + \mathcal{O}(TQW) \quad (4.5)$$

where E is the excitonic peak energy from the photocapacitance spectra, $E_g = 1.424 \text{ eV}$ is the bulk bandgap of GaAs at room temperature, $a_B(V)$ is effective Bohr radius of indirect excitons which is a function of applied bias V , $\mu \sim 0.058m_0$ is the reduced mass of excitons in GaAs, m_0 is the free electron mass. Here, we call the 2nd term within the first bracket in equation 4.5 as the effective binding energy of these indirect excitons. The last term $\mathcal{O}(TQW)$ is, however, neglected in our estimation. This $\mathcal{O}(TQW)$ term may be dependent on separate quantum confinements of electrons and holes in two different TQWs and also on bias induced changes of these quantum wells. As a result, we note that our simplified analyses may underestimate this effective binding energy. However, for this study, we will focus only on bias dependent changes of $a_B(V)$ as shown in figure 4.9(b). Here we observe that with increasing electric field under reverse bias, the effective excitonic diameter ($= 2a_B$) of indirect excitons along the growth direction gradually decreases. In fact, we notice that the excitonic diameter approaches the average distance between the TQWs across the AlAs barrier. Binding energies of direct excitons are expected to reduce with increasing electric field if these are torn apart and subsequently ionize. However, in our case, qualitative estimates of effective binding energies of these indirect excitons increase with increasing reverse bias [inset of figure 4.9(b)]. This matches well with our interpretation of indirect excitons from the band diagrams shown in figures 4.8(a) and 4.8(b). Such characteristically opposite variation of effective binding energy with increasing applied bias further reinforces our claims that photocapacitance is selectively probing these indirect excitons whose size decrease under increasing reverse bias. We would like to emphasize here that, the formation of indirect excitons in this context solely bias dependent and as the bias increases the binding energy as well as the Bohr radius change accordingly. At zero external bias, there is hardly any possibility of indirect excitons formation. It reaffirms that all these other excitons (like direct excitons, etc.) which contribute mostly to excitonic photocurrent are photo-generated far away from the AlAs barrier. This is because remote excitons are not expected to significantly alter space charge regions near the barrier within the time scale of our photocapacitance response. Hence, these hardly contribute to steady-state photocapacitance.

In figure 4.10, we plot the photocapacitance versus photon flux for -1.0 V reverse bias and $877 \pm 3 \text{ nm}$ photoexcitation wavelength. This selected wavelength corresponds to a maximum excitonic absorption under -1.0 V. Here, we will understand how a small fraction of

photogenerated electrons and holes gradually come closer to form indirect excitons with the applied bias and contribute to photocapacitance. We assume that photocapacitance magnitude is proportional to ηN^α where N is the photon flux, η is the fraction of incident photons which converts to indirect excitons and α is the power-law exponent. Dipolar dispersion of complex permittivity under simplistic driven, damped, simple harmonic oscillator model is always proportional to the number density of polarizable dipoles. We, therefore, assume that the photocapacitance signal has a one-to-one correspondence with an areal density of these dipoles of indirect excitons (n_{IX}). Also, we find that $\alpha \rightarrow 1$. This indeed supports our explanation that photocapacitance is directly proportional to the density of dipolar indirect excitons. The fitted value of the fraction η of 6.6×10^{-5} then provides us with a reasonable upper limit of $n_{IX} \cong 1.2 \times 10^{11}/\text{cm}^2$ for a photon flux of $1.85 \times 10^{15}/\text{cm}^2$ used to measure the spectra.

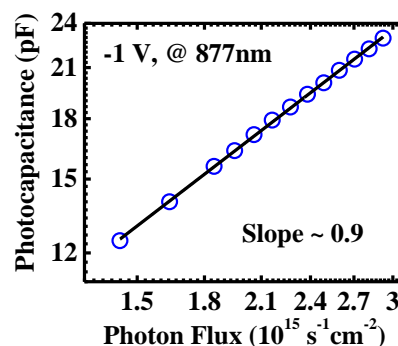


Figure 4.10: To understand the power-law dependence, photocapacitance peak value is plotted with the excitation photon flux. We find the power-law exponent as ~ 0.9 which certainly confirms the presence of excitons in the system.

It is well known that quantum confinement increases the binding energy of 2D excitons by nearly a factor of four^{11,72}. Therefore, such relatively larger values of exciton binding energy as estimated from the experimental data indicates that both electrons and holes of indirect excitons are possibly forced together by the external electric field to be confined in the TQWs as 2DEG and 2DHG, respectively. Moreover, dissociation of excitons into electrons and holes inside a solid is a many-body statistical process with excitonic dissociation probability $\sim \exp\left(-\frac{E_b}{k_B T}\right)$, where E_b is the exciton binding energy^{133,134}. This clearly shows that even when binding energy E_b is smaller than thermal fluctuation energy ($k_B T$), there are still finite, non-zero probabilities of having some bound states of excitons. This analysis also agrees well with our above observation that only a very small fraction ($\sim 10^{-5}$) of photo-generated

electrons and holes form these indirect excitons. In addition, a significantly smaller optical dielectric constant of AIAs as compared to GaAs also enhances their binding energy, which in turn allows such quantum-confined indirect excitons to survive even at room temperature.

III. Supporting analysis and frequency-dependent phot capacitance

In this section, we want to provide some additional analyses to back up the experimental observation in figure 4.7. In figure 4.11(a), we plot the magnitude of excitonic phot capacitance peaks under reverse biases. It increases up to a bias of -1.0 V and then decreases for higher biases. Similar behaviour is observed for forward biases in the inset of figure 4.11(a). This is certainly related to the ongoing tunnelling of electrons and holes through the Γ -AIAs. This tunnelling can subsequently reduce the population of indirect excitons, which is reflected in the variation of the peak value of excitonic phot capacitance (figure 4.11(a)). To confirm this, we verify the applicability of Fowler-Nordheim (FN)^{135,136} tunnelling at higher biases. Accordingly, we find that the following FN expression can be fitted with the DC-photocurrent density (J_{FN})

$$J_{FN} = \frac{q^3}{16\pi^2 \hbar \Phi_b} F^2 \exp\left(-\frac{4\sqrt{2m^*}}{3\hbar q} \Phi_b^{\frac{3}{2}} \frac{1}{F}\right) \quad (4.6)$$

where q is the electron charge, \hbar is reduced Planck's constant, m^* is effective mass of the electron (hole) in GaAs, Φ_b is the effective barrier height at the GaAs/AIAs interface and F is the applied electric field across heterostructure. In figure 4.11(b), we show the Fowler-Nordheim plot for reverse biases and forward biases (inset). Characteristic linear regions at higher biases indicate the presence of tunnelling, which also coincides with bias induced reduction of excitonic phot capacitance peaks. Therefore, it establishes that the tunnelling process reduces the density of indirect excitons resulting in a significant decrease of the excitonic contribution in phot capacitance spectra (see figures 4.7(a), 4.7(b) and 4.11(b)). Remarkably, tunnelling through Γ -AIAs affects excitonic phot capacitance and photocurrent spectra differently. Electrons and holes of indirect excitons can preferentially tunnel at higher biases due to their proximity to the AIAs tunnel barrier. However, this tunnelling current likely contributes a negligible fraction to the overall increase of bulk photocurrent signal and it does not shift the excitonic peak with increasing biases. It is worth noting that electrons having low effective mass (m^*) can easily penetrate the AIAs quantum barrier as compared to holes. This

is due to the fact that the wave function inside AIAs tunnel barrier varies with position (x) as $\sim(\exp(-\kappa x), \kappa \sim \sqrt{m^*})$.

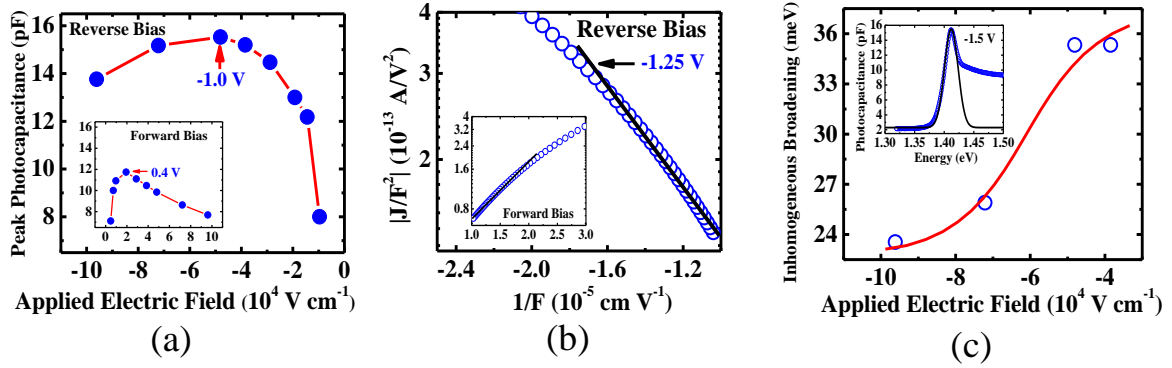


Figure 4.11: (a) The magnitude of the peak photocapacitance initially increases and then falls when the threshold voltage for tunnelling is reached for both the reverse and forward bias (inset). This was also very evident in the spectral signature in figures 4.7(a) and 4.7(b). (b) Fowler-Nordheim plot to comprehend the ongoing tunnelling in the higher reverse and forward bias (inset). (c) Spectral broadening varies with the applied electric field under reverse bias. Excitonic linewidth decreases with the electric field. The inset shows that the Gaussian line shape matches well with the excitonic photocapacitance spectrum.

It is well known that fluctuations in quantum well width and inhomogeneity in alloy compositions can give rise to inhomogeneous broadenings of its optical spectra. Interestingly, inhomogeneous line widths of excitonic peaks of photocapacitance spectra shown in figure 4.11(c) decrease with increasing electric field associated with reverse bias. The strong presence of inhomogeneous broadening is exemplified in the inset of figure 4.11(c), where the excitonic peak in photocapacitance spectra matches to a simple Gaussian line shape. Earlier photocurrent spectroscopy¹³⁷ was used to probe excitons within a quantum well, where electrons and holes are pushed in the opposite direction in order to broaden the excitonic peaks with increasing electric fields. However, in our case, there is a potential barrier in the middle of GaAs/AIAs/GaAs heterojunction and resultant charge carrier dynamics are totally different. Here, with increasing bias, photogenerated electrons and holes of the indirect excitons come even closer towards each other as already observed in figure 4.11(c). Therefore, it results in an unusual sharpening of excitonic photocapacitance with increasing reverse bias. This result again substantiates our interpretations of indirect excitons following the schematic band

diagrams given in figures 4.8(a) and 4.8(b). In a way, it also validates the explanations given along with equation 4.5.

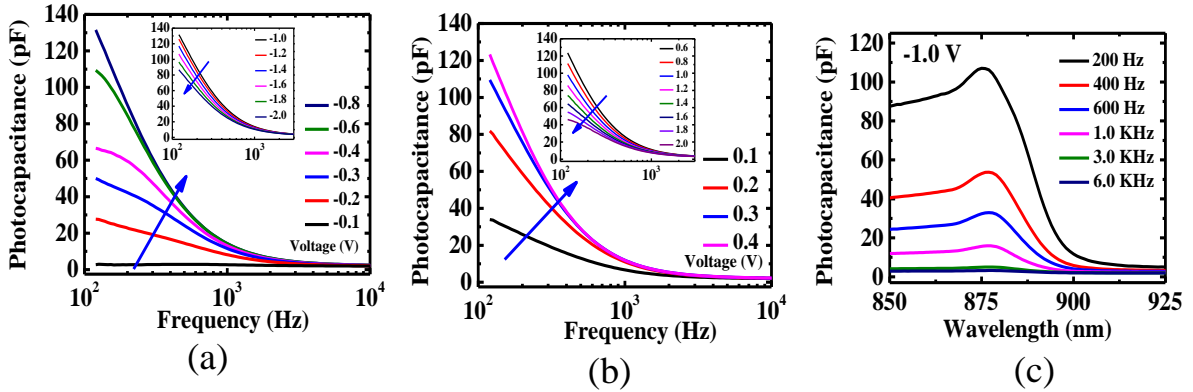


Figure 4.12: (a) and (b) Photocapacitance as a function of frequency varies with the reverse and forward, respectively. The photocapacitance initially increases and then decreases (insets) with biases. The blue arrow points toward the increasing of applied biases. (c) Photocapacitance spectra for a fixed reverse bias -1.0 V are plotted for different frequency modulation.

In the previous chapter, we have shown how a thermodynamic population of dipolar excitons in quantum confined laser diodes can respond to steady-state differential capacitance measurements and shift towards higher applied frequencies with increasing bias. Figures 4.12(a) and 4.12(b) show that excitonic photocapacitance values clearly increase and shift to higher frequencies with increasing bias under 870 ± 3 nm selective photoexcitation (increasing bias is shown by the arrows inside these figures). This supports the proposed⁸ electrical signatures of the formation of excitons. As stated above, tunnelling reduces the number of accumulated electrons and holes in respective 2DEG and 2DHG regions, where these indirect excitons are located. As a result, photocapacitance signal also reduces once tunnelling becomes significant at higher biases (inset of figures 4.12(a) and 4.12(b)).

However, the range of frequency ($\sim 10^2$ to $\sim 10^3$ Hz) for measured photocapacitance response is much smaller compared to frequency ranges ($\sim 10^6$ Hz) reported in the earlier investigations^{138,8,30}. These past studies had only probed direct excitons formed inside quantum structures. On the contrary, here electrons and holes of indirect excitons are physically separated by a large Γ -A1As potential barrier which suppresses¹³⁹ free dipolar oscillation of

excitonic charges. This is expected to cause considerable dipolar relaxation, which can ‘dampen’ the oscillations of indirect excitonic dipoles during steady-state photocapacitance measurements. In these experiments, dipolar relaxation kinetics of indirect excitons involves transitions between two states of opposite charge orientations separated by a large free energy barrier. Therefore, we use the following Arrhenius equation for thermally activated transitions over AlAs barrier

$$E_{Th} = k_B T \ln(v/f) \quad (4.7)$$

where v is the thermal pre-factor $\sim 10^{12}$ Hz, k_B is the Boltzmann constant and T is the temperature in Kelvin. We calculate the effective activation barrier height (E_{Th}) to be ~ 0.56 eV at room temperature. We choose a frequency (f) of ~ 500 Hz where we observe a large photocapacitance response away from its final roll-off at higher frequencies. This effective E_{Th} nearly matches with the reported band offsets at Γ -GaAs/ Γ -AlAs heterojunction where zero bias values of conduction and valence band offsets are $\Delta E_C \sim 0.8$ eV and $\Delta E_V \sim 0.5$ eV respectively. Figure 4.12(c) also shows that the signature of excitonic resonance in the form of photocapacitance peak slowly vanishes above 1.0 kHz. Such low-frequency response can only come from space charge modulation near the AlAs barrier, which directly affects the areal density of indirect excitons probed using photocapacitance. It is well known that space charge dipoles respond around this frequency range¹³⁹.

4.6.3 Summary of part A

In this report, we have provided ample experimental evidence to establish the photocapacitance signature of bias driven, inverted dipoles of 2D indirect excitons formed across 8 nm thin AlAs tunnel barrier in Γ bands of GaAs/AlAs/GaAs heterostructure. We have argued that quantum confinements of photo-generated electrons and holes in triangular quantum wells enhance the excitonic binding energy which effectively increase the thermodynamic probability of these indirect excitons to survive even at room temperature.

We have also analyzed characteristic differences in the electric field dependence of excitonic features in both photocapacitance and DC-photocurrent spectra. In particular, we have shown that large, tunable dipole moment along the growth direction can be engineered to selectively probe, control and manipulate the indirect excitons by photocapacitance using applied bias and modulation frequency. Moreover, peak photocapacitance signal follows a

reasonable upper limit of areal density of photogenerated indirect excitons. Remarkably, the photocapacitance technique which was rarely used in the past to detect excitons can be used to detect indirect excitons which constitute only a small fraction ($\sim 10^{-5}$) of the photogenerated carriers.

Finally, this work opens up the possibility of experimental detection of indirect excitons using photocapacitance at room temperature. It also creates future possibilities for photocapacitance studies to probe the many-body physics of excitons in heterostructures of 2D transition metal di-chalcogenides^{47,48,140-142} using their well-known valley selective charge transport. Significant differences between excitonic signatures of photocapacitance and photocurrent may also be used to address either indirect or direct excitons. Therefore, we predict that all these above findings will also be helpful to design better excitonic devices³⁹.

4.7 Part B: Physics of indirect trions and Fermi-edge singularity at 100 K

4.7.1 Introduction

Presence of excitons and excitonic complexes become more prominent as the temperature of the system is lowered or the thermal energy is equivalent to the binding energy of the bound states. Excitonic complexes like trions have very less binding energy for these III-V semiconductor systems, even quite less than the excitons binding energy. So, trions like low energy bound excitonic states are expected to appear in the low-temperature regime. Henceforth, in this section, we want to probe the signature of trions and other many-body excitonic physics at 100 K. Experimental detection and study of neutral excitons (say X^0) and charged excitons like positive or negative trions (X^+ or X^-) inside two dimensional (2D) semiconductor quantum heterostructures are becoming important for understanding the many-body physics of excitonic complexes^{143,118} as well as for novel applications of excitonic devices³⁹. Existence of trions was first demonstrated in semiconductors by Lampert¹⁴⁴. Since then, there are numerous reports on the optical spectroscopic signatures of trions at low temperatures of few Kelvins as binding energies ($\sim 1-2$ mV) of trions in III-V material system are very small^{109,145,146}. Whereas, trions in 2D monolayers of transition metal di-chalcogenides (TMDC) can have much larger binding energies^{111,113} $\sim 20-50$ meV. Such large binding energies of excitons and trions in TMDC materials can certainly make it much easier, not only to study the many-body physics of excitonic complexes even at room temperature but also for their use in optoelectronic devices. However, there are reports of some disparities between

theoretical and experimental observations of a precise signature of positively or negatively charged trions. Also, the binding energies¹⁰⁹ of these two states are not yet conclusively analyzed. At this point, we understand that identifying a trion as X^+ or X^- depends mostly upon how electrons and holes are being injected with applied bias based on the device configuration. The presence of these excitonic complexes usually occurs in moderate density regimes. Whereas, many-body interactions of charge carriers with Fermi sea lead to Fermi edge singularity (FES) in high-density regimes. Theory^{147,148} and experiments^{122,149,150} of such crossover from excitonic complexes to FES in III-V semiconductors were studied mostly at low temperatures of few Kelvins by optical absorption and photoluminescence (PL) spectroscopies.

In the present study, we report that simple photocapacitance spectroscopy can be used to detect the specific signature of positively charged trions of indirect excitons (IX^+) at moderate levels of carrier densities ($<1 \times 10^{11} \text{ cm}^{-2}$) as well as Fermi edge singularities (FESs) in higher level of carrier densities ($>1 \times 10^{11} \text{ cm}^{-2}$) in a single barrier GaAs/AlAs p-i-n heterostructure. We had already demonstrated that photocapacitance spectroscopy can be used as a sensitive electro-optical tool to probe spatially indirect excitons formed across the AlAs potential barrier in GaAs/AlAs/GaAs heterostructure even at room temperature. Here, we argue why photocapacitance can sense these IX^+ s even at 100 K, which was not possible to detect with photoluminescence. Formations of triangular quantum wells (TQWs) around Γ -AlAs potential barrier also help these spatially indirect trions to survive even at such temperature. We establish that photocapacitance spectroscopy is a more sensitive experimental technique for detecting trions and many-body effects like FES than PL in such heterostructures. We also demonstrate that it is possible to probe and monitor the dielectric properties of strongly correlated, interacting dipoles of excitons, trions, and FES using such capacitance-based techniques even at 100 K. Our observations establish that photocapacitance spectroscopy, which was hardly used to detect trions in the past, can also be useful to detect the traces of these spatially indirect excitonic complexes as well as Fermi edge singularity. This is mainly due to enhanced sensitivity of such capacitive measurements to ‘dipolar’ changes of excitonic complexes in these heterojunctions. Thus, our studies clearly open up future possibilities for electro-optical modulation and detection of trions and Fermi edge singularities in several other heterostructures for next-generation optoelectronic applications.

4.7.2 Results and discussion

I. Presence of indirect positive trions and Fermi edge singularity at 100 K

Stronger appearance of spatially indirect excitons and trions happen near the GaAs/AlAs/GaAs heterojunction when the temperature of the system is lowered around 100 K. The sample is probed under light and applied reverse biases. In figure 4.13, changes in photocapacitance spectra under different applied reverse biases are shown. As the magnitude of reverse bias increases from -0.1 V to higher values, single resonant peak like excitonic spectra is split up into two distinctly separate peaks. This kind of peak splitting with increasing bias was absent at room temperature³¹.

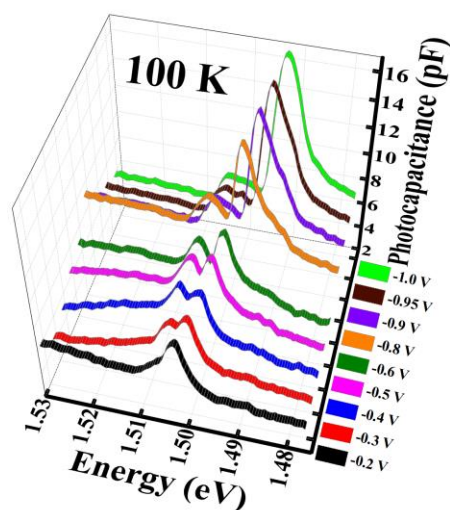


Figure 4.13: Photocapacitance spectral variation with the applied reverse bias is shown in a 3D plot for better representation. A single excitonic peak in the lower bias split into two peaks in the higher bias: one exciton and other trion. After certain voltage ~ -0.8 V, the low energy trion peak shows FES like spectral signature. Last four plots from -0.8 to -1.0 V have been shifted vertically by 2 pF for better visibility.

Initially, the spectral shapes of these peaks remain nearly symmetric until the bias value of -0.6 V. After this, an asymmetric spectral shape emerges where the low energy spectral tails rise slowly and the high energy side falls sharply. In addition, an enhancement of the low energy peak is clearly noticeable around -0.8 V and beyond. On the other hand, the higher energy peak almost vanishes gradually at larger biases.

capacitance-voltage plot which is strictly based on depletion approximation and the presence of a single type of majority carriers.

However, we conceive that large numbers of electrons and holes can accumulate in these TQWs to form 2DEG and 2DHG, respectively, with increasing reverse biases. As a result, corresponding carrier densities in each TQW also increase. So, the charge density of photogenerated carriers per unit area (σ_{ph}) around the heterojunction for each bias values can be estimated from figure 4.13 using the following relationship

$$\sigma_{ph}e = CV \quad (4.8)$$

where e is the electric charge, and C is the peak value of excitonic photocapacitance per unit area at each applied bias (V). Following the description in figure 4.14(a), it is important to note here that one can also relate this σ_{ph} to the density of dipolar charges per unit area in a standard parallel plate capacitor configuration as

$$\sigma_{ph} = \vec{P} \cdot \hat{z} \quad (4.9)$$

where \vec{P} is the effective polarization of these excitonic dipoles around the AlAs barrier and \hat{z} is the unit vector along the growth direction.

At high enough injected carrier density, another peak at the low energy side starts to appear. This happens with $\sigma_{ph} > 3 \times 10^{10} \text{ cm}^{-2}$ or reverse biases higher than $|-0.3| \text{ V}$, as shown in figure 4.13. Evidently, concentrations of holes in the 2DHG become larger compared to those of electrons in 2DEG. This is because the sample is optically excited from the top n-GaAs side only and bias is also applied in the reverse direction. Such excess of one type of carriers (in our case holes) favour the formation of positively charged trions which can be controlled by both light or bias¹⁵². As a result of this excess hole density in 2DHG, we now ascribe the sharp resonant spectral features on the low energy side of the spectra with positively charged indirect excitons or trions (IX^+). Until the bias value reaches -0.6 V or $\sigma_{ph} \sim 8 \times 10^{10} \text{ cm}^{-2}$, both peaks look nearly symmetric. Even though, we see that the trion peak is getting bigger than the exciton peak. This low energy IX^+ state is more energetically favourable and tends to dominate at even higher applied biases.

Subsequently, after the reverse bias around -0.8 V , we observe a drastic change in the spectral behaviour as clearer from figure 4.13. The low energy trion peak indeed rises significantly whereas the exciton peak almost vanishes around $\sigma_{ph} \sim 1.2 \times 10^{11} \text{ cm}^{-2}$. Moreover,

the spectral shape of this trion peak gradually becomes asymmetric in nature. This type of spectral transition is usually^{122, 150, 153} identified with Fermi edge singularities at high enough carrier densities. In our case, we observe similar sharp, asymmetric enhancement of the trion peak in the photocapacitance spectra, once the photo-generated density approaches $\sigma_{ph} \sim 1 \times 10^{11} \text{ cm}^{-2}$. So, we relate this exotic photocapacitance spectral trend as an indication of FES. In the present scenario, it is likely that at higher carrier densities, localized hole states of 2DHG or holes in shallow impurity states can experience enhanced Coulomb attraction with the Fermi sea of electrons in 2DEG at such low temperatures. As a result, we observe a significant enhancement of optical absorption of this trion related FES. Previously, Yusa et al.¹²² had reported asymmetric line shape in absorption spectra, which showed a fast rise in the low energy side and slow fall in the high energy side. Chen et al.¹⁵⁰ and Skolnick et al.¹⁴⁹ had observed a slow rise in the low energy side and fast fall in the high energy side of the PL spectra. Usually, in the high-density limit, enhanced carrier-carrier scattering broadens the high energy tail of FES. However, we notice that photocapacitance spectra in figure 4.13 have much sharper high energy edge in a system consisting of both 2DEG and 2DHG. In addition, we still find the remnant excitonic state above the FES level. Later, we will discuss the effect of sub-bandgap localized states in modifying the photocapacitance spectral broadening in the lower energy side of FES.

Nevertheless, the typical knowledge of FES happens inside a quantum well structure tells that a sea of electrons in the conduction band is usually get attracted to a single localized hole state near the valence band. This follows a power-law singularity¹²² according to equation 4.3 as described in section 4.4. At bias values of -0.8 V, we find $\alpha \approx 0.4$, albeit from the low energy tail of the FES spectra. This value, however, matches with the literature¹²². At this stage, it is important to reiterate that, here, we are dealing with the dual presence of both 2DEG and 2DHG. In a way, we are looking at how a Fermi sea of electrons inside a 2DEG interacts with excess holes localized around 2DHG. The detailed analysis will be explained later in this section.

We want to mention here that the full widths at half maxima (FWHM $\sim 8 \text{ meV}$) of these FES peaks are somewhat lower than the corresponding thermal width $\sim k_B T = 8.7 \text{ meV}$ at 100 K. Moreover, following the discussion by Skolnick et al.¹⁴⁹, we approximate this FWHM value as an estimate of the Fermi Energy. The 2D Fermi energy is usually calculated using the expression of (for spin $\frac{1}{2}$ particles)

$$E_F = \frac{\pi \hbar^2 \sigma_{ph}}{m^*} \quad (4.10)$$

where \hbar is the reduced Planck's constant, σ_{ph} is the dipolar charge density per cm^2 . Here, for these excitonic dipoles around the AlAs barrier, we have used $m^* = \mu$ as the reduced mass of holes and electrons $\sim 0.056m_0$ in GaAs, m_0 is the free electron mass. Therefore, using equation 4.10, we find that $\text{FWHM} \sim E_F = 8 \text{ meV}$ corresponds to $\sigma_{ph} \sim 1.86 \times 10^{11} \text{ cm}^{-2}$ (following the discussion of Skolnick et al. in Ref. 149). This estimate matches closely with $\sim 1.82 \times 10^{11} \text{ cm}^{-2}$, deduced from equation 4.8 at a bias of -1.0 V around where the prominent signatures of FES like asymmetric spectra are visible.

Important to note here that the intrinsic GaAs spacer layers which serve as the arms of the TQWs are $\sim 100 \text{ nm}$. This high value corresponds to a low electric field across the region, and thus TQWs are less confined. So, in these shallow TQWs, we understand that only the first few states of these 2DEG or 2DHG can remain strongly quantum confined, i.e., behave as two dimensional in nature. Higher energy states in TQWs are less localized as the well width becomes wider. We understand this from the quantized energy E_n and n th eigenfunctions $\psi_n(z)$ of an infinite barrier TQW¹⁵⁴, which are given by

$$E_n \sim \sqrt[3]{\left[\left(\frac{\hbar^2}{2m^*}\right) \left[\frac{3\pi e F_z}{2} \left(n - \frac{1}{4}\right)\right]^2\right]} \quad (4.11)$$

and

$$\psi_n(z) = Ai \left[\frac{2m^* e F_z}{\hbar^2} \left(z - \frac{E_n}{e F_z} \right) \right] \quad (4.12)$$

where $n = 1, 2, 3, \dots$, $Ai(z)$ is the Airy functions, m^* is the effective mass of electron/hole, e is the electronic charge, F_z is the electric field along the growth direction along z axis, \hbar is the reduced Planck's constant. The ratio of the first excited energy to the ground state energy is $\frac{E_2}{E_1} = \sqrt[2/3]{\left(\frac{7}{3}\right)} \sim 1.76$. Therefore, it is expected that in practice, with a finite barrier TQW like those shown in figure 4.14(a), only the ground state energy may remain strongly bound and quantum-confined. However, with increasing bias and charge accumulations around the AlAs barrier, the quasi-Fermi levels can suddenly penetrate these TQWs at the onset of FES. As a result, we also observe a sharp transition around a reverse bias of -0.8 V where the exciton-trion spectra suddenly convert into asymmetric FES spectra. This is because, with increasing bias, the quasi-Fermi level E_{Fn} (E_{Fp}) of electrons (holes) can get pinned with the discrete ground state energy of 2DEG (2DHG) in these TQWs. However, the quasi-Fermi Level separation

$(E_{Fn} - E_{Fp})$ can vary along with the ground state energy levels of these electron and hole TQWs as shown in figure 4.14(b). As a result, we find that $(E_{Fn} - E_{Fp})$ can keep on increasing with the increase of reverse bias (electric field) as per equation 4.11. In the absence of any quantum-confined excited states in these shallow TQWs, the maximum optical absorption energy for indirect excitons can then be limited by

$$E_{Opt}^{Max} = E_g + E_1^e + E_1^{hh} \equiv (E_{Fn} - E_{Fp}) \quad (4.13)$$

where E_g is the bulk bandgap of GaAs, $E_1^e(E_1^{hh})$ is ground state energy of electrons (heavy holes). In fact, we observe FES related enhancement at this E_{Opt}^{Max} edge only. In figure 4.14(b), we pictorially depict both high and low energy portion of this FES transition as $E_{high} (=E_{Opt}^{Max})$ and E_{low} following our schematic diagram is given in figure 4.14(a). We assume that quantum-confined holes in 2DHG can be further localized to shallow impurity states or interface trap states or to states related to alloy disorder inside 2DHG near the valence band edge. Any optical absorption from such shallow states near the 2DHG to E_1^e can couple the holes left in these localized states with the 2DEG to create the FES. So, figure 4.14(b) can also explain the broad low energy tail (E_{low}) of the FES spectra as compared to its much sharper high energy side (E_{high}) as found in figure 4.13. Such relative sharpness of the high energy edge of FES can be traced back to intrinsic sharpness of respective Fermi edges as given in equation 4.13. All these understandings are schematically described in figure 4.14(b) and fully support our above explanations based on the formation of positively charged IX^+ at lower bias levels.

II. Spectral redshift and binding energy of indirect trions at 100 K

With applied reverse bias, the spectral peak energy redshifts as evident from figure 4.13. To explain the underlying physics behind this spectral evolution, we plot a 2D colour-filled contour diagram in figure 4.15(a) from the results shown in figure 4.13. This graphic presentation is essential for better visibility of spectral splitting, redshift of low energy IX^+ peak and energy separation of both exciton and trion peaks. Eventually, the low energy trion peak leads to FES with increasing reverse biases. The dashed lines are drawn to guide the eyes only. A clear redshift of IX^+ spectra with the applied bias is visible as mentioned above, whereas the peak energy of IX^0 line hardly shifts. At this stage, it is not fully understood why excitonic peak at slightly higher energy is not at all affected by increasing the electric field.

However, spectral energy separation between two peaks clearly changes and increases with increasing bias as depicted in figure 4.15(a) by two dashed lines.

Firstly, we will comprehend the corresponding physics following the report of Bugajski and Reginski¹⁵⁵, which discuss the transformation of trions into FES spectra. In the parabolic band approximation, the Fermi energy E_{Fn} of electrons in the bulk can be written in the form of low energy onset of absorption (ε_F) and emission edge (ε_g) as

$$E_{Fn} = (\varepsilon_F - \varepsilon_g) \left(1 + \frac{m_e^*}{m_h^*}\right)^{-1} \quad (4.14)$$

where $\left(\frac{m_e^*}{m_h^*}\right)$ is the effective mass ratio of electron and hole of GaAs. The Fermi energy varies with photogenerated carrier density. As discussed previously, we are driving both photogenerated electrons and holes towards the AlAs barrier. So, the gap between the quasi-Fermi levels ($E_{Fn} - E_{Fp}$) should increase with increasing bias. However, this change in E_{Fn} can be more in comparison to changes in E_{Fp} , because, in general, Fermi levels are inversely proportional to the effective mass of the respective carrier and $\left(\frac{m_e^*}{m_h^*}\right) \ll 1$. As there is no observed change in the low energy onset ε_g of photoluminescence (as will be shown later) with increasing reverse bias, we may infer that ε_F may actually blue shift with increasing bias. Here, we assume that any change in the effective mass ratio as a result of bias induced changes in the shape and size of TQWs is negligible. Consequently, FES related enhancement of photocapacitance spectra at $E_{Opt}^{Max} = (E_{Fn} - E_{Fp})$ should also show a blue shift with increasing reverse bias greater than -0.8 V. However, we see the opposite effect and the high energy edge of FES actually redshifts. As we know that FES is a many-body excitonic phenomenon and in our case, this involves the presence of both 2DEG and 2DHG. Therefore, understanding the redshift of FES peak will not be possible without considering how these indirect excitonic complexes and Fermi levels are evolving with increasing bias in such heterostructure. Similar to our room temperature indirect excitons study, we understand here that the electrons and holes of IX^+ can come closer with increasing bias. Consequently, the binding energy of this IX^+ can increase with increasing bias. This can lead to the observed redshift of this trion FES edge due to opening up of an excitonic gap. On the other hand, this significant ~ 10 meV redshift of IX^+ line with the applied bias in this coupled TQWs structure may also be related to quantum-confined Stark effect (QCSE) where exciton peaks usually broaden with increasing electric field.

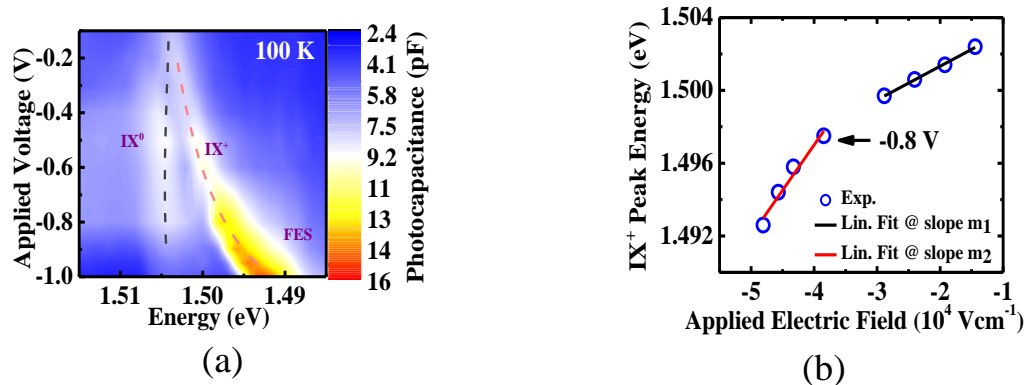


Figure 4.15: (a) A 2-d colour contour plot of photocapacitance spectra for different applied voltages is drawn to visualize the spectral trend much better. A significant redshift of the IX^+ line and the visible splitting of the spectra with bias are clearly pointed out. The black and red lines are drawn to guide the eyes only. (b) The linear variation of peak energy of positively charged trion with increasing electric field is demonstrated to estimate the permanent dipole moments. There is a clear discontinuity around -0.8 V with a field of -3.8×10^4 V cm $^{-1}$.

The magnitude of this peak splitting initially increases slowly and then in the higher bias regime it varies significantly as also reported by Yusa et.al¹²². With increasing bias the carrier density also increases, which eventually contributes to strong scattering mechanisms. However, a rigorous explanation of spectral broadening of FES requires understanding the complete picture of many-body scattering mechanisms and extrinsic carrier dynamics within such single barrier heterostructure, which is currently beyond the scope of this study. However, in figure 4.15(b), the spectral redshift of the trion peak energy has been fitted with linear dipole moment equation

$$E = E_0 + \vec{p} \cdot \vec{F} \quad (4.15)$$

where E is peak energy of IX^+ , E_0 is the energy at zero applied field, \vec{p} is the effective permanent dipole moment of these trions and \vec{F} is the applied electric field. We can see that \vec{p} and \vec{F} are directed opposite to each other (see figure 4.14(a)). Also, \vec{p} is anticipated to be independent of \vec{F} at such low temperature because of the observed linear variation of E with \vec{F} . Two regions of the bias dependent photocapacitance spectra have been fitted with two separate straight lines with slopes m_1 and m_2 . These slopes actually estimate the values of respective dipole moments. Slope m_1 corresponds to the dipole moment value $\sim 2.96 \times 10^{-28}$ C-m before

the onset of FES. However, we get substantially larger value of this dipole moment from slope $m_2 \sim 7.97 \times 10^{-28}$ C-m for higher bias region when FES get started. In the higher electric field regime, there will be more carrier injections to the TQWs. Following equation 4.9 and figure 4.14(b), this eventually contributes to larger dipolar polarization as compared to that in lower biases.

We have already mentioned that exciton peaks gradually decrease and hardly shift in energy with increasing applied bias, whereas the trion peaks slowly enhance and redshift remarkably after certain applied bias. This can happen if more and more positively charged trions (IX^+) form at the expense of excitons (IX^0) in the presence of excess holes. Moreover, the trion peak ultimately converts to FES after a specific density regime, which is in our case around 1×10^{11} cm⁻². This understanding matches well with explanations provided by Huard et al.¹¹² Accordingly, we plot the energy difference between two peaks with the estimated Fermi energy for each applied bias in figure 4.16(a). This is then linearly fitted with the following relation^{108,112},

$$E_{IX^0} - E_{IX^+} = E_{IX^+}^b + E_{Fp} \quad (4.16)$$

where $E_{IX^+}^b$ is the positive trion binding energy, E_{IX^0} and E_{IX^+} are peak energies for indirect excitons and positive trions respectively and E_{Fp} is the Fermi energy change due to extra holes in the valence band. E_{Fp} is estimated from photo-generated carrier density using equations 4.10 and 4.8 with effective mass of hole as $m_h^* \sim 0.45 m_0$ in GaAs. From the intercept, we estimate the value of an average trion binding energy of $E_{IX^+}^b \sim 2.0$ meV. However, we are also assuming here that the estimated value of $E_{IX^+}^b$ using the above equation 4.16 is independent of applied bias. Interestingly, it matches well with earlier reported value in GaAs/AlAs system^{109,145,146,156}. This supports our spectroscopic confirmation of the presence of trions (IX^+) using photocapacitance. Whereas, previous reports mostly estimate this binding energy from PL measurements, here we show that trion binding energy can also be determined from photocapacitance spectroscopy.

Moreover, we note that dissociation of either excitons or trions inside a solid is always a many-body statistical process with thermodynamic dissociation probability $\sim \exp\left(-\frac{E^b}{k_B T}\right)$, where E^b can be either the exciton or the trion binding energy^{133,134,152}.

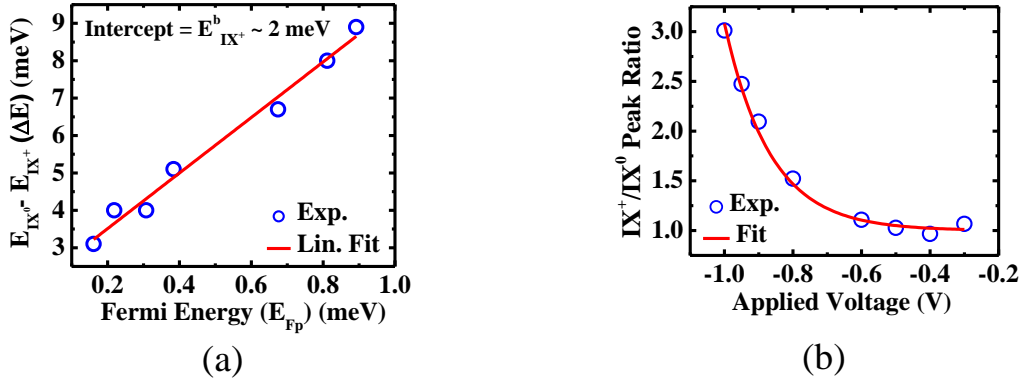


Figure 4.16: (a) The splitting energy (ΔE) between exciton and trion peaks is plotted with respect to Fermi energy. The estimated value of trion binding energy from the fitted straight line is relevant to previous reports. (b) The ratio of trion over exciton peak magnitude changes with applied reverse bias.

This is because such dissociations are typically governed by the following Saha's ionization equations^{133,134}.

$$\frac{n_h n_e}{n_{X^0}} = \frac{C_{X^0}^2}{C_e^2 C_h^2} \exp\left(-\frac{E_{X^0}^b}{k_B T}\right) \quad (4.17)$$

$$\frac{n_X n_h}{n_{X^+}} = \frac{4C_{X^+}^2}{C_X^2 C_h^2} \exp\left(-\frac{E_{X^+}^b}{k_B T}\right) \quad (4.18)$$

where $E_{X^0}^b$, $E_{X^+}^b$ are binding energies of excitons and positively charged trions, n_i are carrier densities per unit area, $C_i = \hbar \sqrt{\frac{2\pi}{m_i k_B T}}$ are thermal wavelengths and m_i are effective masses of ($i = e, h, X^0, X^+$) electrons, holes, excitons, and trions, respectively as in Ref. 134.

Most importantly, assuming constant pre-factors to the exponential term in equations 4.17 and 4.18, we note that $\exp(-2) \approx 0.135$, $\exp(-1) \approx 0.368$, $\exp(-0.5) \approx 0.607$ when the all-important ratio $\left(\frac{E_i^b}{k_B T}\right)$ varies from 2 to 1 to 0.5, respectively. This clearly shows that even when the binding energy E_i^b is less than the thermal fluctuation energy ($k_B T$), there still can be a finite, *non-zero* probability of having some bound states of excitons or trions. It is remarkable to discover that photocapacitance spectroscopy is still sensitive to these very small numbers of excitons or trions. As such, we already know that binding energy can also change under applied bias and can also thereby affect the above populations. However, such changes can be quite small (see figure 5(b) of reference 31). Therefore, based on the above

numerical estimates, unless the ratio $\left(\frac{E^b_i}{k_B T}\right)$ varies hugely, it need not affect the final population significantly.

From figure 4.13, it is quite visible that peak photocapacitance value of two peaks also evolves with the bias. In figure 4.16(b), we show that peak intensity ratio of the peaks IX^+ and IX^0 varies slowly at the beginning. It then changes significantly with increasing applied electric fields. The ratio remains near unity in the low bias side, indicating an equal contribution from both excitons and trions. However, with increasing biases, trions start to dominate the photocapacitance spectra. This is because positive trions formation is always more energetically favourable compared to the excitons. As a result, the peak photocapacitance ratio of trions and excitons is shown to vary with the applied field, implying the formation of trions at the expense of excitons with the increase of electric field in the reverse bias regime. We tried to fit the above variation with a modified Arrhenius rate (R^*) equation following our earlier work⁸

$$R^* \approx \frac{1}{\tau} = v^* \exp\left(-\frac{E_a}{k_B} \eta V_{dc}\right) \quad (4.19)$$

where η is a proportionality factor in units of $V^{-1}K^{-1}$ to ensure correct dimensionality and E_a is activation energy for transitions activated by bias voltage V_{dc} , v^* is the thermal pre-factor representing the heat bath, τ is the time period of the transition and k_B is the Boltzmann constant. The experimental data on peak photocapacitance ratio in figure 4.16(b) fits well with such bias activated model. The ratio drastically increases around the reverse bias of -0.8 V.

III. Differences in spectra at a fixed bias and with respect to temperature

Photocapacitance and photo- G/ω spectra at 200 Hz are compared with DC-photocurrent spectra for -0.6 V bias at 100 K as shown in figure 4.17(a). Spectral splitting is only observed in photocapacitance spectra whereas we don't see any spectral splitting in photocurrent and photo- G/ω . Also, there is a slight shift in peak energy position observed among these. Such differences were also observed at room temperature and were attributed to dissociation of direct excitons which are not closer to the AIAs potential barrier. We know that photocapacitance arises mainly from the bias driven accumulated charge carriers near the AIAs barrier, whereas

the DC-photocurrent is solely affected by the charge carriers driven out of the junction. However, contributions to photo- G/ω can come from both these regions. Moreover, one can notice that the spectral broadening in the photocurrent spectra is reasonably higher than the photo- G/ω and photocapacitance at -0.6 V. All these certainly imply that the origin of DC-photocurrent spectra is different. The measured photocurrent is likely to originate from the dissociation of excitonic²³ photo absorptions, which are mostly forming away from the junction³¹. This will be further elaborated in the next section.

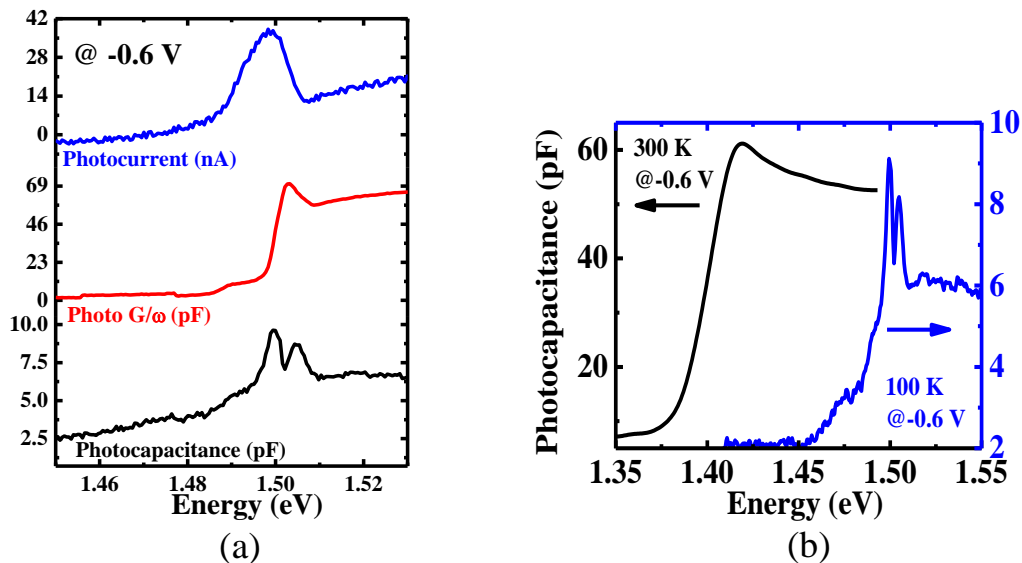


Figure 4.17: (a) DC-photocurrent spectra are compared with photocapacitance and photo- G/ω spectra (at frequency 200 Hz) at a fixed bias -0.6 V. We don't see any spectral splitting in the photocurrent and photo- G/ω spectra at 100 K. (b) Photocapacitance spectral signature is plotted for 300 K and 100 K at a fixed applied voltage of -0.6 V. Temperature-dependent spectral behaviour is differentiated.

In figure 4.17(b), we show the drastic changes in the photocapacitance spectral shape and the peak energy with the temperature variation from room temperature to 100 K. We compare these two spectra for a particular applied bias of -0.6 V. Here, we observe that the single excitonic peak at room temperature drastically changes to narrower double peaks of both excitons and trions at 100 K. This clearly indicates that such peak splitting occurs only at low temperature. Blueshift of the spectral peak energies with decreasing temperature can be explained from the usual band gap expansion.

IV. Why photocapacitance spectra are superior over photoluminescence spectra in detecting such indirect excitonic complexes

Mostly, PL spectra were used in the past to understand the intricate details of many-body carrier dynamics of trions and FES. However, in our experimental results, we find photocapacitance is more informative in comparison to PL study in this type of barrier structure. To recognize the difference, in figure 4.18(a), we plot the PL spectra at 100 K for different applied biases. The spectral broadening, i.e., full width at half maxima (FWHM), is certainly more than that of usual intrinsic FWHM of any excitonic PL at low temperature. However, unlike photocapacitance spectra, we do not observe spectral splitting and any spectral shift in the PL spectra under increasing reverse biases.

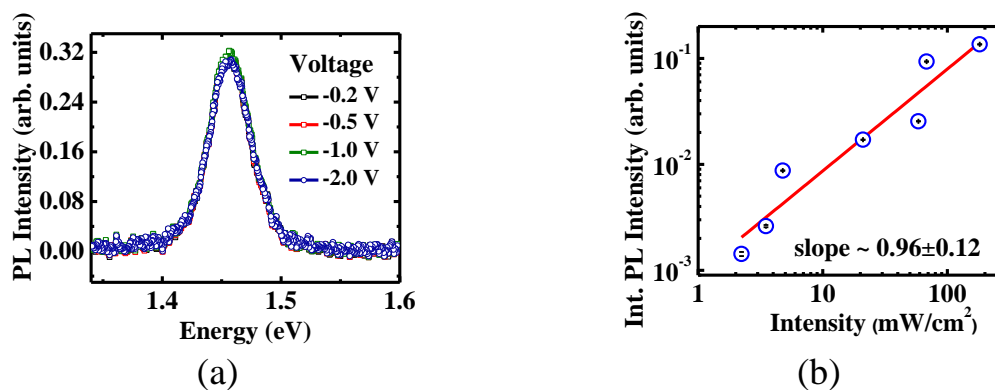


Figure 4.18: (a) Bias dependent PL measurement is carried out at 100 K. We hardly observe any bias dependence in the spectral features. (b) Integrated PL intensity versus intensity follows a power-law trend with an exponent value ~ 0.96 . This value corresponds to the presence of direct excitons, which are forming away from the AlAs junction.

Also, this PL spectral peak energy is expectedly at a lower energy in comparison to the photocapacitance spectral peak. This indicates two different physical origins for PL and photocapacitance spectra. Integrated PL intensity versus optical excitation intensity also follows a linear variation in log-log scale which gives a slope of ~ 0.96 at 100 K indicating the presence of excitons as shown in figure 4.18(b). It is expected that neutral, indirect excitons (IX^0 s) and positively charged, indirect trions (IX^+ s) around the AlAs barrier hardly contribute to PL due to the lack of spatial overlap of their respective electron and hole wave functions. Therefore, the observed PL is mainly due to the presence of excitons, which are photoexcited far away from the AlAs junction and then, radiatively recombine. As a result, PL spectra are

hardly affected by the applied bias. However, the indirect excitons, trions (IX^+), FES forming near the heterojunction are strongly influenced by the applied bias as shown in figures 4.13, 4.14(a) and 4.14(b). As a result, such bias induced changes in carrier accumulations around the GaAs/AlAs/GaAs heterojunction can be sensed by phot capacitance.

As such absorption and emission spectroscopies are based on two different mechanisms where carrier dynamics and detection techniques are different. In fact, this difference is the exact reason why PL was not able to respond to applied bias and could not probe the all-important indirect excitons at 100 K even with more intense photoexcitation. This is because electron-hole pairs generated throughout the top GaAs also contribute significantly to PL. As reported previously for indirect excitons, the phot capacitance spectroscopy is now shown to be also sensitive to bias induced dipolar changes of indirect trions, FES formed across the AlAs barrier. It is this enhanced selectivity of phot capacitance spectroscopy to these spatially indirect dipoles of excitonic many-body systems like trions and FES which needed to be emphasized here. So, we want to point out that phot capacitance spectroscopy is a superior technique in detecting these delicate indirect excitons, trions, and FES in comparison with conventional PL spectroscopy.

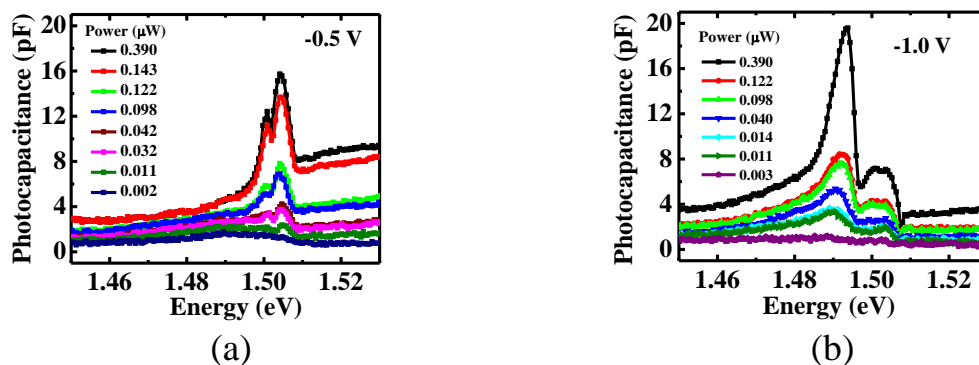


Figure 4.19: (a) and (b) Excitation intensity-dependent phot capacitance spectra for two different applied voltages -0.5 V and -1.0 V, respectively. The two biases correspond to two different spectral behaviours. At -0.5 V, the excitons and trions peaks are dominant whereas at -1.0 V, FES and excitons presence are visible. Optical excitation above the energy bandgap always creates an equal number of electrons and holes, and more intensity generates more carriers. However, it is the applied bias which selectively pushes electrons and holes into their respective TQWs and allows them to form excitons like bound states.

In addition, we want to state that optical intensity dependence of phot capacitance spectra is also studied for fixed biases at 100 K, as shown in figures 4.19(a) and 4.19(b). Spectral peak splitting and shapes are observed to be hardly affected by the variation of the optical excitation intensity over the range of 2 to 50 $\mu\text{W}/\text{cm}^2$. Increase of the optical excitation intensity only enhances the magnitude of the overall phot capacitance. Interestingly, it is the applied bias, which plays a more crucial role to inject the optically generated carriers to respective TQWs to form excitonic complexes. Therefore, we now confirmatively claim that the formations of these spatially indirect trions and FES in this GaAs/AlAs/GaAs heterostructure can be predominantly controlled by the applied reverse bias and not so much by the optical excitation intensity.

4.7.3 Summary of part B

In a nutshell, phot capacitance spectroscopy was used to detect the formation of spatially indirect, bias driven, dipoles of excitons as well as positively charged trions around the AlAs barrier in GaAs/AlAs/GaAs p-i-n heterostructure even at 100 K. Bias dependent spectral peak splitting of exciton and trions is also demonstrated. Moreover, in the higher density limit $\geq 1 \times 10^{11} \text{ cm}^{-2}$, we have also identified the signatures of Fermi edge singularity from phot capacitance spectra. Contrary to popular beliefs, the presence of trions at such a high temperature of ~ 100 K in these III-V materials is explained using the Saha's ionization equation. This analysis indicates that there is always a small but finite thermodynamic probability of the existence of excitonic complexes having binding energy lower than the thermal bath energy ($k_B T$). Interestingly, we have shown that these small fractions of trions and excitons do respond to phot capacitance spectroscopy but not to conventional optical measurements like PL and DC-photocurrent spectra. However, it is established here that phot capacitance is a superior and sensitive experimental tool to probe and study these types of spatially indirect, many-body excitonic complexes in such single barrier p-i-n heterostructures. Such electrical detection and manipulation of excitons and trions at such high temperatures of 100 K were clearly unheard of in III-V materials. We predict that these observations provide a first concrete step towards any device-level experimental control of trions and FES at even higher temperatures. This can further lead to future applications^{39,157,158} in next-generation optoelectronics and telecommunications devices, possibly even at room temperature, using similar heterostructures made with 2D monolayers of TMDC having high

excitonic binding energies. Moreover, it is difficult to directly probe the ‘dark’ excitons’ with standard optical emission-based spectroscopies. However, these kinds of capacitive techniques, have the potential to even sense dipolar signatures of ‘dark’ excitons, which constitute the true ground state of any excitonic BEC. Such indirect excitons in TMDC heterostructure are also predicted^{159,160} to display excitonic superconductivity, electro-optical spectral control of trion lasing¹⁶¹ and optical modulation¹⁶² of ‘dipolar’ excitons. Therefore, our studies on frequency-dependent dynamic signatures of dipolar nature of excitons and trions can provide significant impetus to explore simple photocapacitive spectral control of excitons, trions, and FES for future applications.

4.8 Temperature and bias dependent behaviour of photocapacitance

In this section, we want to provide more experimental results which are not fully analysed yet and thus, not published in any journal so far. We wish to keep these unpublished results here by realizing that it might be helpful to clarify the queries which may arise in readers’ mind as well as for future use. These are the experimental results measured on the same sample in different temperature regime. In figure 4.20(a), we have plotted the photocapacitance spectra for different applied reverse biases at 10 K. The spectral peak position matches well with the GaAs energy bandgap at 10 K. Photocapacitance peak magnitude enhances as the applied reverse biases are increased. It is understandable that as the reverse bias is increased, corresponding more electrons and holes come close towards each other across the AIAs barrier and thus, form more excitons. More abundance of excitons creates more dipoles. Hence, we observe higher signal in photocapacitance measurement. However, we do not see any peak splitting and other signatures here as observed around 100 K temperature. Similarly, we measured photocurrent spectra in figure 4.20(b). Photocurrent spectra also show a nice sharp peak near GaAs energy band edge and always increase as the reverse bias is raised. Although, the microscopic analysis of this spectral signature is not clearly envisioned until now. In figure 4.20(c), the photocapacitance spectral variation with the temperature is plotted for a fixed reverse bias of -1.0 V. Here, we see the spectral evolution from 10 K to 300 K. Beside peak energy shift with the temperature, we also notice the spectral shape change and energy splitting in the spectra.

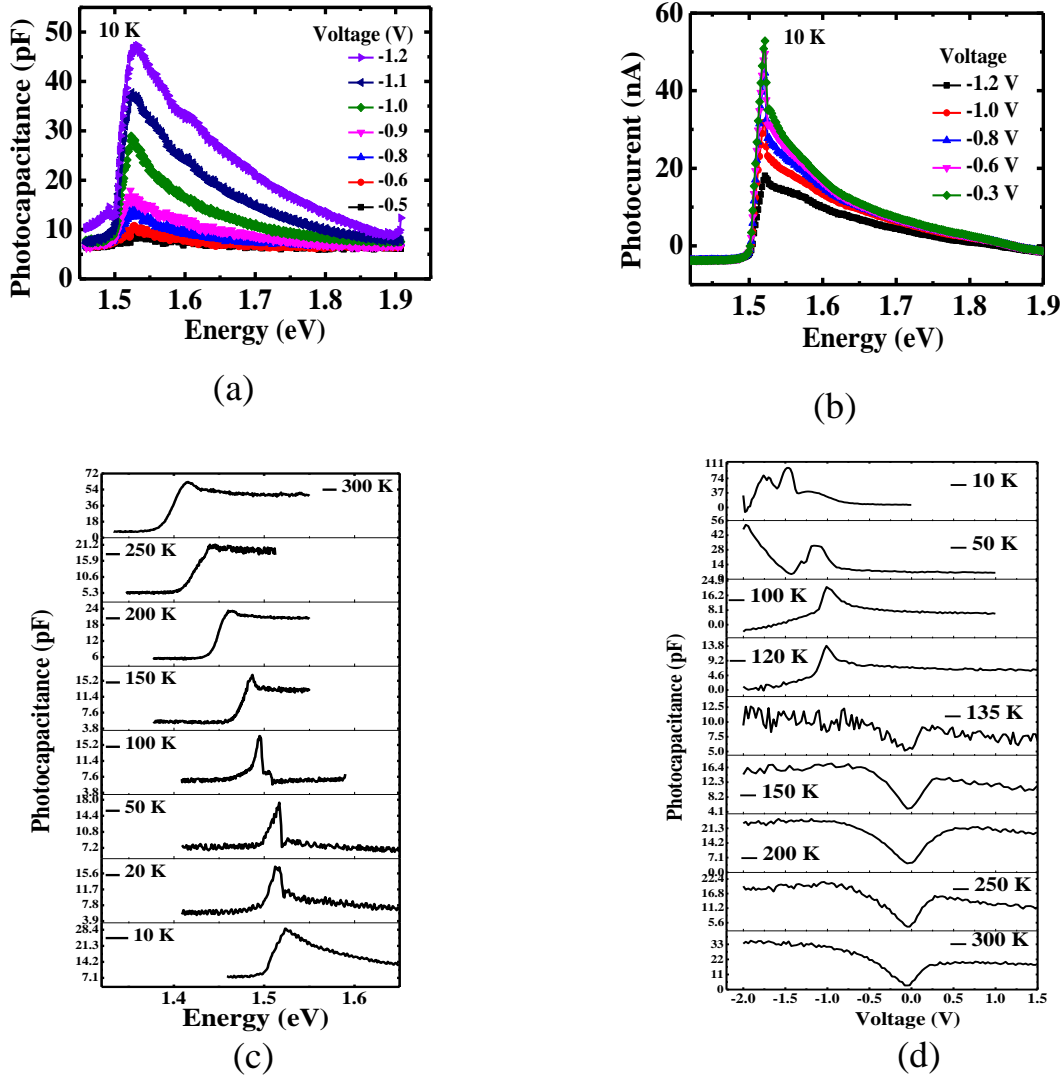


Figure 4.20: (a) photocapacitance spectra is measured at 200 Hz frequency modulation at 10 K. Photocapacitance signal increases as the applied reverse bias is increased. (b) Similarly, photocurrent spectral behaviour is plotted for different applied reverse biases at 10 K. (c) Photocapacitance spectra measured at fixed bias -1.0 V is plotted for different temperature ranging from 300 K to 10 K. (d) Photocapacitance versus voltage is plotted for different temperature values. Comparing (c) and (d), we observe that spectral anomaly started after 150 K also has an impact on the photocapacitance versus voltage measurement as the dip converts into peak after 135 K. However, the physical origin of these observation is still not clearly comprehended by us and further studies require to realize these opto-electrical measurements in this single barrier sample.

We find these spectral behaviours as highly dependent on the measurement temperature. Photocapacitance versus voltage plot shows an interesting feature as shown in figure 4.20(d).

We observe a dip near 0.0 V in the photocapacitance measurement in the higher temperature regime 300 K to 135 K. However, it completely changes after 135 K temperature. Around 120 K and below temperature, the dip in the photocapacitance plot becomes a peak and shift towards reverse voltage ~ -1.0 V. The underlying physics behind these interesting features are not yet understood properly and it certainly needs more analysis and experimental data before asserting any definitive claims.

Chapter 5

Photo-induced oscillations in dielectric measurement: involvement of excitons and quantum capacitance

5.1 Introduction

Transport properties of carriers inside low-dimensional semiconductor heterostructures have very enriching physics and applications. Quantum mechanics mostly play significant roles to explain the carrier dynamics in these low-dimensional heterostructures. There are many published books¹⁶³⁻¹⁶⁷ on quantum transport in low-dimensional structures which explain details theoretical and experimental aspects, might be helpful to readers. Tunnelling is one such kind of phenomenon which can only be realized from the concept of quantum mechanics. Moreover, tunnelling in semiconductor heterostructure is well-understood carrier transport mechanism. Accordingly, there are two types of tunnelling processes which eventually contribute to two tunnel diodes: normal tunnel diode and resonant tunnelling diode. Normal tunnel diode was first invented by L. Esaki in 1958; hence, this is sometimes called Esaki diode. This is a highly doped semiconductor p-n junction diode. Due to this high doping concentrations, the depletion layer width of the p-n junction remains very narrow in the order of 10 nm or less¹⁰.

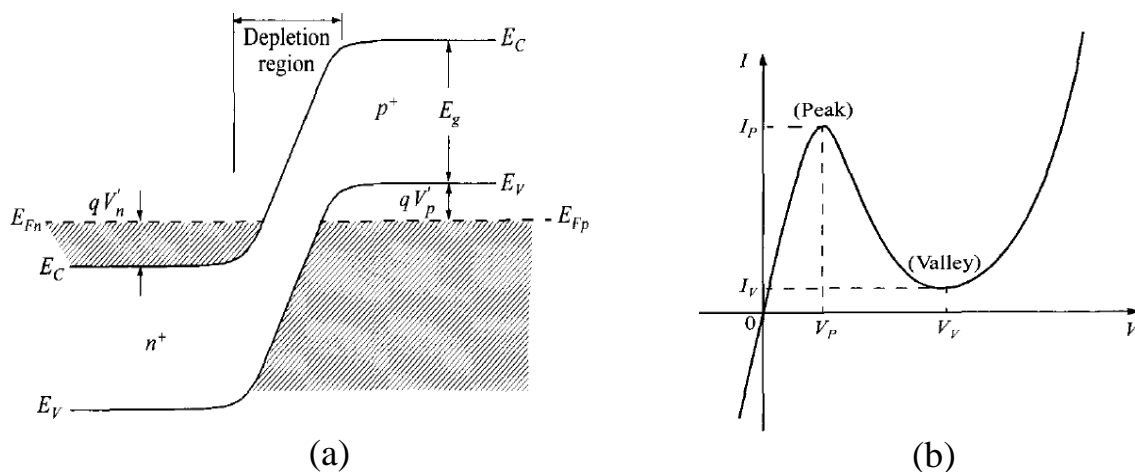


Figure 5.1: (a) A schematic energy band diagram a normal tunnel diode. p^+ and n^+ are the highly doped carrier concentration in both the p and n-type sides of the device, respectively. V'_p and V'_n are degeneracies on the p-side and n-side, respectively. (b) An $I - V$ plot of tunnel diode which shows a negative resistance region. I_p (V_p) and I_v (V_v) are the current (voltage) values at peak and valley voltages, respectively. (taken from reference 10)

This narrow width and the degenerate valence and conduction bands facilitate the tunnelling process, as shown in figure 5.1(a). More interestingly, one observes anomalous current (I) - voltage (V) behaviour where current decreases with the increase in the applied voltage. This unique behaviour was first noticed by Esaki, and he explained this using the concept of quantum mechanical tunnelling effect. The particular region in the current-voltage plot where dI/dV shows negative slope is known as negative differential resistance. Tunnel diodes were mostly used for high-frequency oscillators, fast switching devices, etc. In figure 5.1(b), we show a schematic of the $I - V$ characteristic of a tunnel diode. The negative differential region is evident from the graph. The details physics of this interesting $I - V$ curve is explained thoroughly in reference 10.

However, we are mostly interested in the physics of resonant tunnelling diode in this chapter. Here, the tunnelling happens only when the energy levels of the two transition states match resonantly. Mostly, double barrier p-i-n or n-i-n heterostructures devices have been studied to understand the resonant tunnelling phenomenon. In the case of double barrier structure, there exists a quantum well (QW) in between two barriers. The quantized energy levels (E_n) of the QW play a vital role in the resonant tunnelling of carriers. There are as such three regions of interest in this kind of tunnelling physics: emitter region, well region or quantum-confined region and the collector regions as shown in a schematic diagram in figure 5.2.

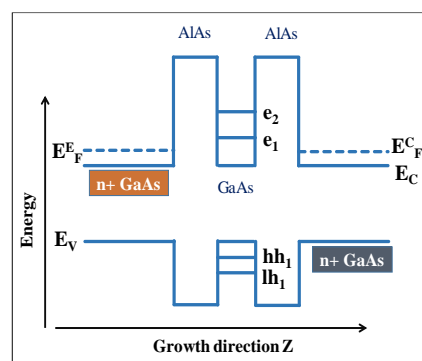


Figure 5.2: A schematic energy band diagram of double barriers resonant tunnelling diode. E_F^E and E_F^C are commonly known as the emitter and collector regions of the device. e_1, e_2 are the electron energy levels in the QW and hh_1 and lh_1 are the energy levels for heavy hole and light hole, respectively.

In general, emitter and collector regions are considered as the electrodes of the system; thus, have free carriers. The corresponding energy expression for the same is,

$$E = E_C + \frac{\hbar^2 k_z^2}{2m^*} + \frac{\hbar^2 (k_x^2 + k_y^2)}{2m^*} \quad (5.1)$$

where, E_C is the conduction band minimum, k_z is the momentum of the carrier along the z-direction (growth direction), k_x and k_y are the momentum along the x-y plane, perpendicular to growth direction, m^* is the effective mass of the carrier. The well-known energy expression for QW is as follows,

$$E_{QW} = E_n^z + \frac{\hbar^2 (k_x^2 + k_y^2)}{2m^*} \quad (5.2a)$$

$$E_n^z = \frac{\hbar^2 \pi^2 n^2}{2m^* L_z^2} \quad (5.2b)$$

here, n is the quantized energy levels, L_z and E_n^z are the width and the energy of the QW along the growth direction, respectively. It is evident from the expressions that carriers in the collector and emitter regions have three-dimensional (3D) degrees of freedom. Whereas, carriers inside the quantum well have 2D degrees of freedom. So, this transition of carriers through the QW region is actually an example of 3D versus 2D energy levels matching in case of resonant tunnelling process.

As mentioned above, resonant tunnelling happens when the energy of the incoming particles matches resonantly with energy of the transition state. During this transition, overall energy and momentum of the carrier mostly remain as a conserved quantity. Hence, one should consider the continuous momentum distribution of the carrier in the x-y plane on top of the quantized energy levels (E_n^z) inside the QW. Detailed analysis of such carrier transport and the consideration of momentum distributions are elaborated in chapter 8 of reference 10. So, we are not going to explain similar physics here again.

Most interestingly, researchers have observed multiple peaks in current versus voltage measurement in this kind of heterostructure instead of a single peak in case of normal tunnel diode (see figure 34 in chapter 8 of reference 10). Due to the presence of more than one quantized energy levels inside the QW, multiple peaks appear when the value of each energy level resonantly matches with the energy of the incoming particles. However, in our experimental results, we will discuss the underlying physics of multiple peaks in capacitance and current in more details and also from a different perspective. In addition, we would like to

mention here that there are two types of resonant tunnelling process; one is known as coherent tunnelling and the other one is sequential tunnelling. In case of coherent tunnelling, the phase of the particles is maintained, i.e. the phase of the incoming particles is the same as that of the transmitted particles after tunnelling through the barriers.^{168,169} When the carriers traverse the tunnelling regions, there are many possible scattering mechanisms like elastic scattering, inelastic scattering which control the phase of the particles. Such phase-coherent tunnelling¹⁷⁰ is only possible if and only if the carriers go through elastic scatterings where the energy of the carriers remain conserved. This kind of phase coherence also can be maintained if the transport happens in the ballistic regime, i.e. without any scattering. However, these kind of theoretical predictions are very difficult to achieve and rarely encountered in real heterostructures as the interface roughness, trap states, defect centers, etc. actively contribute to dissipative scattering mechanisms. Whereas, in case of sequential tunnelling, incoming particles first tunnel from the emitter to the well and then from the well to the collector and the transmitted particles hardly have any phase correlation with the incoming ones. Sequential tunnelling faces multiple scattering during the process, thus phase information is naturally lost in this mechanism. Hence, the transmission peaks or the peaks in the current measurements should be sharper in case of coherent tunnelling whereas, one observes broadened peaks in case of sequential tunnelling due to multiple scattering events¹⁰.

In this chapter, we are mostly involved in exploring the physics of resonant tunnelling in coupled 0D-2D system. We observe interesting quantum oscillations in electrical measurements when a single layer of InAs quantum dot (QD) embedded in GaAs/AlAs/GaAs p-i-n diode is optically excited at 10 K temperature. The observed peaks and valleys in the photocapacitance oscillations are found to be more informative and insightful to probe the interface dynamics of electrons, holes and excitons. We find distinct, periodic, and well-spaced photocapacitance peaks in the reverse bias. The peak amplitude gradually decreases as the reverse bias is increased. However, the photocapacitance peak values are higher, and the peaks are more closely spaced in the small forward bias side. Similarly, we have observed nice, clear-cut oscillation in photocurrent and photoconductance versus voltage measurement also. In addition, to understand the precise nature of this oscillation, we have measured the photocapacitance spectra for different peak and valley voltages. Two sharp, discrete, resonant peaks in photocapacitance spectra at the crest voltages certainly imply the involvement of excitons in these oscillation physics. Formation of triangular quantum well (TQW) across the GaAs/AlAs interface and the presence of InAs QD layer have made it possible to form the

excitons easily. Furthermore, the existence of TQWs allows for 2D electron or hole gases (2DEG or 2DHG) in their respective wells. Formation of this 2DEG or 2DHG under optical excitation and applied bias also modify the effective junction capacitance measured across the intrinsic regions of the device. Change in effective capacitance with respect to dark geometrical capacitance is apprehended as a series contribution of another capacitance, which is known as quantum capacitance. This quantum capacitance again found to be mathematically interconnected to the excitons present in the system which we will describe shortly. Strikingly, the estimated exciton Bohr radius from the experimentally obtained quantum capacitance value matches well with our device configuration. This interpretation of excitons from the quantum capacitance point of view is somewhat new, and we claim it experimentally for the first time.

As such semiconductor p-i-n heterostructure devices having zero-dimensional quantum dot (QD) layer within the intrinsic region were explored well in the past. This particular heterostructure is potentially very rich to probe the novel quantum dynamics of carriers like resonant tunnelling, Coulomb blockade, charging of individual quantum state, exciton dynamics, single-charge fluctuations at the interface,¹⁷¹ etc. QD heterostructure system is also very well-known for single-photon sources¹⁷², quantum information technology, etc. In the recent past, researchers have experimentally observed peaks in the photocapacitance and photocurrent versus voltage study in a similar 0D heterostructures. Observed peaks in photocapacitance versus voltage plot have been explained as the charging of QD's S and P states¹⁷³ and correlations of exciton complexes by Labud et al.²⁸ and Pal et al.²⁹. Recently, Vdovin et al. have shown^{154, 174, 175} interesting quantum oscillations in the photocurrent versus voltage measurement in a sample with an InAs QD layer embedded inside an AlAs single barrier structure. They have observed oscillation in photocapacitance measurement also, but the physics of the same remain unexplored. In our experimental study, we thoroughly probe the physics of these oscillations using photocapacitance and try to correlate the same with the involvement of excitons and quantum capacitance.

5.2 Sample and measurement details

The sample used for our experimental measurements has one InAs quantum dots layer within single barrier GaAs/AlAs/GaAs p-i-n diode. This particular sample structure has a similar configuration as one of the samples measured by Vdovin et.al¹⁵⁴. It was grown by Molecular Beam Epitaxy (MBE) on a highly doped n⁺ GaAs substrate. The following layers

are grown subsequently on the substrate: a 1.0 μm heavily doped ($4 \times 10^{18} \text{ cm}^{-3}$) n^+ GaAs layer is grown at temperature 550 $^\circ\text{C}$ on top of the substrate for bottom contact, subsequently a 100 – nm n doped ($2 \times 10^{16} \text{ cm}^{-3}$) GaAs layer, and then 100 – nm undoped spacer layer of GaAs, two intrinsic AlAs layers of thickness 5.1 nm each having a 1.8 monolayer of InAs quantum dots layer in between them, then a 60 nm thick undoped GaAs layer complete the intrinsic region, after that a 0.51 - μm heavily doped ($2 \times 10^{18} \text{ cm}^{-3}$) p^+ GaAs layer which serves as top contact for the device. Circular ring shaped mesas having outer diameter 200 μm is used for top electrical contact having an optical window for photocapacitance measurements. The area of the gold contact pads is approximately $3 \times 10^{-4} \text{ cm}^2$. A sketch of the sample structure is drawn in figure 5.3 for better visualization.

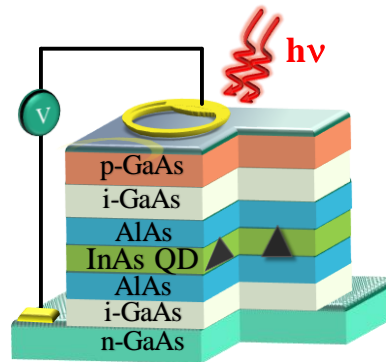


Figure 5.3: A multi-layered p-i-n heterostructure device is drawn schematically to provide an overview of the device under study.

For low-temperature measurements, we place our sample on a copper holder inside of a closed-cycle cryostat CS-204S-DMX-20 from Advanced Research Systems. The temperature of the cryostat is controlled with a Lakeshore (Model-340) temperature controller. For photocapacitance measurement ($C_{photo} = dQ/dV$), the sample is illuminated from the top p-GaAs side using an Acton Research SP2555 monochromator having a 0.5-m focal length along with a 1000-W quartz-tungsten-halogen lamp. For photocapacitance measurements, we used Agilent's E4980A LCR meter with small signal rms ac voltage of 30 mV with the frequency 10 kHz (unless mentioned otherwise). A simple series equivalent circuit of capacitance (C) and conductance (G) in parallel was used to extract these parameters. The spectral response of the lamp-monochromator combination is reasonably smooth and changes slowly and monotonically within the wavelength ranges we use in our experiments.

5.3 Results and discussion

5.3.1 Photocapacitance oscillations and their correspondence to excitons

In this section, we will address some intriguing experimental results and will try to analyze the essential physics behind that. We have used a single barrier GaAs/AlAs/GaAs p-i-n heterostructure diode where the InAs QD layer is grown on AlAs layer. Besides, we notice that this kind of heterostructures are sensitive to optical excitation. Hence, most of the exciting experimental observations have been realized only in the presence of light. In figure 5.4(a), photocapacitance oscillations are plotted with respect to the applied reverse voltage at 10 K. Here, we measure this particular photocapacitance signal using an electrical modulation frequency 10 kHz and under a fixed photoexcitation wavelength ~ 630 nm having a constant power ~ 190 μ W at the sample position. Periodic and distinct oscillations peaks are very much evident in figure 5.4(a) and the magnitude of these peaks decreases as the reverse bias is increased. More prominent and closely spaced peaks are identified for small forward biases shown in the inset of figure 5.4(a).

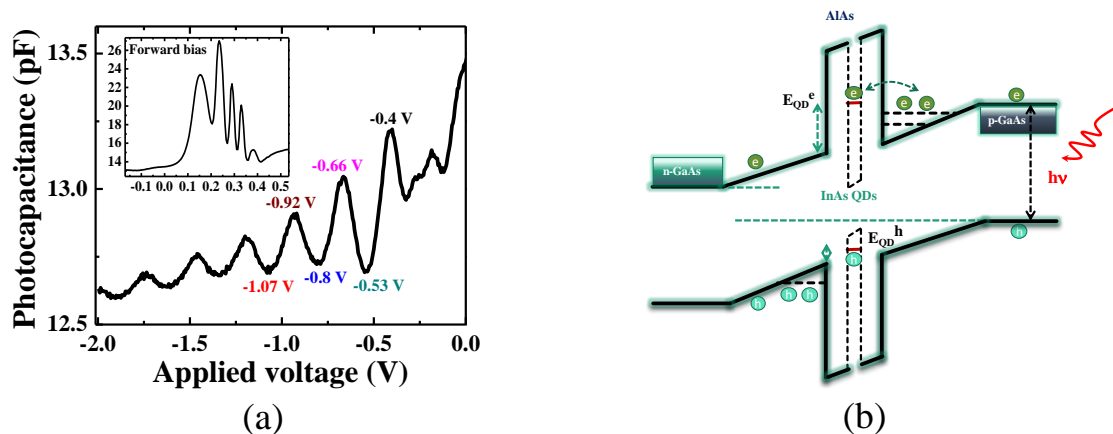


Figure 5.4: (a) A periodic, distinct oscillation in the photocapacitance measurement is plotted for applied reverse bias. The initials few prominent peaks and valleys are marked with corresponding voltage values for the ease of identification. The inset shows much stronger oscillation amplitude and closely spaced peaks under the small forward-bias application. (b) An energy band diagram of the p-i-n device is drawn to understand the motion of charge carriers near the intrinsic region.

A schematic energy band diagram (figure 5.4(b)) of this p-i-n device is depicted for reverse bias under photoexcitation. This standard diagram is based on past claims and

observation^{154,174,175} of such single barrier structures. Also, formation of GaAs TQW on both side of the AlAs barriers and the energy levels of electron (E_{QD}^e) and holes (E_{QD}^h) of InAs quantum dot is clearly visible in the diagram. The formation of GaAs TQWs across the AlAs barrier makes it easier to form 2DEG and 2DHG when the sample is excited with light of appropriate wavelength and bias is applied to the device. In reverse bias, we can have 2DEG in the p-side and 2DHG in the n-side TQW of the device. Now, the questions we raise what is the physics of this oscillation in the photocapacitance versus voltage plot? Do we expect any excitonic state to be present in this structure as this replicates our previously studied sample but having an extra InAs QD layer here? Does exciton play any significant role in these quantum oscillations? At this point, we further speculate that there should be an involvement of energy levels of TQW and the energy levels of InAs QD to explain this nice oscillation in photocapacitance. Now, it is well known that these energy levels of TQWs are explicitly voltage-dependent and can be altered by externally applied bias.

To address all these speculations and ambiguities, in figure 5.5(a), we measured the photocapacitance spectra for initial few peak voltages (where the signal strength is comparatively higher) as marked in figure 5.4(a). Interestingly, we observed two sharp, resonant optical absorption peaks in the photocapacitance spectra, which certainly have an excitonic origin. These two peaks also consistently evolve with the applied bias. Whereas, the photocapacitance spectra measured at different valley voltages do not show sharp, systematic spectral signature like those measured under peak oscillation voltages. These were shown in figure 5.5(b). So, we have identified a crucial distinction between these two spectral signatures measured at peak voltages ($P_1=-0.4$ V, $P_2=-0.66$ V, $P_3=-0.92$ V) and the valley voltages ($V_1=-0.53$ V, $V_2=-0.8$ V, $V_3=-1.07$ V), shown in figures 5.5(a) and 5.5(b), respectively. It is also quite evident from the figures 5.5(a) and 5.5(b) that excitonic presence is prominent when the spectra were taken at peak oscillation voltages. Whereas, in the valley voltages, we do not see such sharp excitonic signatures. So, at this point, we apparently claim that presence of excitons directly contributes to peaks in the photocapacitance oscillations. So, when these excitons vanish from the photocapacitance spectra or dissociate, we observe valleys in the photocapacitance oscillations. Now, we will explore a more detailed microscopic understanding of these excitons and their origin. Therefore, hereafter, we will mostly try to understand the spectral features measured at peak oscillation voltages as shown in figure 5.5(a). Initially, we find that the transition energy for the low energy peak ~ 1.520 eV at peak voltage -0.4 V (say).

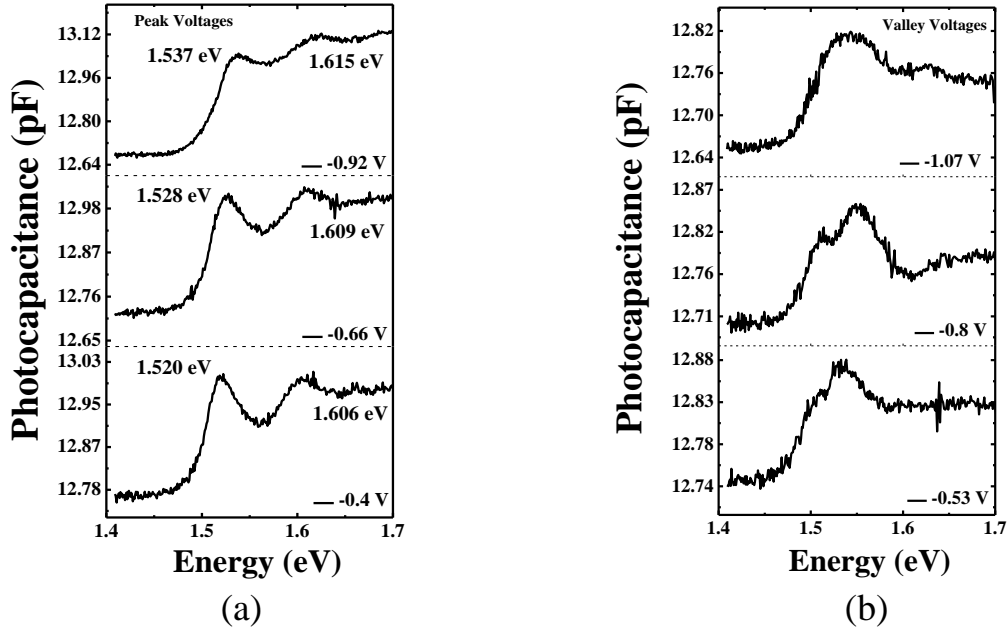


Figure 5.5: (a) Two sharp, distinct, resonant peaks have been observed in the photocapacitance spectra for peak voltages -0.4 V, -0.66 V and -0.92 V. We identify these peaks as due to excitonic presence in the system. We also notice a clear-cut blue shift in peak energies with the biases. (b) Similar photocapacitance spectra have been plotted for valley voltages -0.53 V, -0.8 V and -1.07 V. However, here we do not see such sharp excitonic peak features like those observed under peak oscillation voltages.

This transition energy value matches well with the standard GaAs excitonic energy gap at 10 K. So, we assign this low energy peak in the photocapacitance spectra as GaAs peak. Moreover, the higher energy peak value ~ 1.606 eV at -0.4 V has the possible source of origin from InAs QD layer. As per previous studies^{176,177}, InAs QDs grown on the AlAs layer have a much higher effective energy gap as compared to the same grown on the GaAs layer. Besides, photoluminescence (PL) study also yields QD peak signature in the higher energy side in InAs/AlAs QD sample at 10 K temperature^{178,179}. Hence, we ascribe this higher energy peak at -0.4 V as due to the lowest energy transition in InAs QDs. However, we would like to point out here that these InAs QDs grown on AlAs do not have any wetting layer¹⁸⁰. Hence, we do not expect any contributions in the spectral response due to wetting layer. So, two peaks in the photocapacitance spectra at -0.4 V are attributed as GaAs exciton peak and the InAs QD exciton peak, just because, the energy value of the peak transition matches well with the known energy gap of the consisted layers. Now, to realize the formation of these excitons in this heterostructure system, we look into the energy band diagram of the sample in figure 5.4(b).

We excite the sample with a light of energy ~ 1.968 eV (~ 630 nm) from the top p-type side and simultaneously apply reverse voltage to the p-i-n device. Accordingly, we populate both the QD energy levels (E_{QD}^e and E_{QD}^h) and TQWs with the electrons and holes. As per the configuration of the heterostructure, we have electron accumulations in the p-side TQW and hole accumulations in the n-side TQW (shown in figure 5.4(b)) under reverse bias condition. These two opposite charged particles separated by few nm distances are attracted by Coulomb force and form indirect excitons. These are indirect as the electrons and holes are spatially separated by extra layers (AlAs, InAs). However, there are other possibilities of indirect exciton formation between InAs QD layer and GaAs TQWs in this particular structure. Like, holes in E_{QD}^h can be attracted to electrons in GaAs TQW to form indirect exciton or electron in E_{QD}^e can bind with holes in GaAs TQW in the opposite side to form indirect excitons. Although these probable mechanisms of indirect exciton formation are there, presently we do not find any substantial evidence to differentiate between various scenarios of formation of indirect excitons. Whereas, the electrons and holes which are generated in the QD layer, they form the direct excitons. It is important to note that although the lifetime of these direct excitons is very less \sim few ps, but there will be always a finite population of excitons as we are exciting the sample by a continuous light source. Moreover, optical energy of the light is much higher than the available energy bandgaps of the sample. Hence, presence of both direct and indirect excitons population can be sensed simultaneously under small frequency modulation (10 kHz) and reverse bias. Also, we have drawn the QD hole energy level (E_{QD}^h) below the valence band maximum of GaAs following the previous report¹⁷⁴, in the schematic energy band diagram. Here, we would like to mention that although E_{QD}^h is shown to be the lowest energy state for holes in figure 5.4 (b), still holes from the GaAs TQW are not expected to occupy E_{QD}^h through tunnelling due to following reasons. Firstly, E_{QD}^h energy state mostly remains filled with the holes which are excited in the QD layer itself due to continuous excitation. Secondly, holes effective mass is quite large, and mobility is less in comparison to electrons which effectively reduces the probability of tunnelling by order of magnitude³¹. Henceforth, we reiterate that the holes hardly contribute to any tunnelling mechanism and remain in the same layer where these are created. However, the electrons play a crucial role in resonant tunnelling and quantum oscillation, which we will analyze in the next few paragraphs.

Besides, we observe a significant blue shift in the low energy spectral peak with the peak voltages in comparison to higher energy peak in figure 5.5(a). To grasp the physics behind this blue shift, we necessitate knowing the evolution of electron energy levels in the TQW with

the applied electric field. From the standard textbook understanding of quantum mechanics, one can solve the Schrodinger equation and get the approximate nth energy expression for GaAs TQW for electrons,

$$E_n \propto \left[\frac{3\pi}{2} \left(n - \frac{1}{4} \right) \right]^{2/3} \left[\frac{(F_z e \hbar)^2}{2m^*} \right]^{1/3} \quad (5.3)$$

where E_n is the nth energy level of the TQW and the potential of the GaAs TQW is $V(z) = eF_z z$, \hbar is the reduced Planck constant, F_z is an electric field across the intrinsic region in the growth direction z , m^* is the effective mass of electrons in GaAs. It is quite evident from the energy expression in equation 5.3 that the energy levels of TQW are explicitly dependent on the electric field and the energy levels blue shift with the electric field. Such variation will be negligible for InAs QD levels due to its smaller width along the growth direction, and also the energy levels have hardly any explicit field dependence. However, in table 5.1, we calculate the values of these energy levels for electrons considering an effective mass $m^* \sim 0.067m_0$ of GaAs, for different peak voltages. Here, m_0 is the free electron mass.

Table 5.1: Energy levels of electron in TQW for different peak voltages.

Peak Voltage (V)	Electric Field ($\times 10^6$ V/m)	Energy level (n=1) (meV)	Energy level (n=2) (meV)	Energy level (n=3) (meV)	Energy difference ($\Delta n=2-1$) (meV)	Energy difference ($\Delta n=3-2$) (meV)
P ₁ = -0.4	11.09	95.4	167.7	226.7	72	59
P ₂ = -0.66	12.616	103.9	182.7	247	79	64
P ₃ = -0.92	14.135	112	197	266.3	85	69

Here, we estimate the energy values for the initial three quantized energy states ($n= 1, 2, 3$). We find that energy levels spacing decreases with higher values of ‘n’ and increases with the electric field. We also notice that the estimated energy level spacing (between $n=2$ and $n=1$) are in similar magnitude with the spectral peak energy differences in figure 5.5(a) and as shown in table 5.2. However, the theoretical calculation of energy difference between $n=1$ and $n=2$ always increases with the electric field as shown in table 5.1, whereas experimental results do not follow this particular trend, mentioned in table 5.2. Hence, we deliberately nullify any

involvement of higher energy states except $n=1$, to explain the spectral behaviour in figure 5.5(a) and its correlation with the oscillation in figure 5.4(a).

Table 5.2: Energy difference between two peaks in the spectra taken for peak voltages:

Peak Voltage (V)	Direct exciton (QD) peak energy (eV)	Indirect exciton (GaAs) peak energy (eV)	Difference in peak energy (meV)
$P_1 = -0.4$	1.605	1.521	84
$P_2 = -0.66$	1.607	1.528	79
$P_3 = -0.92$	1.621	1.537	84

Furthermore, we have compared the field-dependent energy level separation for ground state ($n=1$) of TQW and low-energy spectral peak shifts in both the theoretical and experimental regime, respectively and tabulated these values in table 5.3 for a better connection. We observe a striking match between experimental and theoretical estimations. We find that energy level difference of indirect exciton peak measured between two successive peak voltages in the oscillation data matches quite well with the theoretical estimation of $n=1$ energy level difference for electrons in TQW for two peak voltages. This particular result certainly convinced us that only the involvement of $n=1$ energy level could explain the spectral blue shift in the low energy indirect exciton peak with the applied reverse bias. So, it can now be simply interpreted, as the electric field increases, $n=1$ level goes up, and the optical transition due to indirect excitons absorption happen in the higher energy values. Thus, we observe a blue shift in the indirect excitons peak in photocapacitance spectra. However, any change in hole energy levels of TQW due to the applied electric field is negligibly small due to the large effective mass of holes. So far, we have realized that there is a presence of both direct and indirect excitons in peak voltages of the oscillation. Indirect exciton peak significantly blue shifts with the applied electric field and can be explained by considering the evolution of $n=1$ energy level of the electron in the TQW. Now, we would like to explain how the presence of excitons correlate with the observed oscillation in the photocapacitance versus voltage in figure 5.4(a). It is well-known that as we increase the electric field the corresponding energy level of the TQW goes up and when it matches resonantly with another energy level nearby then resonant tunnelling occurs. In this context, we have a QD electron energy level (E_{QD}^e) sitting in the higher energy state, as shown in the schematic diagram in figure 5.4(b). Hence, $n=1$ energy

level of the electron in the TQW rises with the electric field and make a resonant transition once the energy matches with the E_{QD}^e , then electrons from the TQW go away.

Table 5.3: Theoretical and experimental comparison of energy shift for successive peak voltages:

Peak voltage (V)	TQW energy level (n=1) (meV)	Indirect exciton peak energy from spectra (meV)	TQW Energy level difference for successive peak voltages (meV)	Change in exciton peak energy for successive peak voltages (meV)
$P_1 = -0.4$	94.8	1520	8.4 (for P_2, P_1)	8 (for P_2, P_1)
$P_2 = -0.66$	103.2	1528	8.2 (for P_3, P_2)	9 (for P_3, P_2)
$P_3 = -0.92$	111.4	1537	16.6 (for P_3, P_1)	17 (for P_3, P_1)

Thus, the indirect excitons also vanish, and we should not see a sharp excitonic peak in the spectra, as we do not observe excitonic peaks in the valley voltages. So, when the indirect excitons are there in the system, there prevails a dipolar environment which enhances the measured capacitance, and as the excitons dissociate at valley voltages, we observe dips in the oscillation. Now, this particular process should produce a single oscillation peak, as the $n=1$ level already has contributed to resonant tunnelling, but we see multiple peaks in the oscillation. So, there is a catch which we want to mention here to understand multiple oscillation peaks. As mentioned earlier, the accumulated charges in TQWs also create an electric field which plays a significant role to alter the effective electric field at the intrinsic region. Once the resonant energy level matching happens, then the accumulated charges tunnel out from the TQWs, and the effective electric field across the intrinsic region diminishes. As a result, the $n=1$ energy level of the TQW goes down to lower energy values (but does not reach to, from where it started) with respect to E_{QD}^e and again start filling with the carriers. Similar, process of resonant tunnelling through E_{QD}^e and again filling up with photogenerated carriers go on and contribute to multiple peaks in the oscillation. However, the oscillation almost dies down when the TQW ground energy level ($n=1$) reach adjacent to the E_{QD}^e under high reverse bias as observed in figure 5.4(a). So, in a nutshell, we had seen interesting quantum oscillations in the photocapacitance under reverse biases which we have interpreted as the involvement of excitons in the resonant tunnelling process. Also, the evolution of ground energy level ($n=1$)

of TQW for an electron with the electric field and the existence of QD energy level E_{QD}^e facilitate to have resonant tunnelling process which effectively contributes to oscillations.

Additionally, here the resonant tunnelling happens between these 2D and 0D coupled system. Now, QDs have complete discrete energy levels in all three spatial dimensions whereas the 2D TQWs have discrete energy levels only in the growth direction (z-axis) and other two spatial dimensions have a continuous distribution of energy. During resonant tunnelling, the total energy of the system should be taken care of. The details understanding of the particular type of resonant tunnelling (sequential or coherent) need more analysis, which is beyond the scope of the present study.

Moreover, we observe a strong oscillation amplitude in the lower reverse bias, whereas in the higher reverse side, the amplitude of oscillations goes down (figure 5.4(a)). The possible reasoning may be that in the higher reverse bias or higher electric field values, the lowest energy level $n=1$ of the TQW reside at the possible top-level and almost merge with QD energy level. Hence, due to swallow confinement and merging of energy with QD energy values, excitonic features eventually start vanishing. So, in lower field regime oscillations are very dominant due to the strong presence of excitons, in the higher field regime, the oscillation dies down due to dissociation of excitons. In addition, the base photocapacitance or dark capacitance (below bandgap excitation) is also changing with the bias from 12.77 to 12.66 pF (change of ~ 110 fF) over the bias values -0.4 V to -1.07 V. Now, as the reverse bias increases the corresponding depletion width also increases which eventually decrease the capacitance as $C = \frac{\epsilon A}{d}$. Important to mention here that all these changes of capacitance under photoexcitation is very small \sim few hundreds of fF and these change is only possible to observe when the current flowing in the circuit remains very small \sim few nano Amperes.

5.3.2 Origin of quantum capacitance and its correspondence to excitons

Capacitance usually means geometrical capacitance with which we are most familiar. Sometimes, this is also called electrostatic capacitance as the derivation of the same is based on electrostatic equations. Geometrical capacitance is a bulk phenomenon and depends upon the dielectric constant of the medium, shape, area of the capacitor plates, etc. However, quantum capacitance has an entirely different origin and mainly important for low-dimensional quantum heterostructure. Presence of 2DEG in quantum-confined heterostructure modifies the

effective capacitance of the system. Contribution of this extra capacitance cannot be explained from the standard electrostatic depletion capacitance type models. This additional capacitance has a substantial contribution from quantum mechanics and the density of states of the low-dimensional system. The term quantum capacitance was firstly coined by Serge Luryi around 1988¹⁸¹. In a GaAs/AlGaAs QW system, he clearly demonstrated how the presence of 2DEG inside the QW alters the total capacitance by a series combination with the geometric capacitance of the device. After that, there are numerous reports on quantum capacitance; both theoretical and experimental studies are published in peer-reviewed journals^{173,182-186}. Most of the nanoelectronics devices are based on this quantum capacitance. Quantum capacitance finds application in understanding the microscopic details of low-dimensional devices, high-frequency devices, etc.

However, in this context, we are motivated to correlate the quantum capacitance with the excitons in this QD embedded single barrier p-i-n heterostructure. In our case, the formation of indirect excitons involves 2DEG and 2DHG in TQWs. And again quantum capacitance becomes essential due to the presence of 2D and 0D systems. Now, the quantum capacitance for a 2D system has the following expression,

$$C_q = \rho e^2 = \frac{m_* e^2}{\pi \hbar^2} \quad (5.4)$$

where ρ is the two-dimensional density of states, C_q is quantum capacitance per unit area, m_* is the effective mass of carrier, e is an electronic charge, \hbar is the reduced Planck's constant. The above expression for quantum capacitance can be rearranged and written in terms of exciton Bohr radius accordingly,¹⁶⁴

$$C_q = \frac{m_* e^2}{\pi \hbar^2} = \frac{\epsilon}{a_0^*/4} \quad (5.5)$$

where $a_0^* \equiv \frac{4\pi\epsilon\hbar^2}{m_* e^2} = (0.053 \text{ nm}) \frac{m_0}{m_*} \frac{\epsilon}{\epsilon_0}$, a_0^* is the exciton Bohr radius, ϵ is the dielectric constant of the medium, ϵ_0 is the dielectric constant of free space. Now, this expression in equation 5.5 looks similar to well-known formula for geometrical capacitance where the distance between two highly conducting plates is one-fourth of the excitonic Bohr radius. Hence, we can simply draw an analogy between quantum capacitance and classical capacitance by comparing the separation between the plates. When the separation appears in the order of excitonic Bohr radius, i.e., an order of a few nm, then it is termed as quantum capacitance whereas the distance in the micro-meter range or more implies the classical capacitance.

Usually, the value of quantum capacitance is much higher than the classical counterpart. Here, we will experimentally estimate the value of this quantum capacitance and then, aim to evaluate the value of exciton Bohr radius. For a series configuration of geometric capacitance (C_g) and quantum capacitance, one can write effective capacitance (C_{eff}) as

$$\frac{1}{C_{eff}} = \frac{1}{C_g} + \frac{1}{C_q} \quad (5.6a)$$

$$\frac{1}{13} = \frac{1}{12.8} + \frac{1}{C_q} \Rightarrow |C_q| = 832 \text{ pF}. \quad (5.6b)$$

This is an approximate value of $|C_q|$ which is estimated from photocapacitance spectra at a fixed bias. Quantum capacitance can be negative or positive depending upon the experimental conditions which help to form the 2DEG or 2DHG inside the QWs. Here, in the absence of light and under small applied bias, we did not have 2D carrier accumulation. Thus, the capacitance of the device was determined by geometric capacitance. However, in the presence of light and applied reverse bias, 2DEG and 2DHG form inside the TQWs, and thus, there is an increment of effective capacitance with respect to dark geometric capacitance. Henceforth, we will deal with the absolute value of the quantum capacitance only.

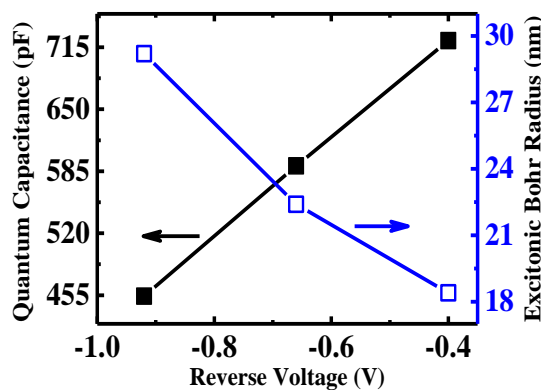


Figure 5.6: We have plotted the magnitude of quantum capacitance and corresponding excitonic Bohr radius for three peak voltages. This shows magnitude of quantum capacitance decreases whereas the excitonic Bohr radius increases as the applied reverse bias increases.

Moreover, using the above-modified expression of quantum capacitance and the experimentally calculated value of $|C_q| \sim 832$ pF, we estimate the value of excitonic Bohr radius as ~ 16 nm. In figure 5.6, we plotted the values of quantum capacitance and corresponding values of excitonic Bohr radius with respect to the peak voltages in the reverse bias. These

values are estimated based on the magnitude of the indirect exciton peak in the three spectral data in figure 5.5(a). Importantly, we find that these values of exciton Bohr radius are crucial for this device as these match more or less with the separation of 2DEG and 2DHG layer in the intrinsic region. Hereafter, we claim that the significance of quantum capacitance is directly related to the excitonic presence in the system, and we experimentally first demonstrate this correlation. So, in a nutshell, we summarize that photocapacitance oscillation with respect to applied reverse bias (figure 5.4(a)) is directly influenced by the presence of excitons and involvement of quantum capacitance in this 0D-2D p-i-n resonant tunnel diode structure. Observations and possible explanations so far presented and discussed are not published yet, and the manuscript is currently under preparation stage only. More analysis and experimental measurement need to be carried out to fully understand the complete dynamics of carriers in this kind of complex 0D-2D interface of semiconductor heterostructure. In the next section, we provide some additional results, which are not yet adequately analyzed and may also require theoretical calculations, simulation to fully grasp the underlying physics.

5.3.3 Further analysis and results to understand the physics of oscillation

In the last few decades, mesoscopic physics of semiconductor nanoelectronics devices has evolved a lot, but researchers still lack complete knowledge of the carrier dynamics of a multi-layered semiconductor quantum heterostructure devices. It is also realized that the presence of many interfaces of semiconductor hetero layers makes the quantum devices too complicated to understand the underlying physical mechanism. In this case, our sample is also consisted of many layers having an InAs QD layer and GaAs TQWs in both sides of the AlAs potential barriers. So, a complete understanding of the observed experimental features requires more analyses and results.

Until now, we have only explained the physics of oscillation and spectral features in the reverse bias side. However, in the small forward bias regime (less than the built-in voltage ~ 1.5 V), we have observed more prominent and closely spaced oscillation, which we have not explained yet, as shown in the inset of figure 5.5(a). To realize this interesting oscillation, we measured the excitation wavelength-dependent oscillation in this particular voltage range as plotted in figure 5.7(a). It is evident from figure 5.7(a) that as the optical excitation energy comes down below the energy bandgap of the constituent materials, the corresponding

oscillation vanishes. This implies that the observed oscillation is highly sensitive to optical excitation. We also notice that with the excitation wavelength, the oscillation peak voltages

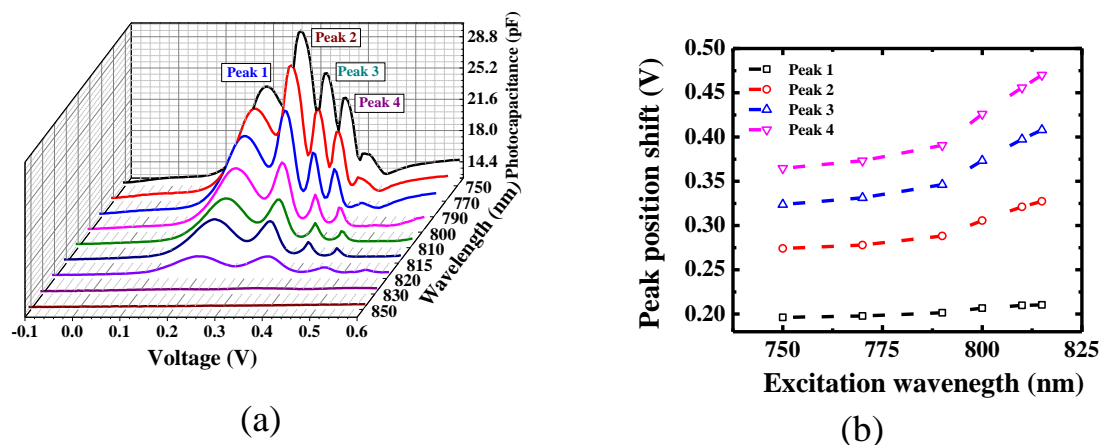


Figure 5.7: (a) We have plotted photocapacitance oscillations with different excitation wavelengths for low forward bias. Depending upon excitation energies, the peak amplitude and positions also vary. (b) The estimated peak shift with the excitation wavelengths is plotted to understand the wavelength dependency.

also shift towards higher voltages, as shown in figure 5.7(b). At this point, we speculate that this closely spaced oscillation may have originated from the closely spaced hole energy levels in TQW due to a higher value of hole effective mass (equation 5.3). It has been inferred that maybe the change of applied bias polarity has allowed the photogenerated holes to dominate the dielectric measurement. Additionally, we also observe exciting photocapacitance spectral signature in the forward bias regime. In figure 5.8(a) and 5.8(b), we plot two photocapacitance spectral results for 0.326 V and 0.6 V, respectively. We have chosen these two specific positive voltages as the 0.326 V locates one peak position in the oscillation regime (0.0 V to 0.5 V) whereas the 0.6 V lies beyond the oscillation regime. It is important to note that we see nice excitonic peak features when the spectra are taken in the oscillation regime but there is no trace of excitonic presence as the spectra is measured beyond the 0.5 V. Another way to represent this study is that presence of excitons in the system highly contribute to nice oscillation in the photocapacitance versus voltage measurement but in the absence of the same, we do not see any oscillation.

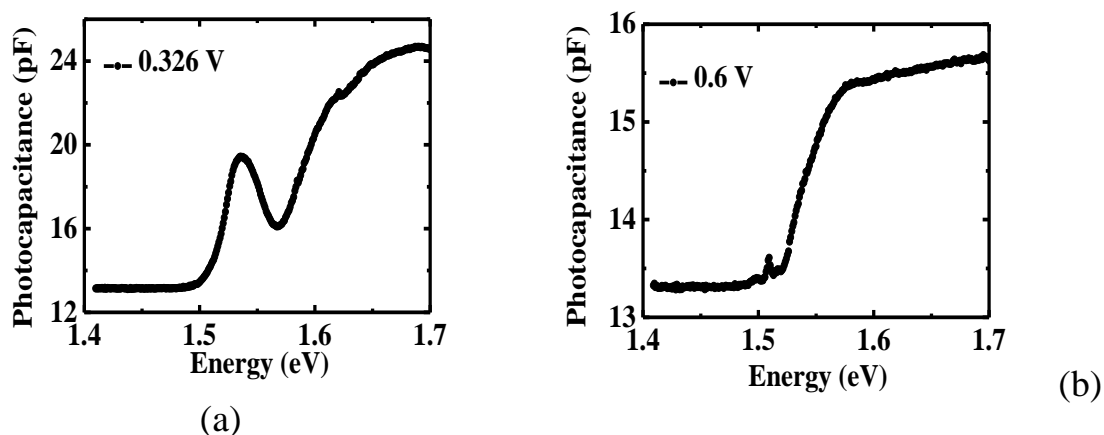


Figure 5.8: (a) and (b) Photocapacitance spectra measured at two different forward bias values; 0.326 V and 0.6 V, respectively. We observe a prominent excitonic peak at 0.326 V whereas we do not see clear excitonic peak at 0.6 V. However, we have seen earlier (figure 5.7(a)) that the small forward voltage oscillation vanishes after 0.5 V. So, these observations apparently suggest that the presence of excitons are somehow related to the observed oscillation in the photocapacitance versus voltage measurement.

Besides, we also observed very systematic, periodic oscillation in the photocurrent and photo- G/ω with respect to the applied voltage. In figure 5.9(a), we have compared both the oscillation. It is visible from the plot that photocurrent oscillation peaks are voltage-phase shifted to the photo- G/ω peaks. However, we find that photocapacitance and photo- G/ω peaks exactly coincide with each other, as shown in figure 5.9(b). The fundamental reasons behind this drastic disparity in the oscillation behaviour are yet to unfold, and the analysis is under progress. Moreover, we find the photo- G/ω peaks are lying in the slope of the photocurrent oscillation data. Now, a derivative of this photocurrent data with respect to voltage (dI/dV) exactly reproduce the photo- G/ω as plotted in figure 5.9(c). Also, it is quite evident from the photocurrent oscillation that the appearance of multiple peaks in the $I - V$ certainly represent the multiple negative differential region (NDR). Usually, in a normal tunnel diode, we have single negative differential region whereas the presence of many NDR in a single device may be helpful in future to make complex high-frequency oscillators, multiple logic, and memory-based devices¹⁰, etc.

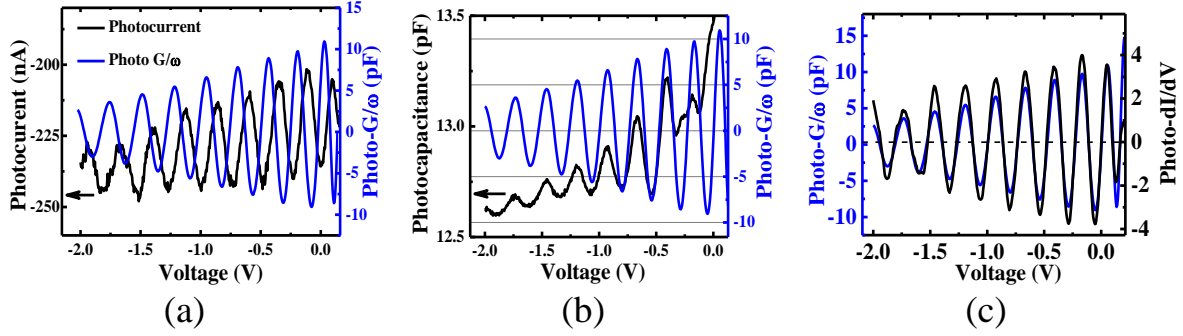


Figure 5.9: (a) We compare the oscillation of photocurrent and photo- G/ω for reverse bias side. The peak positions are voltage shifted to each other. (b) However, Photocapacitance and photo- G/ω fall exactly in line with each other. (c) The derivative of photocurrent with respect to voltage dI/dV replicate the photo- G/ω , implies that these are connected and have a similar origin.

5.4 Conclusions

In summary, we have observed systematic, prominent, periodic and reproducible oscillation in the electrical measurement, when an InAs QD inserted single barrier GaAs/AlAs quantum heterostructure p-i-n device is optically excited at 10 K. Multiple peaks in the oscillation are realized due to resonant tunnelling in between QD energy levels and TQWs energy levels. We further measured the photocapacitance spectra for different peaks and valley voltages. Importantly, we notice sharp excitonic peaks in the spectra, taken at peak oscillation voltages whereas we hardly see clear excitonic feature in the valley voltages. This investigation implies that the involvement of excitons plays crucial roles for the oscillation in photocapacitance. The blue shift of low energy indirect exciton peak is explained due to the involvement of mostly $n=1$ electron energy level of TQW. Moreover, for the first time, we experimentally demonstrate the correlation between quantum capacitance and excitons. Estimated excitonic Bohr radius matches well with the sizes of indirect excitons within our device. Therefore, throughout this chapter, we aimed to explain the microscopic physics behind the interesting photo-induced quantum oscillation in this GaAs/AlAs/InAs complex p-i-n heterostructure device. At this stage, we hope that we are able to give the readers a brief microscopic overview of the underlying carrier dynamics in this quantum heterostructure. This work is now under thorough investigation and manuscript is in the preparation stage. Further experimental results and analysis require to comprehend the complete internal carrier movement.

Chapter 6

Summary and future directions

6.1 Conclusions

In summary, we want to mention that studying the condensed matter physics of excitons and its experimental signatures are itself a vast and really diverse set of topics of research problems. There are different types of excitons and a large variety of excitonic complexes which are possible to form in semiconductor-based quantum heterostructures. Moreover, scattering of excitons with a variety of phonons, defect states, crystal potentials inside materials and quantum structures make the physics of excitons even more intriguing. Also, the lack of precise experimental signatures which can differentiate different types of excitons under the presence of light and electric field need rigorous understanding and analyses. Henceforth, there was always some scopes to explore hitherto unknown physical aspects of excitons in order to gain control over excitons inside semiconductors structures. We also understand that excitons play a crucial role in optical absorption and emission processes as well as in electrical transport properties of semiconductor heterostructure. Furthermore, due to their intrinsic dipolar nature, they are expected to respond in measurements which can sense the non-trivial dielectric polarization of these dipolar excitons. Therefore, in the research work presented in this thesis, we had always aimed to explore dipolar behaviour of excitons in III-V semiconductor heterostructures devices in various temperatures and frequency domains. We have explored some interesting insights and signatures of excitons which were not addressed previously. Photocapacitance based optoelectronic approaches are established by us as a sensitive technique to detect many-body physics of indirect excitons at the heterostructure interfaces, which is not possible using standard PL technique.

Physics of spatially direct and indirect excitons have interesting dynamics and distinct features which allowed us to distinguish them based on the characteristic experimental signatures of their dielectric polarization behaviours. Normally, researchers generate a mixed population of indirect excitons by dissociating some of these direct excitons inside coupled quantum wells (CQWs) using high electric fields. Instead of CQWs, here we have created indirect excitons in single barrier heterostructure devices by photoexcitation and applied electric field. Therefore, we find this method of generating long-lived, indirect excitons much easier where the generic features of these indirect excitons remain intact due to the presence of a large potential barrier preventing them from recombining. However, indirect excitons are

important mainly due to their longer radiative lifetimes. Such long lifetimes may eventually help these indirect excitons to reach thermal equilibrium and thus allow phase transitions like excitonic Bose-Einstein condensations (BEC) and excitonic superconductivity, etc. Henceforth, we have extensively studied the physics of indirect excitons and demonstrated our unique approach to detect and investigate experimental signatures of these dipolar indirect excitons.

It was also understood and reported previously, that inside quantum heterostructures, binding energy of excitonic states enhance due to strong quantum confinement effects. However, with the help of our sensitive experimental techniques to sense the overall dipolar polarization of excitonic dipoles, we have established that even a small fraction of excitons present in any system can be explicitly identified. Therefore, we were able to clearly establish that excitons can survive even at higher temperatures where the thermal energy is way more than the Coulombic binding energy of these excitonic states. Earlier, photocapacitance technique was used mainly to probe the sub-bandgap defect states, trap states of semiconductors. Whereas, there were only a few reports on detecting excitons using photocapacitance spectroscopy. However, we have clearly demonstrated and explained how photocapacitance spectroscopy could be used to detect the presence of excitons and excitonic complexes. Moreover, we have also estimated the dipole moments and polarizabilities of these excitonic dipoles from the shift of spectral peak energy with applied bias.

In our first work, we intended to find a new dielectric signature of excitons in quantum confined laser structures at room temperature. Accordingly, we have established a novel electrical technique to identify the presence of excitons in GaInP/AlGaInP MQW and MBE grown InGaAs/GaAs QD laser diodes. Differential capacitance (fdC/df) measurements with frequency under different applied forward voltages bear the signature of excitons in these quantum confined structures. Presence of excitonic dipoles at the junctions of these light-emitting diodes, certainly modify the junction capacitance depending upon applied modulation frequency. We conceived a phenomenological rate equation considering the effects of applied bias on the dynamics of various rate-limited processes. Formation of stable excitonic population inverts the usual negative Arrhenius slope to positive one which eventually appears as ‘negative activation energy’. We demonstrate that this ‘negative activation energy’ relates to the presence of transitional bound states, which was identified by us as excitons. That is because the calculated average energy of this bound transitional state matches well with the binding energy of the weakly confined excitons in these laser diodes. We emphasize that such

occurrence of ‘negative activation energy’ was not observed in ordinary Silicon diodes which do not emit light as electroluminescence and perhaps are non-excitonic in nature. Further increase in charge injection suppresses the differential capacitive response, which shows a gradual Mott transition of exciton states into electron-hole plasma in GaInP/AlGaInP MQW. This all-electrical, steady-state description of excitonic presence and its subsequent suppression is fully supported by standard optical spectroscopic signatures of excitonic Mott transition. We speculate that this work may lead to innovative applications based on efficient electrical modulation and control of excitonic light emitting devices. Further studies are required to make concrete applications and also to fully comprehend various analytical details of dipolar contributions of excitons through such dielectric polarization measurements using capacitive methods.

We have also studied photocapacitance signature of bias driven, inverted dipoles of 2D indirect excitons formed across 8 nm thin AlAs tunnel barrier in Γ bands of GaAs/AlAs/GaAs heterostructure. We have argued that quantum confinements of photo-generated electrons and holes in triangular 2DEG and 2DHG structures enhance both the excitonic binding energy and the thermodynamic probability of these indirect excitons to survive even at room temperature. We have also analyzed characteristic differences in the electric field dependence of excitonic features in both photocapacitance and DC-photocurrent spectra. In particular, we have shown that large, tunable dipole moment along the growth direction can be engineered to selectively probe, control, and manipulate the indirect excitons by photocapacitance using applied bias and modulation frequency. Moreover, peak photocapacitance signal follows a reasonable upper limit of areal density of photo-generated indirect excitons. Remarkably, we could demonstrate that the photocapacitance technique which was rarely used in the past to detect excitons can be used to identify indirect excitons.

Furthermore, we have used photocapacitance spectroscopy to detect the formation of spatially indirect, bias driven, dipoles of excitons as well as positively charged trions around the AlAs barrier in GaAs/AlAs/GaAs p-i-n heterostructure even at 100 K. Bias dependent spectral peak splitting of exciton and trions was also demonstrated. We also want to emphasize here that physics of these excitons and excitonic complexes are highly dependent on applied bias and happen mostly under photoexcitation. Additionally, in the higher density limit $\geq 1 \times 10^{11} \text{ cm}^{-2}$, we have also identified the signatures of Fermi edge singularity and trions from photocapacitance spectra. Contrary to popular beliefs, the presence of trions at such a high temperature of ~ 100 K in these III-V materials is explained using the Saha’s ionization

equation. This analysis indicates that there is always a small but finite thermodynamic probability of the existence of excitonic complexes having binding energy lower than the thermal bath energy ($k_B T$). Interestingly, we have shown that these small fractions of trions and excitons do respond to phot capacitance spectroscopy but not to conventional optical measurements like PL and DC-photocurrent spectra. Until now, researchers mostly used PL to study these excitons, trions, and FES in a variety of materials. Our work also explains why and how phot capacitance spectroscopy can efficiently probe these interacting dipoles of trions and FES, which ordinary luminescence spectroscopy fails to do so.

Such electrical detection and manipulation of excitons and trions at such high enough temperature of 100 K were clearly unheard of in III-V materials. We predict this work opens up the possibility of experimental detection of indirect excitons and trions using phot capacitance in materials with higher excitonic binding energies. This may provide a first concrete step towards any device-level experimental control of these excitonic complexes at higher temperatures. Significant differences between excitonic signatures of phot capacitance and photocurrent spectroscopies may also be used to address either indirect or direct excitons. This can further lead to future applications in next-generation optoelectronics, telecommunications, and excitonic devices, possibly even at room temperature, using similar heterostructures made with 2D monolayers of TMDC having high excitonic binding energies. Moreover, it is always difficult to directly probe the ‘dark excitons’ with standard optical emission-based spectroscopies. However, these kinds of capacitive techniques have the potential even to sense dipolar signatures of ‘dark’ excitons, which constitute the true ground state of any excitonic BEC in III-V semiconductors. Such indirect excitons in TMDC heterostructure are also predicted to display excitonic superconductivity, electro-optical spectral control of trion based lasing and optical modulation of ‘dipolar’ excitons. Therefore, our studies on frequency-dependent dipolar signatures of excitons, trions, and FES can provide significant impetus to explore simple phot capacitance spectral control of these excitonic complexes for future applications.

Finally, we have also probed indirect excitons in coupled 0D-2D quantum structure where InAs QD were inserted inside single barrier GaAs/AlAs p-i-n quantum heterostructure and measured at 10 K. A prominent, periodic and reproducible quantum oscillation in the electrical measurement were observed when the sample is optically excited. Multiple peaks in the oscillation are realized due to resonant tunnelling between QD energy levels and TQWs energy levels. Phot capacitance oscillation with the applied reverse bias, was found more

informative about excitons as compared to photocurrent and photo- G/ω . We further measured the phot capacitance spectra for different peaks and valley voltages. Importantly, we have noticed sharp excitonic features in the spectra, taken at peak oscillation voltages whereas we hardly have seen sharper excitonic features in the valley voltages. This observation certainly established that the involvements of excitons are crucial for observing such coherent oscillations. The blue shift of low energy indirect exciton peak was explained due to the involvement of $n=1$ electron energy level of TQW. Moreover, we experimentally demonstrated the correlation between quantum capacitance and excitons for the first time. The estimated excitonic Bohr radius from the quantum capacitance results fit well with our device dimensions.

Moreover, one may apply a similar analysis to investigate the presence of condensed excitonic phases at low temperatures and other rate-limited transitions involving any bound states/quasiparticles in various materials/device structures intended for advanced functionality including ‘excitonics’. Specifically, there is increasing consensus about the role of dark excitons, in connection with still ‘elusive’, concrete experimental signature of excitonic BEC. It has been realized that standard optical tools, which indirectly, study such excitonic condensations by looking only at photons coming out once excitonic quasi-particles decay, might actually overlook the BEC altogether. At this point, we speculate that our dielectric experiments dealing with frequency-dependent dynamic signatures of dipolar excitons will be able to throw more light in that direction as these tools will also be sensitive to the presence of the dark excitons

Therefore, throughout this thesis, we have tried to probe and explain interesting physics of excitonic complexes in p-i-n quantum heterostructure. Frequency and voltage-dependent dielectric measurements were carried out to trace the novel signature of direct excitons in quantum confined laser structures. We were able to establish that phot capacitance is a superior and sensitive experimental tool to investigate these types of spatially indirect, many-body excitonic complexes in such single barrier p-i-n heterostructures. At this stage, we hope that we were able to provide the readers with a brief outlook on how to study the vast and still unexplored condensed matter physics of excitons in these quantum heterostructures. Although, we understand that further experimental results and analyses will be required to comprehend some of the recent observations.

6.2 Future plans

Importance of excitons has been utilized in various fields of research in the last few decades: from basic physics studies to semiconductor device applications including excitonic Mott transition, excitonic Bose-Einstein Condensation (BEC), exciton-polariton laser, excitonic solar cells, low-dimensional optoelectronic devices like photodetector, LEDs, non-linear electro-optical effects of excitons, etc. Excitons usually have very low binding energy (few meV) in III-V semiconductors like GaAs, InAs, etc. As a result, till now most of the interesting physics of excitons were only observed and understood at very low temperatures around a few Kelvin or below. Although, there are few materials like copper oxides, zinc oxides, organic and inorganic lead halides perovskites and 2-dimensional transition metal dichalcogenides where excitons can have very high binding energies (~tens to hundreds of meV). However, many of these material systems still lack good quality epitaxial film growth techniques to make quantum heterostructures. Problems with material stability and difficulty in fabrication of large area, uniform quantum heterostructure devices become long-standing challenges for their applications. Whereas, epitaxial growth of good quality III-nitride semiconductor quantum heterostructures were already demonstrated in various laboratories. Also, the excitonic binding energy of these III-nitride semiconductors are sufficiently high (~tens of meV) to easily probe and explore their own excitonic physics even at room temperature.

In the near future, I plan to study quantum materials with high excitonic binding energies. Recently, worldwide researchers are concerned and involved to explore the physics of a few emergents and promising optoelectronic materials namely, III-Nitride semiconductors, transition metal di-chalcogenides (TMDC), organic-inorganic perovskite, etc. These materials have the humongous potential for next-generation optoelectronic applications. These are also interesting because of their high excitonic binding energy which allows probing important and rich excitonic physics at room temperature. At this point, I hope that studying the many-body physics of excitons in these Nitride materials using opto-electrical techniques (mainly, photocapacitance and photocurrent spectroscopy) in both frequency and voltage regime may lead to some significant experimental outputs. Moreover, we found photocapacitance spectroscopy as an efficient and sensitive tool in comparison to standard photoluminescence to probe the exciting physics of indirect excitons in III-V heterostructure devices. Therefore, I want to extend our opto-electrical approach to study the dielectric polarization of excitonic complexes in III-nitride semiconductor as well as in layered TMDC heterostructure devices.

Off late, GaN is considered as a very important optoelectronic material with potential application in power electronics and high-speed devices. Microscopic understanding of the carrier dynamics and charge distribution inside any nitride-based heterostructures is a long-standing research problem which needs to be addressed to improve the efficiency of any optoelectronic devices. There are some technical difficulties like growing of high-quality p-GaN, high activation ratio of Mg as hole carriers, diffusion of Mg during high-temperature growth, etc. remain as debatable concerns in InGaN/GaN QW light-emitting diodes (LEDs), which limit their efficiency¹⁸⁷. Moreover, these problems are hardly addressed analytically, rather dealt with by varying different growth parameters. Besides, there is a ‘green gap’ problem¹⁸⁸ in InGaN/GaN QW LEDs, which eventually restricts scientists and engineers to make more efficient white light source using combination of red, green and blue LEDs. The above-mentioned challenges of drooping efficiency are due to the lack of thorough microscopic understanding of the carriers’ transport dynamics and control of defects distribution, non-radiative centers inside the interface of these hetero layers.

We propose that understanding the microscopic physics and distribution of excitons and their optical and electrical properties, lifetimes, etc. using opto-electronic based approach will be helpful to get a better overview of defects distribution, internal carrier dynamics in these excitonic materials. Moreover, there should be also some interesting excitonic physics at the interface of polar and non-polar InGaN/GaN QWs which will be important to understand the ‘green gap’ problems in LEDs¹⁸⁸. Later on, I plan to probe single InGaN/GaN QDs. At this point, I anticipate that a single quantum dot might sustain a single electron-hole pair or a few excitons in the time scale of their lifetimes. One can optically create the electron-hole pairs with selective photoexcitation and can simultaneously detect the tiny changes in dielectric polarization behaviours using capacitive techniques. This will also allow me to probe microscopic details of QD charging and Coulomb blockade physics even at room temperature. More importantly, at this point, I foresee that a single exciton might be a source of a single photon light emitter. So, getting the confirmative experimental signatures of such single photon emitter and simultaneously able to manipulate their energy states will be a great leap towards future technological applications. Overall, all these studies will facilitate researchers to understand better details of the underlying microscopic physics of excitons and charge carriers and grow high-quality quantum heterostructure devices using either III-nitride materials or 2D TMDC materials for next-generation optoelectronics applications.

References:

-
- ¹ T. Ihn, *Semiconductor Nanostructures: Quantum States and Electronic Transport* (Oxford University Press, New York, USA, 2010)
 - ² I. Singh Bhatia, A. Raman and N. Lal, *IJARCCCE*, **2**, 11 (2013).
 - ³ J. F. Muth, J. H. Lee, I. K. Shmagin, R. M. Kolbas, H. C. Casey, B. P. Keller, U. K. Mishra, and S. P. DenBaars, *Appl. Phys. Lett.* **71**, 2572 (1997).
 - ⁴ A. Miyata, A. Mitioglu, P. Plochocka, O. Portugall, J. Tse-WeiWang, S. D. Stranks, H. J. Snaith and R. J. Nicholas, *Nat. Phys.* **11**, 582 (2015).
 - ⁵ L. Protesescu, S. Yakunin, M. I. Bodnarchuk, F. Krieg, R. Caputo, C. H. Hendon, R. Xi Yang, A. Walsh, and M. V. Kovalenko, *Nano Lett.* **15**, 3692, (2015).
 - ⁶ G. Wang, A. Chernikov, M. M. Glazov, T. F. Heinz, X. Marie, T. Amand, and B. Urbaszek, *Rev. Mod. Phys.* **90**, 021001 (2018).
 - ⁷ T. Mueller and E. Malic, *NPJ 2D Mater. Appl.* **2**, 29 (2018).
 - ⁸ A. Bhunia, K. Bansal, M. Henini, M. S. Alshammari, and S. Datta, *J. Appl. Phys.* **120**, 144304 (2016).
 - ⁹ P. Y. Yu and M. Cardona, *Fundamentals of Semiconductors: Physics and Materials Properties* (Springer, 4th Edition, 2010).
 - ¹⁰ S. M. Sze and K. K. Ng, *Physics of Semiconductor Devices* (Wiley-Inter science, 3rd Edition, 2006).
 - ¹¹ J. Singh, *Physics of Semiconductors and their Heterostructures* (McGraw- Hill Inc., USA, 1992).
 - ¹² Y. P. Varshni, *Physica*, **34**, 149–154 (1967).
 - ¹³ W. Shockley, *Electrons and Holes in Semiconductors with Application to Transistor Electronics* (D. Van Nostrand Company, 1950).
 - ¹⁴ Z. I. Alferov, *Rev. Mod. Phys.* **73**, 767 (2001).
 - ¹⁵ Z. I. Alferov, *Semiconductors* **32**, 1 (1998).
 - ¹⁶ <https://warwick.ac.uk/fac/sci/physics/current/postgraduate/regs/mpagswarwick/ex5/bandstructure/>.
 - ¹⁷ J. H. Davies, *The Physics of Low-dimensional Semiconductors: An Introduction* (Cambridge University Press, 1997).
 - ¹⁸ <https://courses.cit.cornell.edu/ece407/Lectures/handout25.pdf>
 - ¹⁹ I. Pelant and J. Valenta, *Luminescence Spectroscopy of Semiconductors* (Oxford University Press, New York, 2012), Chap. 7.
 - ²⁰ M. Combescot, O. Betbeder-Matibet, and R. Combescot, *Phys. Rev. Lett.* **99**, 176403 (2007).
 - ²¹ M. Combescot, R. Combescot and F. Dubin, *Rep. Prog. Phys.* **80**, 066501 (2017).
 - ²² <http://web.mit.edu/course/6/6.732/www/6.732-pt2.pdf>
 - ²³ M. Fox, *Optical Properties of Solid*, 2nd edn. (Oxford University Press Inc., USA, New York, 2010).
 - ²⁴ M. Fox, *Quantum optics: An Introduction* (Oxford University Press Inc., USA, New York, 2006).
 - ²⁵ J. E. Fouquet and A. E. Siegman, *Appl. Phys. Lett.* **46**, 280 (1985).
 - ²⁶ X. Zhongying et al., *Solid State Commun.* **61**, 707 (1987).
 - ²⁷ G. T. Dang, H. Kanbe, and M. Taniwaki, *J. Appl. Phys.* **106**, 093523 (2009).
 - ²⁸ P. A. Labud, A. Ludwig, A. D. Wieck, G. Bester, and D. Reuter, *Phys. Rev. Lett.* **112**, 046803 (2014).

-
- ²⁹ S. Pal, C. Junggebauer, S. R. Valentin, P. Eickelmann, S. Scholz, A. Ludwig, and A. D. Wieck, *Phys. Rev. B* **94**, 245311 (2016).
- ³⁰ T. Yan, Z. Houzhi, Y. Fuhua, T. Pingheng, and L. Yuexia, *Semicond. Sci. Technol.* **16**, 822 (2001).
- ³¹ A. Bhunia, M. K. Singh, Y. G. Gobato, M. Henini, and S. Datta, *J. Appl. Phys.* **123**, 044305 (2018).
- ³² A. Bhunia, M. K. Singh, Y. G. Gobato, M. Henini, and S. Datta, *Phys. Rev. Appl.* **10**, 044043 (2018).
- ³³ Yu Ye, Zi JingWong, Xiufang Lu, Xingjie Ni, Hanyu Zhu, Xianhui Chen, YuanWang and Xiang Zhang, *Nature Photon.* **9**, 733–737 (2015).
- ³⁴ Wu, S. et al. *Nature* **520**, 69–72 (2015).
- ³⁵ Salehzadeh, O., Djavid, M., Tran, N. H., Shih, I. & Mi, Z, *Nano Lett.* **15**, 5302–5306 (2015).
- ³⁶ A. A. High, E. E. Novitskaya, L. V. Butov, M. Hanson and A. C. Gossard, *Science*, **321**, 229 (2008).
- ³⁷ D. Unuchek, A. Ciarrocchi, A. Avsar, K. Watanabe, T. Taniguchi and A. Kis, *Nature*, **560**, 340 (2018).
- ³⁸ H. J. Krenner, S. Stufler, M. Sabathil, E. C. Clark, P. Ester, M. Bichler, G. Abstreiter, J. J. Finley and A. Zrenner, *New J. Phys.* **7**, 184 (2005).
- ³⁹ L. V. Butov, *Superlattices Microstruct.* **108**, 2 (2017).
- ⁴⁰ K. B. Davis, M.-O. Mewes, M. R. Andrews, N. J. vanDruten, D. S. Durfee, D. M. Kurn, and W. Ketterle, *Phys. Rev. Lett.* **75**, 3969 (1995).
- ⁴¹ M. H. Anderson, J. R. Ensher, M. R. Matthews, C. E. Wieman, and E. A. Cornell, *Science*, **269**, 198 (1995)
- ⁴² L. V. Butov, A. C. Gossard, and D. S. Chemla, *Nature* **418**, 751 (2002).
- ⁴³ P. B. Littlewood, P. R. Eastham, J. M. J. Keeling, F. M. Marchetti, B. D. Simons, and M. H. Szymanska, *J. Phys.: Condens. Matter* **16**, S3597 (2004).
- ⁴⁴ L. V. Butov, C. W. Lai, A. L. Ivanov, A. Gossard, and D. S. Chemla, *Nature* **417**, 47 (2002).
- ⁴⁵ J. P. Eisenstein and A. H. MacDonald, *Nature* **432**, 691 (2004).
- ⁴⁶ A. A. High et al., *Nature* **483**, 584 (2012).
- ⁴⁷ O. Cotlet, S. Zeytinoglu, M. Sigrist, E. Demler, and A. Imamoglu, *Phys. Rev. B* **93**, 054510 (2016).
- ⁴⁸ A. Kavokin and P. Lagoudakis, *Nat. Mater.* **15**, 599 (2016).
- ⁴⁹ D. Snoke, *Phys. Status Solidi B* **238**, 389 (2003).
- ⁵⁰ Y. Mazuz-Harpaz, K. Cohen, M. Leveson, K. West, L. Pfeiffer, M. Khodas, and R. Rapaport, *Proc. Natl. Acad. Sci.* **116**, (2019).
- ⁵¹ Y. Mazuz-Harpaz, K. Cohen, R. Rapaport, *Superlattice Microstruct.* **108**, 88–97 (2017).
- ⁵² M. Beianet al., *Europhys. Lett.* **119**, 37004 (2017).
- ⁵³ V. Timofeev and D. Sanvitto, *Exciton Polaritons in Microcavities* (Springer-Verlag, Berlin Heidelberg, 2012).
- ⁵⁴ A. Kavokin, *Phys. Status Solidi B* **247**, 1898 (2010).
- ⁵⁵ J. Kasprzak et al., *Nature* **443**, 409 (2006).
- ⁵⁶ B. Deveaud, *Annu. Rev. Condens. Matter Phys.* **6**, 155 (2015).
- ⁵⁷ S. Utsunomiya, L. Tian, G. Roumpos, C. W. Lai, N. Kumada, T. Fujisawa, M. Kuwata-gonokami, A. Löffler, S. Höfling, A. Forchel and Y. Yamamoto, *Nature Phys.* **4**, 700 (2008).
- ⁵⁸ F. P. Laussy, A. V. Kavokin, and I. A. Shelykh, *Phys. Rev. Lett.* **104**, 106402 (2010).
- ⁵⁹ F. P. Laussy, T. Taylor, I. A. Shelykh, and A. V. Kavokin, *J. Nanophotonics* **6**, 064502 (2012).
- ⁶⁰ Y. Sun, P. Wen, Y. Yoon, G. Liu, M. Steger, L. N. Pfeiffer, K. West, D. W. Snoke and K. A. Nelson, *Phys. Rev. Lett.* **118**, 016602 (2017).

-
- ⁶¹ M. D. Fraser, S. Höfiling, and Y. Yamamoto, *Nat. Mater.* **15**, 1049 (2016).
- ⁶² D. Sanvitto and S. Kena-Cohen, *Nat. Mater.* **15**, 1061 (2016).
- ⁶³ D. V. Lang, *J. Appl. Phys.* **45**, 3023 (1974).
- ⁶⁴ J. T. Heath, J. D. Cohen and W. N. Shafarman, *J. Appl. Phys.* **95**, 1000 (2004).
- ⁶⁵ J. D. Jackson, *Classical Electrodynamics* (Wiley, 3rd Edition, 1998).
- ⁶⁶ D. A. B. Miller, D. V. Lang and L. C. Kimerling, *Ann. Rev. Mater. Sci.* **7**, 377 (1977).
- ⁶⁷ A. Menon and N. Sathyamurthy, *J. Phys. Chem.* **85**, 1021 (1981).
- ⁶⁸ J. R. Alvarez-Idaboy, N. Mora-Diez, and A. Vivier-Bunge, *J. Am. Chem. Soc.* **122**, 3715 (2000).
- ⁶⁹ J. L. Muench, J. Kruuv, and J. R. Lepock, *Cryobiology* **33**, 253 (1996).
- ⁷⁰ M. Mozurkewich and S. W. Benson, *J. Phys. Chem.* **88**, 6429 (1984).
- ⁷¹ D. Snoke, *Solid State Comm.* **146**, 73–77, (2008)
- ⁷² C. F. Klingshirn, *Semiconductor Optics*, 4th ed. (Springer-Verlag, Berlin, Heidelberg, 2012).
- ⁷³ N. F. Mott, *Proc. Phys. Soc. A* **62**, 416 (1949).
- ⁷⁴ N. F. Mott, *Contemp. Phys.* **14**, 401 (1973).
- ⁷⁵ P. Nozières, *Ann. Phys. Coll. C2* **20**, 417 (1995).
- ⁷⁶ V. V. Nikolaev and M. E. Portnoi, *Superlattice Microstruct.* **43**, 460–464 (2008).
- ⁷⁷ G. Manzke, D. Semkat and H. Stolz, *New J. Phys.* **14**, 095002 (2012).
- ⁷⁸ L. Kappei, J. Szczytko, F. Morier-Genoud, and B. Deveaud, *Phys. Rev. Lett.* **94**, 147403 (2005).
- ⁷⁹ G. Rossbach et al., *Phys. Rev. B* **90**, 201308R (2014).
- ⁸⁰ M. Stern, V. Garmider, V. Umansky, and I. Bar-Joseph, *Phys. Rev. Lett.* **100**, 256402 (2008).
- ⁸¹ K. Bansal and S. Datta, *J. Appl. Phys.* **110**, 114509 (2011).
- ⁸² K. Bansal, *Phys Status Solidi C* **10**, 593 (2013).
- ⁸³ K. Bansal and S. Datta, *Appl. Phys. Lett.* **102**, 053508 (2013).
- ⁸⁴ T. Walter, R. Herberholz, C. Muller, and H. W. Schock, *J. Appl. Phys.* **80**, 4411 (1996).
- ⁸⁵ P. P. Boix et al., *Appl. Phys. Lett.* **95**, 233302 (2009).
- ⁸⁶ A. Polimeni et al., *Appl. Phys. Lett.* **73**, 1415 (1998).
- ⁸⁷ K. Bansal, M. Henini, M. S. Alshammari, and S. Datta, *Appl. Phys. Lett.* **105**, 123503 (2014).
- ⁸⁸ M. D. Sturge, *Phys. Rev.* **127**, 768 (1962).
- ⁸⁹ C. T. H. F. Liedenbaum, A. Valster, A. L. G. J. Severens, and G. W't. Hooft, *Appl. Phys. Lett.* **57**, 2698 (1990).
- ⁹⁰ J. Shao, A. D'ornen, R. Winterhoff, and F. Scholz, *J. Appl. Phys.* **91**, 2553 (2002).
- ⁹¹ D. S. Chemla and D. A. B. Miller, *J. Opt. Soc. Am. B* **2**, 1155 (1985), see Fig. 6.
- ⁹² P. Dawson, G. Duggan, H. I. Ralph, and K. Woodbridge, *Phys. Rev. B* **28**, 7381 (1983).
- ⁹³ M. Noriyasu and K. Fujiwara, *Appl. Phys. Lett.* **97**, 031103 (2010).
- ⁹⁴ S.W. Koch et al., *Phys. Status Solidi B* **238**, 404 (2003).
- ⁹⁵ G. Wang et al., *Appl. Phys. Lett.* **64**, 2815 (1994).
- ⁹⁶ S. L. Tyana et al., *Solid State Commun.* **117**, 649 (2001).
- ⁹⁷ Ioffe Institute's Online Electronic Archive, New Semiconductor Materials (NSM), Available at:
<http://www.ioffe.ru/SVA/NSM/Semicond/AlGaAs/index.html>
- ⁹⁸ S. Adachi, *J. Appl. Phys.* **58** (3), R1 (1985).
- ⁹⁹ I. Vurgaftman, J. R. Meyer and L. R. Ram-Mohan, *J. Appl. Phys.* **89**, 11, (2001).

-
- ¹⁰⁰ I. T. Awan, H. V. A. Galeti, Y. Galvão Gobato, M. J. S. P. Brasil, D. Taylor, and M. Henini, *J. Appl. Phys.* **116**, 054506 (2014).
- ¹⁰¹ C. R. H. White, H. B. Evans, L. Eaves, P. M. Martin, M. Henini, G. Hill, and M. A. Pate, *Phys. Rev. B* **45**, 9513(R) (1992).
- ¹⁰² A. Parlange, P. C. M. Christianen, J. C. Maan, and M. Henini, *Phys. Rev. B* **63**, 115307 (2001).
- ¹⁰³ R. T. Collins, K. v. Klitzing, and K. Ploog, *Phys. Rev. B* **33**, 4378 (1986).
- ¹⁰⁴ K. Sivalertporn, L. Mouchliadis, A. L. Ivanov, R. Philp, and E. A. Muljarov, *Phys. Rev. B* **85**, 045207 (2012).
- ¹⁰⁵ D. A. B. Miller, D. S. Chemla, T. C. Damen, A. C. Gossard, W. Wiegmann, T. H. Wood, and C. A. Burrus, *Phys. Rev. Lett.* **53**, 2173 (1984).
- ¹⁰⁶ Peng Jin, C. M. Li, Z. Y. Zhang, F. Q. Liu, Y. H. Chen, X. L. Ye, B. Xu, and Z. G. Wang, *Appl. Phys. Lett.* **85**, 2791 (2004)
- ¹⁰⁷ R. J. Warburton, C. Schulhauser, D. Haft, C. Schäflein, K. Karrai, J. M. Garcia, W. Schoenfeld, and P. M. Petroff, *Phys. Rev. B* **65**, 113303 (2002).
- ¹⁰⁸ P.W. Fry et. al. *Phys. Rev. Lett.* **84**, 733 (2000)
- ¹⁰⁹ F. J. Teran, L. Eaves, L. Mansouri, H. Buhmann, D. K. Maude, M. Potemski, M. Henini, and G. Hill, *Phys. Rev. B* **71**, 161309 (2005).
- ¹¹⁰ J. Yang, R. Xu, J. Pei, Y. W. Myint, F. Wang, Z. Wang, S. Zhang, Z. Yu, and Y. Lu, *Light Sci. Appl.* **4** (2015)
- ¹¹¹ K. F. Mak, K. He, C. Lee, G. H. Lee, J. Hone, T. F. Heinz, and J. Shan, *Nat. Mater.* **12**, 207 (2013).
- ¹¹² P. K. Gogoi et. al., *Phys. Rev. Lett.* **119**, 077402 (2017).
- ¹¹³ B. Zhua, H. Zengb, J. Daic, Z. Gongga, and X. Cuia, *Proc. Natl. Acad. Sci.* **111**, 11606-11611 (2014).
- ¹¹⁴ J. Huang, T. B. Hoang and M. H. Mikkelsen, *Sci. Rep.* **6**, 22414 (2016).
- ¹¹⁵ V. Huard, R. T. Cox, K. Saminadayar, A. Arnoult, and S. Tatarenko, *Phys. Rev. Lett.* **84**, 187 (2000).
- ¹¹⁶ Y. You, X. X. Zhang, T. C. Berkelbach, M. S. Hybertsen, D. R. Reichman and T. F. Heinz, *Nat. Phys.* **11**, 477 (2015).
- ¹¹⁷ R. T. Phillips, D. J. Lovering, G. J. Denton, and G. W. Smith, *Phys. Rev. B* **45**, 4308, (1992).
- ¹¹⁸ M. Zielinski et. al., *Phys. Rev. B* **91**, 085303 (2015).
- ¹¹⁹ Z. Trabelsi, M. Yahyaoui, K. Boujdaria, M. Chamarro, and C. Testelin, *J. Appl. Phys.* **121**, 245702 (2017).
- ¹²⁰ G. D. Mahan, *Phys. Rev. Lett.* **18**, 448 (1967).
- ¹²¹ G. D. Mahan, *Phys. Rev.* **153**, 882 (1967).
- ¹²² G. Yusa, H. Shtrikman, and I. Bar-Joseph, *Phys. Rev. B* **62**, 15390 (2000).
- ¹²³ https://en.wikipedia.org/wiki/Van_Hove_singularity.
- ¹²⁴ V.V. Mkhitarian and M. E. Raikh, *Phys. Rev. Lett.* **106**, 197003 (2011).
- ¹²⁵ F. Haupt, S. Smolka, M. Hanl, W. Wüster, J. Miguel-Sanchez, A. Weichselbaum, J. von Delft, and A. Imamoglu, *Phys. Rev. B* **88**, 161304(R) (2013).
- ¹²⁶ S. W. Koch, M. Kira, G. Khitrova, and H. M. Gibbs, *Nat. Mater.* **5**, 523 (2006).
- ¹²⁷ J. J. Finley, R. J. Teissier, M. S. Skolnick, J. W. Cockburn, G. A. Roberts, R. Grey, G. Hill, M. A. Pate, and R. Paniel, *Phys. Rev. B* **58**, 10619 (1998).
- ¹²⁸ R. Beresford, L. F. Luo, W. I. Wang, and E. E. Mendez, *Appl. Phys. Lett.* **55**, 1555 (1989).
- ¹²⁹ D. S. Chemla, T. C. Damen, D. A. B. Miller, A. C. Gossard, and W. Wiegmann, *Appl. Phys. Lett.* **42**, 864 (1983).

-
- ¹³⁰ D. A. B. Miller, D. S. Chemla, T. C. Damen, A. C. Gossard, W. Wiegmann, T. H. Wood, and C. A. Burrus, *Phys. Rev. B* **32**, 1043 (1985).
- ¹³¹ Y. G. Gobato et al., *Appl. Phys. Lett.* **99**, 233507 (2011).
- ¹³² E. V. Calman, C. J. Dorow, M. M. Fogler, L. V. Butov, S. Hu, A. Mishchenko, and A. K. Geim, *Appl. Phys. Lett.* **108**, 101901 (2016).
- ¹³³ J. Szczytko, L. Kappei, J. Berney, F. Morier-Genoud, M. T. Portella-Oberli, and B. Deveaud, *Phys. Rev. Lett.* **93**, 137401 (2004).
- ¹³⁴ A. Esser, E. Runge, R. Zimmermann, and W. Langbein, *Phys. Status Solidi (a)* **178**, 489 (2000), Eq. (6).
- ¹³⁵ E. Miranda, G. Redin, and A. Faigón, *J. Appl. Phys.* **82**, 1262 (1997).
- ¹³⁶ J. C. Ranaúrez, M. J. Deen, C. H. Chen, *Microelectro. Reliability* **46**, 1939–1956, (2006).
- ¹³⁷ M. Fox, *Contemp. Phys.* **37**, 111 (1996).
- ¹³⁸ R. Rosencher, N. Vodjdani, J. Nagle, P. Bois, E. Costard, and S. Delaitre, *Appl. Phys. Lett.* **55**, 1853 (1989).
- ¹³⁹ A. K. Jonscher, C. Pickup, and S. H. Zaidi, *Semicond. Sci. Technol.* **1**, 71 (1986).
- ¹⁴⁰ B. Miller, A. Steinhoff, B. Pano, J. Klein, F. Jahnke, A. Holleitner, and U. Wurstbauer, *Nano Lett.* **17**, 5229 (2017).
- ¹⁴¹ K. S. Novoselov, A. Mishchenko, A. Carvalho, and A. H. Castro Neto, *Science* **353**, 461 (2016).
- ¹⁴² W. Xia, L. Dai, P. Yu, X. Tong, W. Song, G. Zhang, and Z. Wang, *Nanoscale* **9**, 4324 (2017).
- ¹⁴³ B. Ganchev, N. Drummond, I. Aleiner, and V. Fal'ko, *Phys. Rev. Lett.* **114**, 107401 (2015).
- ¹⁴⁴ M. A. Lampert, *Phys. Rev. Lett.* **1**, 450 (1958).
- ¹⁴⁵ F. M. Peeters, C. Riva, and K. Varga, *Phys. B: Condens. Matter.* **300**, 139 (2001).
- ¹⁴⁶ R. A. Sergeev, R. A. Suris, G. V. Astakhov, W. Ossau, and D. R. Yakovlev, *Eur. Phys. J. B* **47**, 541 (2005).
- ¹⁴⁷ P. Hawrylak, *Phys. Rev. B* **44**, 3821 (1991).
- ¹⁴⁸ G. G. Spink, P. López Ríos, N. D. Drummond, and R. J. Needs, *Phys. Rev. B* **94**, 041410 (2016).
- ¹⁴⁹ M. S. Skolnick, J. M. Rorison, K. J. Nash, D. J. Mowbray, P. R. Tapster, S. J. Bass, and A. D. Pitt, *Phys. Rev. Lett.* **58**, 2130 (1987).
- ¹⁵⁰ W. Chen, M. Fritze, A. V. Nurmikko, M. Hong, and L. L. Chang, *Phys. Rev. B* **43**, 14738 (1991).
- ¹⁵¹ H. V. A. Galeti, H. B. de Carvalho, M. J. S. P. Brasil, Y. Galvão Gobato, V. Lopez-Richard, G. E. Marques, M. Henini, and G. Hill, *Phys. Rev. B* **78**, 165309 (2008).
- ¹⁵² A. Vercik, Y. G. Gobato, and M. J. S. P. Brasil, *J. Appl. Phys.* **92**, 1888 (2002).
- ¹⁵³ H. Kalt, K. Leo, R. Cingolani, and K. Ploog, *Phys. Rev. B* **40**, 12017 (1989).
- ¹⁵⁴ E. E. Vdovin, M. Ashdown, A. Patanè, L. Eaves, R. P. Champion, Y. N. Khanin, M. Henini, and O. Makarovsky, *Phys. Rev. B* **89**, 205305 (2014).
- ¹⁵⁵ A. Bugajski and K. Reginski, *Opto-Electron. Rev.* **4**, 97 (1996).
- ¹⁵⁶ S. Glasberg, G. Finkelstein, H. Shtrikman, and I. Bar-Joseph, *Phys. Rev. B* **59**, R10425 (1999).
- ¹⁵⁷ V. Orsi Gordo, M. A. G. Balanta, Y. Galvão Gobato, F. S. Covre, H. V. A. Galeti, F. Iikawa, O. D. D. Couto, Jr., F. Qu, M. Henini, D. W. Hewak, and C. C. Huang, *Nanoscale* **10**, 4807 (2018).
- ¹⁵⁸ A. Pospischil and T. Mueller, *Appl. Sci.* **6**, 78 (2016).
- ¹⁵⁹ M. M. Fogler, L. V. Butov, and K. S. Novoselov, *Nat. Commun.* **5**, 4555 (2014).
- ¹⁶⁰ O. L. Berman and R. Y. Kezerashvili, *Phys. Rev. B* **93**, 245410 (2016).

-
- ¹⁶¹ J. Puls, G. V. Mikhailov, F. Henneberger, D. R. Yakovlev, A. Waag, and W. Faschinger, *Phys. Rev. Lett.* **89**, 287402 (2002).
- ¹⁶² S. Yu, X. Wu, Y. Wang, X. Guo, and L. Tong, *Adv. Mater.* **29**, 1606128 (2017).
- ¹⁶³ S. Datta, *Electronic Transport in Mesoscopic Systems*, 1st Ed. (Cambridge University Press, Cambridge, 1995).
- ¹⁶⁴ S. Datta, *Quantum Transport: Atom to Transistor*, (Cambridge University Press, Cambridge, 2005).
- ¹⁶⁵ T. Ihn, *Electronic Quantum Transport in Mesoscopic Semiconductor Structures*, (Springer, New York, 2004).
- ¹⁶⁶ H. Mizuta, T. Tanoue, *The Physics and Applications of Resonant Tunnelling Diodes*, (Cambridge University Press, Cambridge, 1995).
- ¹⁶⁷ L. L. Chang, L. L. Chang, E. E. Mendez, and C. Tejedor, *Resonant Tunneling in Semiconductors: Physics and Applications*, (Springer, Spain, 1990).
- ¹⁶⁸ M. Buttiker, *IBM J Res. Devp.* **32**, 63, (1988).
- ¹⁶⁹ F. Capasso, K. Mohammed, and A. Y. Cho, *Appl. Phys. Lett.* **48**, 478 (1986).
- ¹⁷⁰ S. Luryi, *Superlattices Microstruct.* **5**, 3 (1989).
- ¹⁷¹ J. Houel et. al., *Phys. Rev. Lett.* **108**, 107401 (2012).
- ¹⁷² Z. Yuan et. al., *Science* **295**, 102 (2002).
- ¹⁷³ M. Ruß, C. Meier, A. Lorke, D. Reuter and A. D. Wieck, *Phys. Rev. B* **73**, 115334 (2006).
- ¹⁷⁴ Y. N. Khanin, E. E. Vdovin, O. Makarovskii and M. Henini, *JETP Lett.* **102**, 720 (2015).
- ¹⁷⁵ Y. N. Khanin, E. E. Vdovin, *Semiconductors* **52**, 6 (2018).
- ¹⁷⁶ P. Offermans, P. M. Koenraad, and J. H. Wolter, K. Pierz, M. Roy and P. A. Maksym, *Phys. Rev. B* **72**, 165332 (2005).
- ¹⁷⁷ A. E. Belyaev, A. Patane, L. Eaves, P. C. Main, M. Henini and S. V. Danylyuk, *9th Int. Symp. "Nanostructures: Physics and Technology*, St Petersburg, Russia, (2001).
- ¹⁷⁸ P. Dawson, Z. Ma, K. Pierz, and E. O. Göbel, *Appl. Phys. Lett.* **81**, 2349 (2002).
- ¹⁷⁹ T. S. Shamirzaev, D. S. Abramkin, A. V. Nenashev, K. S. Zhuravlev, F. Trojanek, B. Dzurnak and P. Mal, *Nanotechnology* **21**, 155703 (2010).
- ¹⁸⁰ X. Q. Meng, P. Jin, Z. M. Liang, F. Q. Liu, Z. G. Wang and Z. Y. Zhang, *J. Appl. Phys.* **108**, 103515 (2010).
- ¹⁸¹ S. Luryi, *Appl. Phys. Lett.* **52**, 501 (1988).
- ¹⁸² S. Mukherjee, M. Manninen, P. S. Deo, *Physica E* **44**, 62–66 (2011).
- ¹⁸³ Y. Hu, and S. Stapleton, *Appl. Phys. Lett.* **58**, 167 (1991).
- ¹⁸⁴ B. Skinner, G. L. Yu, A. V. Kretinin, A. K. Geim, K. S. Novoselov and B. I. Shklovskii, *Phys. Rev. B* **88**, 155417 (2013).
- ¹⁸⁵ J. Dai, J. Li, H. Zeng, and X. Cui, *Appl. Phys. Lett.* **94**, 093114 (2009).
- ¹⁸⁶ S. Ilani, L. A. K. Donev, M. Kindermann and P. L. McEuen, *Nat. Phys.* **2**, 412 (2006).
- ¹⁸⁷ A. M. Nahhas, *Am. J. Nanomaterials* **6**, 1-14 (2018).
- ¹⁸⁸ C. J. Humphreys et. al., *Ultramicroscopy* **176**, 93–98 (2017).